Measurements of d_2^n and A_1^n: Probing the neutron spin structure

D. Flay,[1,2,†] M. Posik,[1] D. S. Parno,[3,4] K. Allada,[5] W. R. Armstrong,[1,6] T. Averett,[7] F. Benmokhtar,[8] W. Bertozzi,[9] A. Camsonne,[10] M. Canan,[11] G. D. Cates,[12] C. Chen,[13] J.-P. Chen,[10] S. Choi,[14] E. Chudakov,[10] F. Cusanno,[15,16,*] M. M. Dalton,[12] W. Deconinck,[9] C. W. de Jager,[10,12] X. Deng,[12] A. Deur,[10] C. Dutta,[5] L. El Fassi,[17,18] G. B. Franklin,[3] M. Friend,[3] H. Gao,[19] F. Garibaldi,[15] S. Gilad,[9] R. Gilman,[10,17] O. Glamazdin,[20] S. Golge,[11] J. Gomez,[10] L. Guo,[21] O. Hansen,[10] D. W. Higinbotham,[10] T. Holmstrom,[22] J. Huang,[9] C. Hyde,[11,23] H. F. Ibrahim,[24] X. Jiang,[17,21] G. Jin,[12] J. Katich,[7] A. Kelleher,[7] A. Kolarkar,[5] W. Korsch,[5] G. Kumbartzki,[17] J. J. LeRose,[10] R. Lindgren,[12] N. Liyanage,[12] E. Long,[25] A. Lukhanin,[1] V. Mamyan,[3] D. McNulty,[2] Z.-E. Meziani,[1,‡] R. Michaels,[10] M. Mihovilovič,[26] B. Moffit,[9,10] N. Muangma,[9] S. Nanda,[10] A. Narayan,[18] V. Nelyubin,[12] B. Norum,[27,18] Y. Oh,[28] J. C. Peng,[29] X. Qian,[19,30] Y. Qiang,[19,10] A. Rakhman,[31] R. D. Ransome,[17] S. Riordan,[27] A. Saha,[10,*] B. Sawatzky,[1,10] M. H. Shabestari,[27] A. Shahinyan,[32] S. Širca,[33] P. Solvignon,[6,10,*] R. Subedi,[27] V. Sulkosky,[9,10] W. A. Tobias,[27] W. Troth,[22] D. Wang,[27] Y. Wang,[29] B. Wojtsekhowski,[10] X. Yan,[34] H. Yao,[1,35] Y. Ye,[34] Z. Ye,[13] L. Yuan,[13] X. Zhan,[9] Y. Zhang,[36] Y.-W. Zhang,[36,17] B. Zhao,[35] and X. Zheng[27]

(Jefferson Lab Hall A Collaboration)

[1]*Temple University, Philadelphia, Pennsylvania 19122, USA*
[2]*University of Massachusetts, Amherst, Massachusetts 01003, USA*
[3]*Carnegie Mellon University, Pittsburgh, Pennsylvania 15213, USA*
[4]*Center for Experimental Nuclear Physics and Astrophysics, University of Washington, Seattle, Washington 98195, USA*
[5]*University of Kentucky, Lexington, Kentucky 40506, USA*
[6]*Argonne National Lab, Argonne, Illinois 60439, USA*
[7]*College of William and Mary, Williamsburg, Virginia 23187, USA*
[8]*Duquesne University, Pittsburgh, Pennsylvania 15282, USA*
[9]*Massachusetts Institute of Technology, Cambridge, Massachusetts 02139, USA*
[10]*Thomas Jefferson National Accelerator Facility, Newport News, Virginia 23606, USA*
[11]*Old Dominion University, Norfolk, Virginia 23529, USA*
[12]*University of Virginia, Charlottesville, Virginia 22904, USA*
[13]*Hampton University, Hampton, Virginia 23187, USA*
[14]*Seoul National University, Seoul 151-742, South Korea*
[15]*INFN, Sezione di Roma, I-00161 Rome, Italy*
[16]*Istituto Superiore di Sanità, I-00161 Rome, Italy*
[17]*Rutgers, The State University of New Jersey, Piscataway, New Jersey 08855, USA*
[18]*Mississippi State University, Mississippi 39762, USA*
[19]*Duke University, Durham, North Carolina 27708, USA*
[20]*Kharkov Institute of Physics and Technology, Kharkov 61108, Ukraine*
[21]*Los Alamos National Laboratory, Los Alamos, New Mexico 87545, USA*
[22]*Longwood University, Farmville, Virginia 23909, USA*
[23]*Université Blaise Pascal/IN2P3, F-63177 Aubière, France*
[24]*Cairo University, Giza 12613, Egypt*
[25]*Kent State University, Kent, Ohio 44242, USA*
[26]*Jožef Stefan Institute, SI-1000 Ljubljana, Slovenia*
[27]*University of Virginia, Charlottesville, Virginia 22904*
[28]*Seoul National University, Seoul 151-742, South Korea*
[29]*University of Illinois at Urbana-Champaign, Urbana, Illinois 61801, USA*
[30]*Kellogg Radiation Laboratory, California Institute of Technology, Pasadena, California 91125, USA*
[31]*Syracuse University, Syracuse, New York 13244, USA*
[32]*Yerevan Physics Institute, Yerevan 375036, Armenia*
[33]*University of Ljubljana, SI-1000 Ljubljana, Slovenia*
[34]*University of Science and Technology of China, Hefei 230026, People's Republic of China*
[35]*College of William and Mary, Williamsburg, Virginia 23187*
[36]*Lanzhou University, Lanzhou 730000, Gansu, People's Republic of China*

(Received 13 March 2016; published 6 September 2016)

[*]Deceased.
[†]flay@umass.edu
[‡]meziani@temple.edu

We report on the results of the E06-014 experiment performed at Jefferson Lab in Hall A, where a precision measurement of the twist-3 matrix element d_2 of the neutron (d_2^n) was conducted. The quantity d_2^n represents the average color Lorentz force a struck quark experiences in a deep inelastic electron scattering event off a neutron due to its interaction with the hadronizing remnants. This color force was determined from a linear combination of the third moments of the ^{3}He spin structure functions, g_1 and g_2, after nuclear corrections had been applied to these moments. The structure functions were obtained from a measurement of the unpolarized cross section and of double-spin asymmetries in the scattering of a longitudinally polarized electron beam from a transversely and a longitudinally polarized ^{3}He target. The measurement kinematics included two average Q^2 bins of 3.2 GeV^2 and 4.3 GeV^2, and Bjorken-x $0.25 \leq x \leq 0.90$ covering the deep inelastic and resonance regions. We have found that d_2^n is small and negative for $\langle Q^2 \rangle = 3.2$ GeV^2, and even smaller for $\langle Q^2 \rangle = 4.3$ GeV^2, consistent with the results of a lattice QCD calculation. The twist-4 matrix element f_2^n was extracted by combining our measured d_2^n with the world data on the first moment in x of g_1^n, Γ_1^n. We found f_2^n to be roughly an order of magnitude larger than d_2^n. Utilizing the extracted d_2^n and f_2^n data, we separated the Lorentz color force into its electric and magnetic components, $F_E^{y,n}$ and $F_B^{y,n}$, and found them to be equal and opposite in magnitude, in agreement with the predictions from an instanton model but not with those from QCD sum rules. Furthermore, using the measured double-spin asymmetries, we have extracted the virtual photon-nucleon asymmetry on the neutron A_1^n, the structure function ratio g_1^n/F_1^n, and the quark ratios $(\Delta u + \Delta\bar{u})/(u + \bar{u})$ and $(\Delta d + \Delta\bar{d})/(d + \bar{d})$. These results were found to be consistent with deep-inelastic scattering world data and with the prediction of the constituent quark model but at odds with the perturbative quantum chromodynamics predictions at large x.

DOI: 10.1103/PhysRevD.94.052003

I. INTRODUCTION

A. Overview of nucleon structure

Experiments utilizing the scattering of leptons from nucleons have been instrumental in uncovering the complex structure of subatomic matter over the past half century. In the mid-1950s, elastic scattering of electrons from hydrogen revealed that the proton is not a pointlike particle but has internal structure [1]; in the 1970s, deep-inelastic scattering (DIS) of electrons from hydrogen showed that pointlike particles, labeled "partons," are the underlying constituents of the proton [2]. These partons were later identified as quarks and gluons in the modern theory of strong interactions, quantum chromodynamics (QCD) [3].

Since the late 1970s, scattering of polarized lepton beams from polarized nucleons and polarized light nuclear targets (deuterium and ^{3}He) has given us the opportunity to probe the spin structure of the nucleon encoded in the g_1 and g_2 spin-structure functions. In particular, worldwide DIS studies focusing on g_1 as a function of both Bjorken-x and Q^2 allowed the determination of the fraction of the proton spin that is carried by the quarks [4,5] and by the gluons [6,7]. Here, x is interpreted as the fractional momentum of the parent nucleon carried by the struck quark in the infinite momentum frame, and $Q^2 \equiv -q^2$ is the four-momentum transferred to the target squared.

Early theoretical work [8] has shown that the $g_1(x, Q^2)$ and $g_2(x, Q^2)$ spin-structure functions contain information on quark-gluon correlations. These dynamical effects are accessible through the Q^2-variations of these functions beyond those of the calculable perturbative QCD (pQCD) radiative corrections [9]. In fact, they appear in an expansion of both the measured g_1 spin-structure function and its moments in x in powers of $1/Q^2$, but only at higher order. In contrast, in the measured g_2 spin-structure function, quark-gluon interactions are accessible at leading order in a similar expansion and thus suffer no $1/Q^2$ suppression. This makes measurements of g_2 particularly sensitive and important for studying multiparton correlations in the nucleon.

Studies of the moments in x of spin-structure functions have resulted in fundamental tests of QCD like that of the Bjorken sum rule [10]; here, not only do they offer an opportunity to test our understanding of pQCD beyond the simple partonic picture, but they also allow for measured observables to be tested against *ab initio* calculations of lattice QCD. While there is a wealth of data available for g_1, fewer data exist for g_2—especially in the valence region. This region provides the dominant contribution to higher moments. These moments are of interest because the contribution arising from the lower-x region of integration, where the structure functions are unknown, is small. Thus these higher moments offer robust experimental results relevant for a comparison with lattice QCD, for example. Finally, it is worth noting that high-precision data of the g_1 nucleon structure function in the valence region of deep inelastic scattering—namely $x \geq 0.6$—are still sparse, and every new data set with good precision offers a real possibility to test nucleon models in a domain sensitive to those models' parameters.

B. The g_2 structure function and quark-gluon correlations

While the polarized structure function g_2 has no clear interpretation in the quark-parton model [11], it is known to contain quark-gluon correlations and can be decomposed as

$$g_2(x,Q^2) = g_2^{\mathrm{WW}}(x,Q^2) + \bar{g}_2(x,Q^2), \tag{1}$$

where $\bar{g}_2$ is the component of g_2 that contains the quark-gluon correlations [8], given by [12]

$$\bar{g}_2(x,Q^2) = \int_x^1 \frac{\partial}{\partial y}\left[\frac{m_q}{M} h_T(x,Q^2) + \xi(y,Q^2)\right]\frac{dy}{y}. \tag{2}$$

Here, h_T denotes the transversity distribution in the nucleon [13], ξ the quark-gluon correlation function, m_q the quark mass of flavor q, and M the nucleon mass. The quantity g_2^{WW} in Eq. (1) is the Wandzura-Wilczek term, which is fully determined from the knowledge of the g_1 structure function [14],

$$g_2^{\mathrm{WW}}(x,Q^2) = -g_1(x,Q^2) + \int_x^1 \frac{g_1(y,Q^2)}{y}dy. \tag{3}$$

Under the operator product expansion (OPE) [15], one can access the effects of quark-gluon correlations via the third moment of a linear combination of g_1 and g_2,

$$\begin{aligned} d_2(Q^2) &= 3\int_0^1 x^2 \bar{g}_2(x,Q^2)dx \\ &= \int_0^1 x^2[2g_1(x,Q^2) + 3g_2(x,Q^2)]dx. \end{aligned} \tag{4}$$

Because of the x^2-weighting, d_2 is particularly sensitive to the large-x behavior of $\bar{g}_2$. The quantity d_2 is related to a specific twist-3 ($\tau = 3$) matrix element consisting of local operators of quark and gluon fields [13,16,17],

$$2MP^+P^+S^x d_2 = g\langle P,S|\bar{\psi}(0)\gamma^+ G^{+y}(0)\psi(0)|P,S\rangle, \tag{5}$$

where P denotes the nucleon momentum, S its spin, ψ the quark field, and g the QCD coupling constant. The $+$ superscript indicates the equation is expressed in light-cone coordinates. In analogy to the electromagnetic Lorentz force F^y that acts on a charged particle, the gluon field $G^{+y} = (B^x - E^y)/\sqrt{2} = F^y$, where B^x and E^y are the transverse components of the color magnetic and color electric field, respectively; the z direction is defined by the three-momentum transfer of the virtual photon [17].

There are two interpretations of d_2 in the literature. The first connects d_2 with color electromagnetic fields induced in a transversely polarized nucleon probed by a virtual photon. These induced color fields [appearing in Eq. (5)] are represented as color polarizabilities χ [13],

$$\chi_E \vec{S} = \frac{1}{2M^2}\langle P,S|\psi^\dagger g\vec{a}\times\vec{E}\psi|P,S\rangle, \tag{6}$$

$$\chi_B \vec{S} = \frac{1}{2M^2}\langle P,S|\psi^\dagger g\vec{B}\psi|P,S\rangle, \tag{7}$$

where $\vec{a}$ denotes the velocity of the struck quark. Then, d_2 can be expressed as

$$d_2 = \frac{1}{4}(\chi_E + 2\chi_B). \tag{8}$$

A second, more recent interpretation shows that the matrix element connected to d_2 represents an average color Lorentz force F^y acting on the struck quark due to the remnant diquark system at the instant it is struck by the virtual photon [cf. Eq. (5)],

$$F^y(0) \equiv \langle P,S|\bar{\psi}(0)\gamma^+ G^{+y}(0)\psi(0)|P,S\rangle \tag{9}$$

$$= -M^2 d_2, \tag{10}$$

where the last equality is true only in the rest frame of the nucleon [17].

Combining measurements of d_2 with the twist-4 matrix element f_2 allows the extraction of the color electric and magnetic forces F_E^y and F_B^y [17],

$$d_2 = -\frac{1}{M^2}(F_E^y + F_B^y), \tag{11}$$

$$f_2 = -\frac{2}{M^2}(2F_E^y - F_B^y). \tag{12}$$

The quantity f_2 is sensitive to quark-gluon correlations, since it is expressed as a matrix element similar to d_2, containing a mixed quark-gluon field operator [8,18–20]. The f_2 matrix element cannot be measured directly, but can be extracted from g_1 data by utilizing a twist expansion of Γ_1, the first moment of g_1,

$$\begin{aligned} \Gamma_1 &\equiv \int_0^1 g_1 dx \\ &= \mu_2 + \frac{M^2}{9Q^2}(a_2 + 4d_2 + 4f_2) + \frac{\mu_6}{Q^4} \\ &\quad + \mathcal{O}\left(\frac{1}{Q^6}\right) + \cdots. \end{aligned} \tag{13}$$

For simplicity the Q^2 dependence of the structure functions, matrix elements, and μ_n terms has been omitted in Eq. (13). The quantity $a_2 = \int x^2 g_1 dx$ is the third moment of g_1, a twist-2 matrix element that has connections to target mass corrections. The term μ_6 is a higher-twist ($\tau > 4$) term. The quantity μ_2 is the twist-2 contribution, given as

$$\mu_2(Q^2) = C_{ns}(Q^2)\left(-\frac{1}{12}g_A + \frac{1}{36}a_8\right) + C_s(Q^2)\frac{1}{9}\Delta\Sigma, \tag{14}$$

where C_{ns} and C_s denote the nonsinglet and singlet Wilson coefficients [21], g_A the flavor-triplet axial charge, a_8 the octet axial charge, and $\Delta\Sigma \equiv \Delta\Sigma(Q^2 = \infty)$, the renormalization group invariant definition of the singlet axial current. This definition of $\Delta\Sigma$ is used to factorize all of the Q^2 dependence into the Wilson coefficients, as was done in Refs. [20,22]. The f_2 matrix element can be extracted from Eq. (13) by first subtracting μ_2 from Γ_1 and then fitting the result as a function of $1/Q^2$.

In practice, in order to access the spin-structure functions g_1 and g_2, we measure experimental asymmetries,

$$\begin{aligned} A_\parallel &\equiv \frac{\sigma^{\downarrow\Uparrow} - \sigma^{\uparrow\Uparrow}}{\sigma^{\downarrow\Uparrow} + \sigma^{\uparrow\Uparrow}} \\ &= \frac{4\alpha^2}{MQ^2}\frac{(1-y)(2-y)}{2y^2\sigma_0} \\ &\quad \times \frac{(1-y)\sin\theta}{1+(1-y)[\cos\theta + \tan(\theta/2)\sin\theta]} \\ &\quad \times \left\{ y\frac{1+(1-y)\cos\theta}{(1-y)\sin\theta}g_1 - 2\tan(\theta/2)g_2 \right\} \end{aligned} \tag{15}$$

and

$$\begin{aligned} A_\perp &\equiv \frac{\sigma^{\downarrow\Rightarrow} - \sigma^{\uparrow\Rightarrow}}{\sigma^{\downarrow\Rightarrow} + \sigma^{\uparrow\Rightarrow}} \\ &= \frac{4\alpha^2}{MQ^2}\frac{(1-y)(2-y)}{2y^2\sigma_0} \\ &\quad \times \frac{(1-y)\sin\theta}{1+(1-y)[\cos\theta + \tan(\theta/2)\sin\theta]} \\ &\quad \times \{ yg_1 + 2g_2 \}. \end{aligned} \tag{16}$$

The quantity σ^{sS} denotes the polarized cross section for electron spin s and target spin S. The $\uparrow$ ($\downarrow$) indicates the electron spin parallel (antiparallel) to its momentum, and $\Uparrow$ ($\Downarrow$) indicates the target spin parallel (antiparallel) to the electron beam momentum. The $\Leftarrow$ ($\Rightarrow$) indicates the target spin perpendicular to the beam momentum, pointing away from (toward) the side of the beam line on which the scattered electron is detected. The quantity $y = (E - E')/E$ is the fractional energy transferred to the target, with E being the electron beam energy and E' the scattered electron energy, with E and E' measured in the laboratory frame. The quantity α denotes the electromagnetic coupling constant and θ the electron scattering angle. The quantity σ_0 is the unpolarized electron scattering cross section. The dependence of g_1, g_2, and σ_0 on x and Q^2 has been suppressed for simplicity.

The two spin structure functions g_1 and g_2 can be expressed in terms of the experimental observables $A_\parallel$, $A_\perp$, and σ_0 by combining and inverting Eqs. (16) and (17). Then the expression for d_2 in Eq. (4) can be rewritten in terms of those experimental observables,

$$\begin{aligned} d_2 = \int_0^1 dx \frac{MQ^2}{4\alpha^2}\frac{x^2y^2}{(1-y)(2-y)}\sigma_0 \\ \times \left[\left(3\frac{1+(1-y)\cos\theta}{(1-y)\sin\theta} + \frac{4}{y}\tan(\theta/2) \right) A_\perp \right. \\ \left. + \left(\frac{4}{y} - 3 \right) A_\parallel \right]. \end{aligned} \tag{17}$$

The prior world data for d_2^n as a function of Q^2 [23] are presented in Fig. 1. The top panel shows measured data and model calculations without the elastic contribution, while the bottom panel shows the same data and models with the elastic contribution included. Resonance measurements from JLab E94-010 [24] and RSS [25], along with resonance plus DIS data from E01-012 [26], are shown

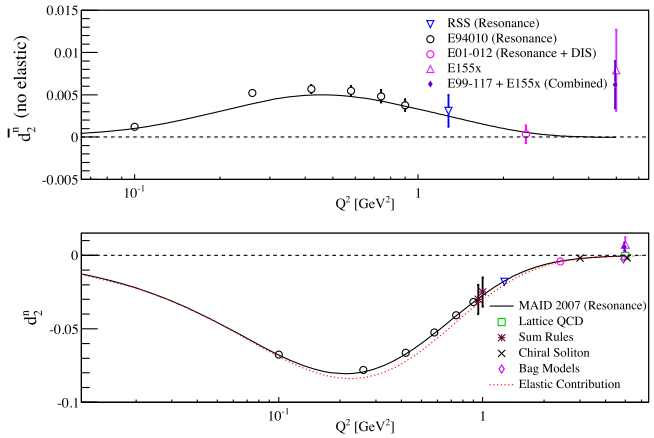

FIG. 1. The world d_2^n data as a function of Q^2. Upper panel: Data and models without the elastic contribution. Bottom panel: Data and models with the elastic contribution included. The experimental resonance data from JLab E94-010 [24] and RSS [25], along with resonance plus DIS data from E01-012 [26], are shown at $Q^2 \lesssim 3$ GeV^2, while at larger Q^2 DIS data from SLAC E155x [27] and combined data from JLab E99-117 and SLAC E155x [28] are shown. The solid curve is from a MAID [29] calculation, which is dominated by the resonance contribution. Model calculations for $Q^2 \approx 1$ GeV^2 from a QCD sum rule approach from Ref. [30] (offset lower in Q^2) and Ref. [31] are shown. A chiral soliton model [32] and a bag model [33] are also given. Additionally, a lattice QCD [34] calculation is shown. The model calculations that include the elastic contribution are shown in the lower panel only. We added the elastic contribution to the MAID model in the lower panel. The elastic contribution to d_2^n is given in the lower panel by the dashed curve, evaluated using the Cornwall-Norton (CN) moments (see Appendix B) where the Riordan [35] and Kelly [36] parametrizations are used for G_E^n and G_M^n, respectively.

at $Q^2 \lesssim 3$ GeV^2. At large Q^2 toward 5 GeV^2 are DIS measurements from SLAC E155x [27] and the combined data from JLab E99-117 and SLAC E155x [28]. In the latter data set, d_2^n was evaluated by combining the g_2^n data from JLab E99-117 with the g_2 data of SLAC E155x, and $\bar{g}_2$ was assumed to be Q^2-independent and to follow $\bar{g}_2 \propto (1-x)^m$ with $m = 2$ or 3 for $x \gtrsim 0.78$ [27], for which there were no data from either experiment [28].

The solid curve in Fig. 1 is from a MAID [29] calculation, which uses phenomenological fits to electro- and photoproduction data for the nucleon, extending from the single-pion production threshold to the resonance/DIS boundary at $W = 2$ GeV. The major resonances are modeled using Breit-Wigner functions to construct the production channels. The bottom panel displays the results of additional model calculations from a QCD sum rule approach [30,31], which in general uses dispersion relations, combined with the OPE, to interpolate between the perturbative and nonperturbative regimes of QCD. The two calculations presented at $Q^2 \approx 1$ GeV^2 use a three-quark field with [30] (offset lower in Q^2 in Fig. 1) and without [31] a gluon field. A chiral soliton model [32] is shown, where the nucleon is described as a nonlinear dynamical system consisting of "mesonic lumps" [32] governed by a $U(1) \times SU(2)_L \times SU(2)_R$ chiral symmetry. Another model displayed is a bag model, in which the quarks are confined to a nucleon "bag." Here, the confinement mechanism of QCD is simulated using quark-gluon and gluon-gluon interactions [33]. The model also includes generalized spin-dependent effects via an explicit symmetry-breaking parameter [37]. A lattice QCD calculation [34] is also presented, which solves the dynamical QCD equations nonperturbatively on a discretized lattice. The model calculations that include the elastic contribution are shown in the lower panel only. We added the elastic contribution to the MAID model in the lower panel. Our measurement focused on the moderately large-Q^2 region of $3 < Q^2 < 5$ GeV^2, where the elastic contribution is seen to be small (lower panel of Fig. 1) and where a theoretical interpretation in terms of twist-3 contributions is cleaner.

While bag [33,38,39] and soliton [32] model calculations of d_2 for the neutron yield numerical values consistent with those of lattice QCD [34], prior experimental data differ by roughly 2 standard deviations in the large Q^2-range. This is illustrated by the data for $Q^2 \approx 5$ GeV^2 in Fig. 1. This situation called for a dedicated experiment for the neutron, JLab E06-014. For the proton d_2, the measurements and models are in better agreement [27,30–34,40]. These data sets will be further extended by a recent measurement [41] whose precision results are expected in the near future. Under the assumption of isospin symmetry, combining the neutron and proton data would then allow a flavor decomposition to determine the average color force felt by the up and down quarks in the proton. Measurements of d_2 access similar forces as those that cause quark confinement. Consequently, such measurements are important for understanding the dynamics of the constituents of the nucleon.

Our measurements of the unpolarized cross section σ_0 and the double-spin asymmetries $A_\parallel$ and $A_\perp$ allow the extraction of d_2, and in turn, f_2. Combining our results for these higher-twist matrix elements, we obtain the color electric and magnetic forces F_E^y and F_B^y. Utilizing our data on g_1, we also evaluate the twist-2 matrix element a_2 and test it against lattice QCD calculations.

C. A_1 and flavor decomposition

The measurement of the double-spin asymmetries $A_\parallel$ and $A_\perp$ required for the extraction of d_2 also gives access to the virtual photon-nucleon asymmetry A_1 and the polarized to unpolarized structure-function ratio g_1/F_1,

$$A_1 = \frac{1}{D(1+\eta\xi)} A_\parallel - \frac{\eta}{d(1+\eta\xi)} A_\perp, \tag{18}$$

$$\frac{g_1}{F_1} = \frac{1}{d'}\left(A_\parallel + \tan\frac{\theta}{2} A_\perp\right), \tag{19}$$

where $F_1(x, Q^2)$ denotes the unpolarized structure function and D the virtual photon depolarization factor. This quantity, along with η, d, ξ, and d' are defined as

$$D = \frac{E - \epsilon E'}{E(1+\epsilon R)}, \tag{20}$$

$$\eta = \frac{\epsilon\sqrt{Q^2}}{E - \epsilon E'}, \tag{21}$$

$$d = D\sqrt{\frac{2\epsilon}{1+\epsilon}}, \tag{22}$$

$$\xi = \eta\frac{1+\epsilon}{2\epsilon}, \tag{23}$$

$$d' = \frac{(1-\epsilon)(2-y)}{y(1+\epsilon R)}, \tag{24}$$

where $R \equiv \sigma_L/\sigma_T$, the ratio of longitudinally to transversely polarized photoabsorption cross sections [42], and ϵ denotes the ratio of the longitudinal to transverse polarization of the virtual photon,

$$\epsilon = \left[1 + 2(1+\gamma^2)\tan^2\frac{\theta}{2}\right]^{-1}, \tag{25}$$

with $\gamma^2 = (2Mx)^2/Q^2$.

The A_1 asymmetry is particularly sensitive to the way that the quark spins combine to give the nucleon spin. Therefore, A_1 is a good discriminator for various model calculations that aim to describe the spin structure of the

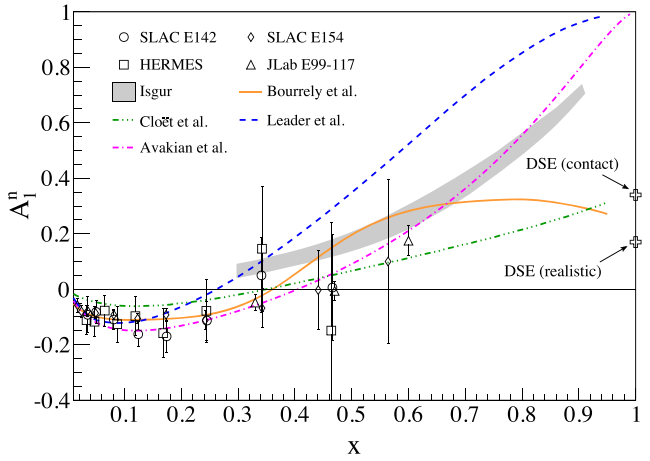

FIG. 2. World data for A_1^n from SLAC E142 [43] and E154 [44], HERMES [45], and JLab E99-117 [28,46], compared to various models, including a pQCD-inspired global analysis (dashed curve) [49], a statistical quark model from Bourrely *et al.* (solid curve) [51], a pQCD parametrization including OAM from Avakian *et al.* (dash-dotted curve) [50] and a CQM model from Isgur (gray band) [48]. Also plotted is an NJL-type model from Cloët *et al.* (dash triple-dotted curve) [52]. Predictions from Dyson-Schwinger equation treatments by Roberts *et al.* [53] are shown at $x = 1$.

nucleon. Figure 2 shows the previous world data using ^{3}He targets from SLAC E142 [43] and E154 [44], HERMES [45], and JLab E99-117 [28,46] compared to various models. The SLAC E143 [47] data, which used NH_3 and ND_3 targets, have been omitted from the plot due to their large uncertainties. It is seen that the relativistic constituent quark model (CQM) [48] describes the trend of the data reasonably well. The pQCD parametrization with hadron helicity conservation [49] (dashed curve)—assuming quark orbital angular momentum to be zero—does not describe the data adequately. However, the pQCD parametrization allowing for quark orbital angular momentum to be nonzero [50] (dash-dotted curve) is in good agreement with the data, suggesting the importance of quark orbital angular momentum in the spin structure of the nucleon. The statistical quark model (solid curve) [51], which interprets the constituent partons as fermions (quarks) and bosons (gluons), adequately describes the trend of the world data after fitting its parameters to a subset of the available data. A modified Nambu-Jona-Lasinio (NJL) model from Cloët *et al.* (dash triple-dotted curve) [52] is shown to fit the data accurately in the large-x region. This NJL-type model imposes constraints for confinement such that unphysical thresholds for nucleon decay into quarks are excluded. Nucleon states are obtained by solving the Faddeev equation using a quark-diquark approximation, including scalar and axial-vector diquark states. Relatively recent predictions come from Dyson-Schwinger equation (DSE) treatments by Roberts *et al.* [53], which reveal nonpointlike diquark correlations in the nucleon due to dynamical chiral symmetry breaking. In these calculations Roberts *et al.* employ two different types of dressed-quark propagators for the Faddeev equation: one where the mass term is momentum independent, and the other where the mass term carries a momentum dependence. This yields two different sets of results, referred to as *contact* and *realistic*, respectively. The predictions for the two approaches are shown at $x = 1$ (Fig. 2). We note the contrast between the DSE predictions and those from pQCD and CQMs, where the latter two predict $A_1^n \to 1$ as $x \to 1$. The measurement presented here provides more contiguous coverage over the region of $0.27 < x < 0.60$ compared to the JLab E99-117 measurement [28,46].

Even more than A_1, the polarized-to-unpolarized quark parton distribution function (PDF) ratios for the up quark (u), given by $(\Delta u + \Delta\bar{u})/(u + \bar{u})$, and the down quark ($d$), given by $(\Delta d + \Delta\bar{d})/(d + \bar{d})$, allow a high level of discrimination between theoretical models that describe the quark-spin contribution to nucleon spin. Such ratios may be extracted from measurements of g_1/F_1 at leading order in Q^2 according to

$$\frac{\Delta u + \Delta\bar{u}}{u + \bar{u}} = \frac{4}{15}\frac{g_1^p}{F_1^p}(4 + R^{du}) - \frac{1}{15}\frac{g_1^n}{F_1^n}(1 + 4R^{du}), \tag{26}$$

$$\frac{\Delta d + \Delta\bar{d}}{d + \bar{d}} = \frac{4}{15}\frac{g_1^n}{F_1^n}\left(4 + \frac{1}{R^{du}}\right) - \frac{1}{15}\frac{g_1^p}{F_1^p}\left(1 + 4\frac{1}{R^{du}}\right), \tag{27}$$

where $R^{du} \equiv (d + \bar{d})/(u + \bar{u})$. Earlier experimental data for $(\Delta u + \Delta\bar{u})/(u + \bar{u})$ and $(\Delta d + \Delta\bar{d})/(d + \bar{d})$ are shown in Fig. 3, where the data in the upper (lower) part of the figure represent the up (down) quark ratio. The data shown are from HERMES [54] and COMPASS [55], both semi-inclusive DIS measurements, and JLab experiments E99-117 [28] and CLAS EG1b [56], both of which are inclusive DIS measurements. The semi-inclusive DIS data from HERMES and COMPASS are constructed from their published polarized PDF data, where we used the same unpolarized PDF parametrizations as were applied in the original analyses: CTEQ5L [57] for the HERMES data, and MRST2006 [58] for the COMPASS data. The uncertainties are thus slightly larger than could be achieved from the raw data. The dashed curve represents a next-to-leading order (NLO) QCD global analysis that includes target mass corrections and higher-twist effects [59], and the dash-dotted curve represents a pQCD calculation that includes orbital angular momentum effects [50]. The solid curve shows the statistical quark model [51], and the dash–triple-dotted curve is a modified NJL model [52]. At $x = 1$, DSE calculations [53] are indicated by open stars (crosses) for

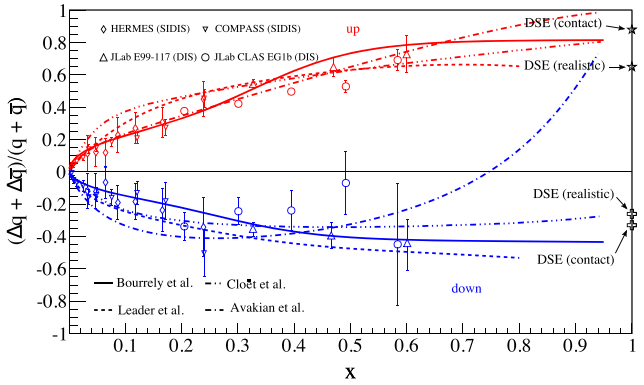

FIG. 3. The world data for the up- and down-quark polarized-to-unpolarized PDF ratios. The data shown are from HERMES [54] and COMPASS [55], both of which are semi-inclusive DIS measurements, and JLab E99-117 [28] and CLAS EG1b [56], both of which are DIS measurements. Theoretical curves are from an NLO QCD analysis from Leader *et al.* [59] (dashed curves) and pQCD-inspired fit from Avakian *et al.* [50] (dash-dotted curves). The solid curve shows a statistical quark model from Bourrely *et al.* [51], and the dash–triple-dotted curve shows a modified NJL model calculation from Cloët *et al.* [52]. The open stars (crosses) at $x = 1$ indicate the DSE calculations from Roberts *et al.* [53] for up (down) quarks.

the up (down) quark ratios. Clearly, both pQCD models predict that $\Delta q/q \to 1$ at large x, which implies that the positive helicity state of the quark (quark spin aligned with the nucleon spin) must dominate as $x \to 1$. The data for $(\Delta u + \Delta\bar{u})/(u + \bar{u})$ are consistent with this prediction; however, we note that the current $(\Delta d + \Delta\bar{d})/(d + \bar{d})$ data show no sign of turning positive as we approach the large x region. The calculation of Avakian *et al.* fits the down quark data better, but still has a zero crossing at $x \sim 0.75$. The data in Fig. 3 imply that in general, the up quark spins tend to be parallel to the nucleon spin, whereas the down quark spins are antiparallel to the nucleon spin. The trend of the down quark data, supported by the model of Avakian *et al.*, suggests that quark orbital angular momentum might play an important role in the spin of the nucleon. The experiment presented here aims to provide more complete kinematic coverage for the down quark, especially in the large-x region approaching $x \sim 0.6$, where the predictions of the pQCD models start to contrast with those of the CQMs and the DSE calculations.

D. Outline of the paper

The body of this paper is structured as follows: in Sec. II we discuss the experimental setup and the performance of the polarized electron beam and of the particle detectors for JLab E06-014; in Sec. III, we discuss the polarized ^{3}He target; in Sec. IV, the data analysis to obtain the cross sections and asymmetries is presented. The nuclear corrections required to extract the neutron results for d_2, a_2, A_1, and g_1/F_1 are also discussed. In Sec. V the results of the experiment are presented. In particular, ^{3}He results for the unpolarized cross section, double-spin asymmetries, g_1, g_2, A_1, and g_1/F_1 are given in Sec. V A. In Sec. V B the results for the neutron d_2 and a_2 are presented. Following this, the analysis necessary to obtain the twist-4 matrix element f_2, leading to the extraction of the color forces F_E^y and F_B^y on the neutron, is discussed in Sec. V B 3. The quantities A_1 and g_1/F_1 on the neutron are presented in Secs. V B 4 and V B 5, respectively. The flavor separation analysis to obtain $(\Delta u+\Delta\bar{u})/(u+\bar{u})$ and $(\Delta d+\Delta\bar{d})/(d+\bar{d})$ is discussed, and the results are presented in Sec. V C. Concluding remarks are given in Sec. VI. Appendix A gives an overview of the DIS kinematics, structure functions, and cross sections, while Appendix B discusses the details of the operator product expansion. Fits to unpolarized nitrogen cross sections and positron cross sections measured in this experiment, used in correcting the measured $e-^3$He cross section, are presented in Appendix C. Also presented in that appendix are fits to world proton data on g_1/F_1 and A_1, needed for the nuclear corrections. Details for the world Γ_1^n data and fitting the higher-twist component of Γ_1^n are given in Appendix D. The systematic uncertainties for all results presented in this paper are tabulated in Appendix E.

II. THE EXPERIMENT

The E06-014 experiment ran in Hall A of Thomas Jefferson National Accelerator Facility (Jefferson Lab or JLab) for six weeks in five run periods from February to March 2009, consisting of a commissioning run using 1.2 GeV electrons, a 5.89 GeV run using polarized electrons, a 4.74 GeV run using unpolarized electrons, and finally runs using polarized electrons at energies of 5.89 GeV and 4.74 GeV. The data at 4.74 GeV and 5.89 GeV were the production data sets, which covered the resonance and deep inelastic valence quark regions, in a kinematic region of $0.25 \le x \le 0.9$ and $2\ \text{GeV}^2 \le Q^2 \le 6\ \text{GeV}^2$, shown in Fig. 4.

Polarized electrons were scattered from a polarized ^{3}He target, which acts as an effective polarized neutron target [60]. The scattered electrons were detected independently in the left high-resolution spectrometer (LHRS) and in the BigBite spectrometer, which were oriented at a scattering angle of $\theta = 45°$ to the left and right of the beam line, respectively. The unpolarized cross section σ_0 was extracted from the LHRS data, and the double-spin asymmetries $A_\parallel$ and $A_\perp$ were obtained from the BigBite data. The matrix element d_2 was computed using Eq. (17), and the virtual photon asymmetry A_1 and structure function ratio g_1/F_1 were extracted according to Eqs. (18) and (19), respectively.

The measurement with the BigBite spectrometer consisted of 20 evenly spaced, continuous bins in x with a bin width of 0.05 for each beam energy; of these, seven were discarded because of insufficient statistics. The statistics in

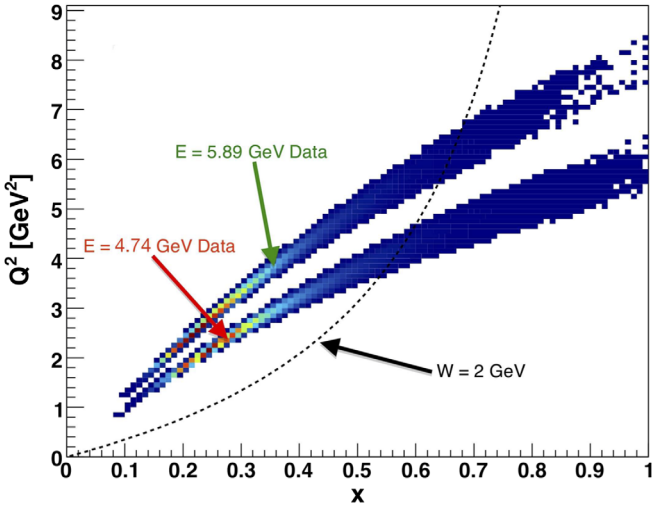

FIG. 4. The E06-014 kinematic coverage in Q^2 and x. The lower band represents the $E = 4.74$ GeV data set and the upper band the $E = 5.89$ GeV one. The black dashed line shows $W = 2$ GeV. The regions to the left and right of this line correspond to DIS and resonance kinematics, respectively.

all bins for a given beam energy were recorded simultaneously. The LHRS data were acquired in 9 unevenly spaced bins in the scattered electron momentum p for the $E = 4.74$ GeV run and 11 unevenly spaced bins for the $E = 5.89$ GeV run, covering a range of $0.6 \leq p \leq 1.7$ GeV as listed in Tables I and II. The statistics in the LHRS were recorded sequentially. For the d_2 extraction, the measured cross sections were interpolated and extrapolated to match the binning of the BigBite data.

The experimental run plan optimized its statistics on the d_2 integral [Eq. (17)] in order to minimize the error on d_2, *not* on the structure functions g_1 and g_2. After the extraction of $d_2^{^3\mathrm{He}}$, nuclear corrections were applied (Sec. IV D) to obtain d_2^n.

A. The polarized electron beam

The high-energy longitudinally polarized electron beam is provided by the Continuous Electron Beam Accelerator Facility (CEBAF) at JLab [61]. Polarized electrons are produced by shining circularly polarized laser light on a strained superlattice gallium arsenide (GaAs) photocathode. This produces electrons with a polarization of up to ~85% at currents up to ~200 μA. High-energy electrons are achieved by two superconducting radio-frequency (RF) linear accelerators connected by two magnetic recirculating arcs. The beam may be circulated around the racetrack accelerator up to a maximum of 5 times to achieve an energy of ~6 GeV [61].

TABLE I. Kinematic bins for the LHRS for the 4.74 GeV run. The LHRS momentum setting is labeled as p_0.

p_0 [GeV]	x	Q^2 [GeV^2]
0.60	0.215	1.66
0.80	0.301	2.22
1.12	0.458	3.10
1.19	0.496	3.30
1.26	0.536	3.49
1.34	0.584	3.71
1.42	0.634	3.93
1.51	0.693	4.18
1.60	0.755	4.43

TABLE II. Kinematic bins for the LHRS for the 5.89 GeV run. The LHRS momentum setting is labeled as p_0.

p_0 [GeV]	x	Q^2 [GeV^2]
0.60	0.209	2.07
0.70	0.248	2.42
0.90	0.332	3.11
1.13	0.437	3.90
1.20	0.471	4.14
1.27	0.506	4.38
1.34	0.542	4.62
1.42	0.584	4.90
1.51	0.634	5.21
1.60	0.686	5.52
1.70	0.746	5.87

B. Beam helicity

To control certain systematic errors associated with the electron beam polarization during the experiment, the helicity of the electrons was flipped every 33 ms. This time frame was referred to as a helicity window, and successive windows were separated by master pulse signals. Each window had a definite helicity state in which the electron spin was either parallel (+) or antiparallel (−) to the beam direction. Helicity windows were organized into quartets, taking the form $+--+$ or $-++-$. The helicity state of the first window of the quartet was decided by a pseudorandom number generator, and in turn defined the helicity state for the remaining windows. A signal indicating the helicity of each window was sent to the data acquisition (DAQ) systems.

At the electron source an insertable half-wave plate (IHWP) can be placed in the path of the laser illuminating the strained GaAs source to reverse the helicity of the extracted polarized electrons relative to the helicity signal. This was done for about half of the statistics to minimize possible systematic effects due to the helicity bit. The asymmetry in the amount of charge delivered with the two helicity states was found to be negligible [62]; this was accomplished using a feedback loop and a specialized data acquisition system developed by a previous JLab experiment [63].

To determine the actual sign of the electrons' helicity state for each window type, a measurement of the quasielastic ^{3}He

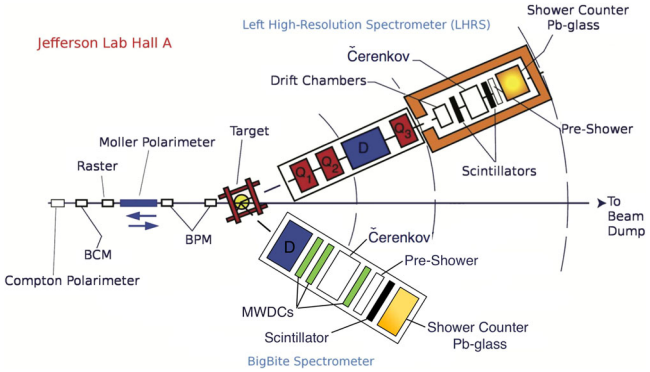

FIG. 5. Overhead view of the experimental setup for E06-014. The longitudinally polarized electron beam enters from the left and scatters from the longitudinally or transversely polarized ^{3}He target, which is discussed in Sec. III. The Møller and Compton polarimeters provide beam polarization measurements, presented in Sec. II D 2. The LHRS and BigBite spectrometers are positioned at 45° with respect to the beam line and detect scattered electrons.

asymmetry was made and compared to a theoretical calculation [64]. For more details, see Sec. IV C.

C. Hall A overview

The layout of the Hall A hardware for this experiment is shown in Fig. 5. Along the beam line are beam diagnostic tools, like the beam current monitors (BCMs), beam position monitors (BPMs), and the Møller and Compton polarimeters. A polarized ^{3}He target was utilized as an effective polarized neutron target. Scattered electrons were measured independently in the LHRS and the BigBite spectrometers, each equipped with a gas Čerenkov detector and electromagnetic calorimeters for particle identification (PID) purposes. In the LHRS quadrupole and dipole magnets are used to focus charged particles into the detector stack, while a single dipole magnet bends charged particles into the BigBite detector stack. In each spectrometer wire drift chambers are used to reconstruct particle tracks. Each of these elements will be described in the following sections.

D. The Hall A beam line

The beam line in Hall A contains a number of important diagnostic components: BCMs, BPMs, and the polarimetry apparatus. We first discuss the BCMs and BPMs in Sec. II D 1, followed by the beam polarization measurements in Sec. II D 2. The measurement of the beam energy is presented in Sec. II D 3.

1. Beam charge and position monitoring

The experiment ran at beam currents of $\sim 15\ \mu$A. Fluctuations about the required value and beam trips, due to difficulties in the accelerator or in the other two experimental halls, make it important to monitor the beam current. To this purpose two BCMs, which are resonant RF cavities, are utilized. These cavities, stainless-steel cylinders with a Q factor of ~ 3000, were tuned to the fundamental beam frequency of 1.497 GHz. The two BCMs were located 25 m upstream of the target, where one cavity was denoted as upstream and the other as downstream, based on their relative positions along the beam line. Each produced a voltage signal that was proportional to the measured current. Three copies of the signal were recorded, each amplified by a different gain factor (1, 3, or 10), resulting in six signals altogether (three for each cavity) [65]. Each copy of the signal was amplified by its assigned gain and then sent to a voltage-to-frequency converter. These signals were calibrated using a Faraday cup [64]. Each signal was read out by scalers in the LHRS and BigBite spectrometers.

For accurate vertex reconstruction and proper momentum calculation for each detected electron, the position of the electron beam in the plane transverse to the nominal beam direction at the target was needed. The measurement of the beam position was accomplished through the use of two BPMs. They each consisted of four antenna arrays placed ~ 7.5 m and ~ 1.3 m upstream of the target. Pairs of wires were positioned at $\pm 45°$ relative to the horizontal and vertical directions in the hall. The signal induced in the wires by the beam was inversely proportional to the distance from the beam to the wires and was recorded by analog-to-digital converters (ADCs). The differences between the signals in pairs of wires in a given plane yielded a positional resolution of 100 μm [66]. Combining the measurements of the two BPMs yielded the trajectory of the beam; extrapolating these data gave the position at the target. The BPMs were calibrated using wire scanners called harps. A single harp was located immediately downstream of each BPM. Harp measurements allow the relative position measurements from the BPMs to be tied to the Hall A coordinate system. They interfered with the beam, so dedicated runs called "bull's eye" scans were needed. A bull's eye scan consisted of five measurements with (x, y) data points in the plane perpendicular to the beam momentum with the beam positioned at different locations. Four of these points described the corners of a 4 mm by 4 mm square, and the fifth data point measured the square's center [64].

In order to avoid damage to the glass target cell due to beam heating, the beam was rastered (scanned) at high speeds (17–24 kHz) across a large rectangular cross section $(\approx 4 \times 6\ \text{mm}^2)$ at the target. This rectangular distribution was achieved by two dipole magnets (one for vertical, one for horizontal) located 23 m upstream of the target [65].

2. Beam polarization measurement

The polarization of the electron beam was measured using two different polarimeters, a Møller and a Compton polarimeter. Møller polarimetry utilizes scattering the

polarized electron beam from polarized atomic electrons in a magnetized iron foil. The scattering rate is proportional to the beam and foil polarizations [65,67,68]. Such a measurement required the insertion of a magnetized foil into the beam path which inhibited normal data taking. A total of seven Møller measurements were made during the course of the experiment. This method has subpercent statistical accuracy, but a sizable systematic uncertainty mainly due to uncertainty in the target foil polarization. The total relative systematic uncertainty on the Møller measurement during this experiment was ∼2%.

The Compton polarimeter utilized $\vec{e}-\vec{\gamma}$ scattering to determine the polarization of the electron beam as the interaction is sensitive to the relative polarizations of the electrons and photons [69,70]. The newly commissioned polarimeter consisted of a magnetic chicane which deflected the electron beam toward a photon source and deflected unscattered electrons back toward the original beam path. At the center of the chicane was the photon source, a 700 mW laser at a wavelength of 1064 nm. The laser output was 400–500 W with a resonant Fabry-Pérot cavity [71]. The laser polarization for the left- and right-circular polarization states was $99\% \pm 0.02\%$ during the experiment [64]. There was also an electromagnetic calorimeter, a Gd_2SiO_5 crystal doped with cerium, for detecting scattered photons [72]. The electron detector was not used in this experiment.

The electron polarization was extracted from an asymmetry in the rate of scattering circularly polarized photons from the longitudinally polarized electrons, between two unique spin configurations: electron and photon spins parallel and antiparallel. The energy-weighted, integrated asymmetry was measured in a new integrating DAQ and then combined with the polarimeter's theoretically calculated analyzing power to determine the electron beam polarization [72,73]. Since Compton polarimetry is a noninvasive measurement, polarization measurements could be performed in parallel with data taking.

Combining the results of the Møller and Compton measurements for the three production run periods with polarized beam resulted in a beam polarization of $74\% \pm 1\%$ ($E = 5.89$ GeV), $79\% \pm 1\%$ ($E = 5.89$ GeV), and $63\% \pm 1\%$ ($E = 4.74$ GeV) [64].

3. Beam energy measurement

The beam energy was monitored throughout the experiment using the so-called Tiefenback method [74], which combined BPM measurements and the estimated integral of the magnetic field produced by the Hall A arc magnets. This method was calibrated against an invasive "arc energy" measurement. This measurement used the results of a detailed field mapping of all nine arc dipoles (including the reference one) after following a controlled excitation. In the actual arc energy measurement, all nine dipoles were excited following the same curve and the field was measured in the ninth dipole. The actual deflection of the beam was then measured, and the beam energy was computed from the deviation from the nominal bend angle of 34.3°. The uncertainty on such a measurement was $\delta E/E \approx 2 \times 10^{-4}$ [75]. Arc measurements were not performed during this experiment but were done for the immediately preceding experiment, E06-010 [76]. Their arc measurement was used as a reference for the Tiefenback measurements. The arc measurement conducted during E06-010 for ∼6 GeV beam energies yielded a value of $5889.4 \pm 0.5_{\text{stat}} \pm 1_{\text{syst}}$ MeV, while the Tiefenback measurement yielded $5891.3 \pm 2.5_{\text{syst}}$ MeV [76]. In our data analysis we used the Tiefenback measurements without correcting for the difference relative to the arc measurement, which was $\ll 1\%$.

E. The spectrometers

1. The left high-resolution spectrometer

The Hall A high-resolution spectrometers were designed for in-depth studies of the structure of nuclei and nucleons. The LHRS has high resolution in both the momentum and angle reconstruction of the scattered particles, in addition to the capability of running at high luminosity.

At the entrance of the LHRS there are two superconducting quadrupoles, for focusing the charged particles, followed by a superconducting dipole magnet that bends the charged particles upwards through a nominal 45° bending angle. After this, the particles pass through a third quadrupole before entering the detector stack. The LHRS has an angular acceptance of 6 msr, for a horizontal (vertical) angular resolution of 0.5 mrad (1 mrad). The momentum acceptance is 10% with a momentum resolution of 10^{-4}. The designed maximum central momentum is 4 GeV [65].

For E06-014 the LHRS detector stack was composed of a number of subpackages, located in the shield hut at the end of the magnet configuration. The detector subpackages included vertical drift chambers (VDCs), which provided tracking information for scattered particles, and the S1 and S2m scintillating planes served as the main trigger. Finally, the gas Čerenkov and the pion rejector yielded PID capabilities. The layout of the spectrometer is shown in Fig. 6.

The VDCs allowed precise reconstruction of particle trajectories. Each chamber had two wire planes containing 368 sense wires, spaced 4.24 mm apart [65]; the wires of a given plane were oriented orthogonally with respect to those in the other plane. The two wire planes lay in the horizontal plane of the laboratory, thus oriented at 45° with respect to the central (scattered) particle trajectory. Gold-plated Mylar high-voltage planes were placed above and below each wire plane at an operating voltage of −4 kV, thus setting up an electric field between the high-voltage planes. This defined a "sense region" for each wire plane.

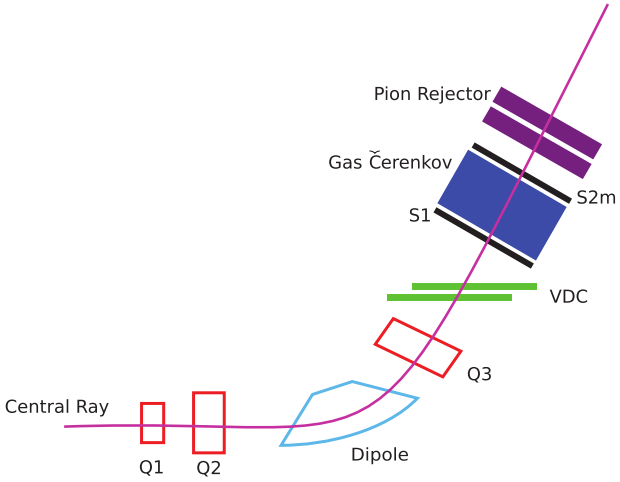

FIG. 6. The layout of the left high-resolution spectrometer in Hall A of Jefferson Lab during E06-014. Drawing not to scale.

The chambers were filled with a mixture of 62% argon and 38% ethane by weight. Traversing particles ionized the gas mixture; the ionization electrons drifted along the field lines to the closest sense wires, triggering a "hit" signal in the wires. A central track passing through at an angle of 45° fired five sense wires on average, resulting in a positional resolution of $\sim 100\ \mu$m and an angular resolution of ~ 0.5 mrad [65].

The gas Čerenkov had ten spherical mirrors, each with a focal length of 80 cm, stacked in two columns of five. Each mirror was viewed by a photomultiplier tube (PMT), placed 45 cm from the mirror. The chamber was filled with CO_2 gas at standard temperature and pressure with an index of refraction of 1.00043 [77]. This yielded a momentum threshold for triggering the gas Čerenkov of ~ 17 MeV for electrons and ~ 4.8 GeV for pions.

Incident particles were also identified using their energy deposits in the lead glass shower calorimeter, called a pion rejector. It was composed of two layers of 34 lead-glass blocks, the first 14.5 cm × 14.5 cm × 30 cm and the second 14.5 cm × 14.5 cm × 35 cm, made of the material SF-5, which has a radiation length of 2.55 cm [78]. The blocks were stacked so that the long dimensions of the blocks were transverse with respect to the direction of the scattered particle from the target. The gaps between the blocks in the first layer were compensated for by a slight offset in the second layer of blocks.

Since electrons and heavier particles like pions have different energy deposition distributions in electromagnetic calorimeters, we can distinguish between the two particle distributions. Electrons tend to leave most (if not all) of their energy in the calorimeter, while pions act like minimum ionizing particles (MIPs), leaving only a small amount of energy in the calorimeter. The energy loss of a MIP can be approximated by 1.5 MeV per g/cm^2 traversed [79]. With the density of SF-5 being ~ 4 g/cm^3 [77], pions deposited ~ 175 MeV in the calorimeter (both layers of the pion rejector taken together). As a result there are two distinct peaks in the energy distribution with good separation in the calorimeter: one due to pions and the other due to electrons. This allows the selection of electrons in the analysis while rejecting pions.

Figure 7 shows a typical signal distribution in the gas Čerenkov. Electron (pion) candidates are indicated by the distributions centered at ~ 6.5 photoelectrons ($\lesssim 2$ photoelectron) in Fig. 7, that are obtained by placing cuts on the pion rejector signals. While scattered electrons yielded an ADC signal corresponding to the main photoelectron peak in the gas Čerenkov, pions may also influence the ADC spectrum. This occurs because pions could have ionized the atoms of the gaseous medium in the Čerenkov, producing electrons with enough energy to trigger the detector. Such electrons are called δ rays, or *knock-on electrons*. The distribution of these electrons has a peak at the one-photoelectron peak (leftmost peak in Fig. 7) with a long tail underneath the multiple (main) photoelectron peak. These knock-on electrons can effectively be removed in the analysis because on average they deposited a small amount of energy in the pion rejector. To identify electrons the ratio E/p of the energy deposited in the pion rejector and the reconstructed momentum was required to be greater than 0.54, as illustrated in Fig. 8 (Sec. II G). Additionally, events that deposited less than 200 MeV in the first layer of the pion rejector were removed from the analysis, as they were likely to be pions or knock-on electrons.

There were two planes of plastic scintillating material, labeled S1 and S2m. S1 was composed of six horizontal

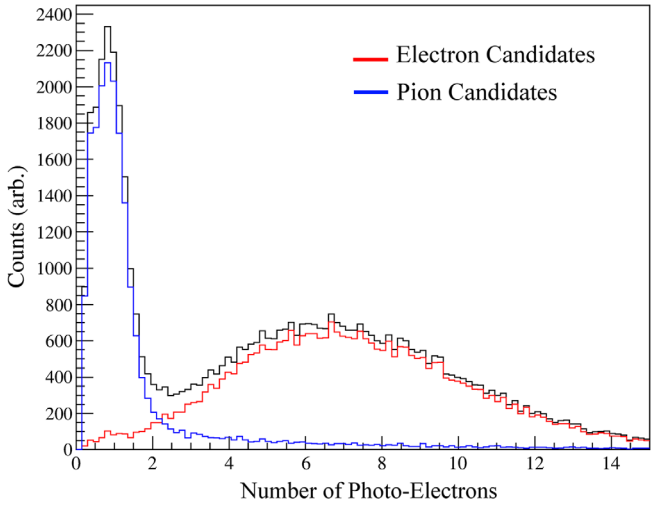

FIG. 7. A typical signal distribution in the LHRS gas Čerenkov (black curve). Electron (pion) candidates were selected by placing cuts on the energy deposited in the pion rejector, described by $E/p > 0.54$ ($E/p < 0.54$) and for the energy deposited in the first layer of the pion rejector to be greater than (less than) 200 MeV. Electrons are indicated by the distribution centered at ~ 6.5 photoelectrons, while pion candidates have their distribution peaked at ~ 1 photoelectron.

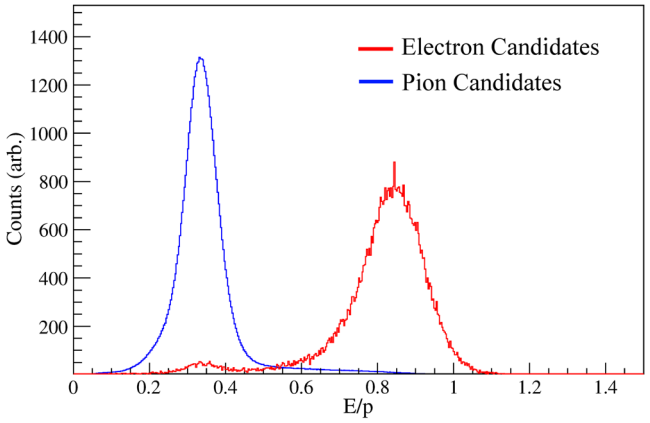

FIG. 8. A typical signal distribution in the LHRS pion rejector layers, where the particle's total deposited energy divided by its reconstructed momentum is plotted. Electron (pion) candidates are shown by the distributions on the right (left), as selected by placing a cut on the gas Čerenkov signal to be greater than (less than) two photoelectrons.

scintillating paddles with 36 cm × 29.3 cm × 0.5 cm active volume. Each paddle was viewed by a 5.1 cm-diameter PMT on each end. The paddles overlapped by 10 mm, oriented at a small angle with the S1 plane. The S2m plane consisted of 16 nonoverlapping paddles with dimensions of 43.2 cm × 14 cm × 5.1 cm. The timing resolution of the PMTs used for each plane was ∼50 ps [80].

When a paddle absorbed ionizing radiation, it emitted light which traveled down the length of the paddle and was collected by the PMTs attached at each end. The timing information encoded in the PMTs' time-to-digital converters (TDCs) is utilized in the formation of the LHRS main trigger, discussed in Sec. II F.

2. The BigBite spectrometer

The BigBite spectrometer is a large-acceptance spectrometer, able to detect particles over a wide range in scattering angle and momentum. BigBite consists of one large dipole magnet, capable of producing a maximum magnetic field of ∼1.2 T. The magnet entrance was located 1.5 m from the target center, resulting in an angular acceptance of about 64 msr. Charged particles with momenta of ∼0.5 GeV entering the magnet near its optical axis are then deflected roughly 25° for a total trajectory of 64 cm when the field is 0.92 T [81]. The momentum range covered by the spectrometer at full field had a lower bound of roughly 0.6 GeV. In its standard configuration, the magnet bent negatively charged particles upwards into the detector stack, while positively charged particles were deflected downwards. The large acceptance of the spectrometer allowed the detection of both negatively and positively charged particles. The detector stack for E06-014 included multiwire drift chambers for particle tracking, a newly installed gas

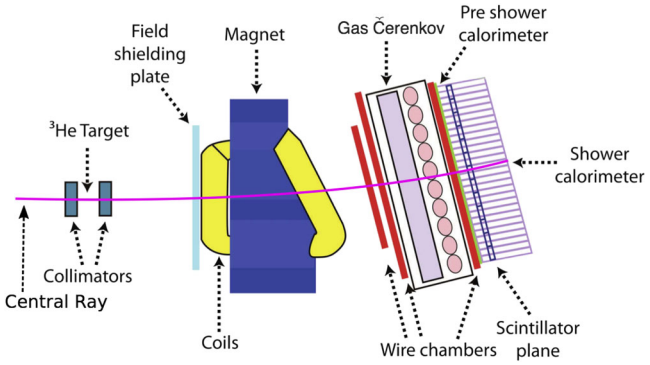

FIG. 9. The layout of the BigBite spectrometer in Hall A of Jefferson Lab. Drawing not to scale. The central ray drawn here is for a path similar to what a 1.7 GeV electron would take through the magnet. Figure modified from [80].

Čerenkov, a scintillator plane, and an electromagnetic calorimeter, composed of a preshower and shower calorimeter. The gas Čerenkov, scintillator plane, and the preshower and shower calorimeters were used for PID purposes. The schematic layout of BigBite is shown in Fig. 9.

The multiwire drift chambers were utilized for particle tracking, in much the same way as described for the VDC planes in the LHRS. There were three chambers, each filled with a 50–50 mixture of argon and ethane gas. Each chamber had three pairs of wire planes, giving a total of 18 planes in all. Each of the 18 planes was perpendicular to the detector's central ray (Fig. 9), bounded by cathode planes 6 mm apart from one another. Halfway between the cathode planes was a plane of wires, composed of alternating field and sense wires. The field wires and the cathode planes were held at the same constant high voltage, producing a nearly symmetric potential in the region close to the sense wires. Each pair of wire planes had a different orientation so as to optimize track reconstruction in three dimensions. The two so-called X planes (X, X') ran horizontally (in detector coordinates), while the U and V planes were oriented at +30° and −30° with respect to the X planes, respectively. The wires in each plane were 1 cm apart and the primed planes (X', U', V') were offset from their unprimed counterparts by 0.5 cm. This allowed the tracking algorithm to determine if the track passed above or below a given wire in the X plane based upon which wire registered a hit in the X' plane, for example. This alignment resulted in a positional resolution of less than 300 μm [62].

The gas Čerenkov, which was constructed by Temple University specifically for this experiment [82], included 20 spherical mirrors, each with a focal length of 58 cm, stacked in two columns of ten. The chamber was filled with the gas C_4F_8O, which has an average index of refraction of 1.00135 [62]. Čerenkov light incident on each mirror was reflected onto a corresponding secondary flat mirror. This mirror then directed the Čerenkov light onto the face of a corresponding PMT. To boost the amount of light collected, each PMT was fitted with a cone similar to a Winston cone

[83]. This extended the effective diameter of each PMT collection area from 5 in. to 8 in. The PMTs were recessed 5 in. within their shielding in order to reduce the effects of the BigBite magnetic field. The resulting gap between the PMT face and the edge of the shielding was filled with a cylindrical lining of Anomet UVS reflective material, so as to direct light incident upon this region onto the PMT face. Figure 10 shows a typical signal distribution in the gas Čerenkov. Electron (pion) events are indicated by the right (left) distributions. Electron events for a given PMT were identified by selecting those events that had a hit in their corresponding TDC with a projected track from the target that fell within the PMT's geometrical acceptance.

The calorimeter was composed of two layers of lead-glass blocks. The first layer was the preshower, composed of the material TF-5, which has a radiation length of 2.74 cm. The preshower was located 85 cm from the first drift chamber plane. It contained 54 blocks of dimensions 35 cm × 8.5 cm × 8.5 cm. They were organized in two columns of 27 rows. The long dimension of each block was oriented transverse with respect to scattered particles coming from the target. The shower layer was composed of the material TF-2, which has a radiation length of 3.67 cm and was located 15 cm behind the preshower and 1 m from the first drift chamber. It had 189 blocks of the same dimensions as the blocks in the preshower, but they were organized in seven columns and 27 rows. The long dimension of the block was oriented along the scattered particle path, ensuring the capture of a large amount of the electromagnetic shower of the particle [84].

The plane located between the preshower and the shower was a scintillator plane composed of 13 paddles of plastic scintillator, each of which had a PMT at each end with a timing resolution of 0.3 ns. Each paddle had the dimensions 17 cm × 64 cm × 4 cm. The first dimension was transverse with respect to the scattered particles, while the short dimension was along the scattered particle path. This resulted in an active area of 221 cm × 64 cm. This plane provided an additional source of pion rejection to complement the gas Čerenkov and the shower calorimeter, as the charged pions left a significant signal in the low end of the ADC spectrum via knock-on electrons [62].

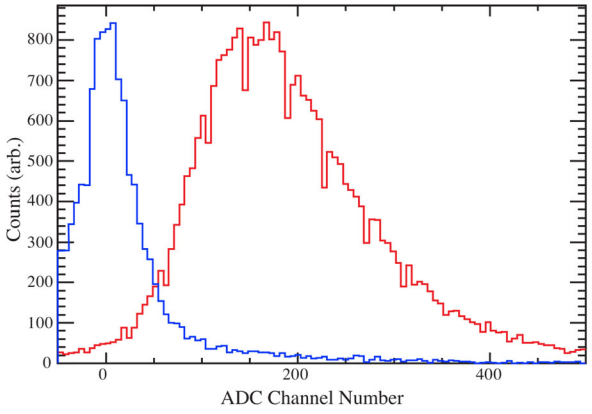

FIG. 10. Signal distributions in the BigBite gas Čerenkov. Electron (pion) events are shown by the right (left) distributions.

F. Data acquisition and data processing

In this experiment, the CEBAF Online Data Acquisition [85] system was used to process the various trigger signals and data coming from the LHRS and BigBite spectrometers, beam line, and target equipment. The LHRS and the BigBite detector systems were run independently with a total of 5 TB of data recorded.

Eight triggers were configured for E06-014, summarized in Table III. The T8 trigger was used for troubleshooting purposes only. It was a 1024 Hz clock, injected into the data stream to ensure that the electronics were working correctly. The T5 trigger was the coincidence (coin.) trigger between the LHRS and BigBite, used for optics calibration purposes.

The generation of the main LHRS trigger (T3) required a hit in both scintillating planes S1 and S2m, where a hit in a single plane corresponded to a signal in the two PMTs affixed to a paddle (left and right sides) in a plane. Thus, a T3 trigger corresponded to a pulse detected in four PMTs, two in the S1 plane and two in the S2m plane. The timing of this trigger was set by the leading edge of the TDC signal recorded in the PMT attached to the right side of the S2m scintillator paddles [66]. The second LHRS trigger was the T4 trigger. The only difference between the T3 and T4 triggers was that a T4 was generated when there was a coincidence between either S1 or S2m and the gas Čerenkov detector, *without* generating a T3 trigger. The T4 trigger was used to study the efficiency of the T3 trigger, as these events were potentially good events since they generated a signal in the gas Čerenkov. It was found that the efficiency of the T3 trigger was 99.95% over the course of the experiment [86].

The BigBite spectrometer had four dedicated triggers, T1, T2, T6, and T7. The T1 and T6 triggers involved taking the hardware (voltage) sum of the calorimeter blocks belonging to the cluster with the largest signal, where a cluster for the preshower and shower calorimeters was defined as two adjacent rows of calorimeter blocks. There

TABLE III. Triggers used during E06-014.

Trigger	Spectrometer(s)	Description
T1	BigBite	Low shower threshold
T2	BigBite	Coin. of T6 and T7
T3	LHRS	Coin. of S1 and S2m
T4	LHRS	Coin. of either S1 or S2m and Čerenkov
T5	LHRS, BigBite	Coin. of T1 and T3
T6	BigBite	High shower threshold
T7	BigBite	Gas Čerenkov
T8	LHRS, BigBite	1024 Hz Clock

are 26 clusters each for the preshower and shower calorimeters. The sum of the preshower and shower signals was then formed and sent to a discriminator. If this signal was greater than ∼300–400 MeV (∼500–600 MeV), then the T1 (T6) trigger was formed. The T7 trigger was formed in a manner similar to the T1 and T6 triggers, but using the Čerenkov detector instead of the preshower or shower calorimeter. The Čerenkov signals from two adjacent rows of mirrors (four mirrors in total) were summed, resulting in nine overlapping mirror clusters. If this sum was larger than the set threshold value (> 1–1.5 photoelectrons), then the T7 trigger was formed. The main trigger for the BigBite spectrometer, T2, imposed a geometric constraint on the incident particle track by requiring a coincidence between the geometrically overlapping regions in the gas Čerenkov and the calorimeter. An example of an event that generated a T2 trigger is illustrated in Fig. 11: a particle that triggered cluster C1 in the gas Čerenkov would also have to trigger at least one of the clusters A–D in the calorimeter. Similar coincidences were imposed for the eight other groupings that could form a T2 trigger.

The raw data were processed by the Hall A Analyzer [87], which is based on ROOT [88]. Specific C++ classes were written to interpret the data recorded by the various detectors and their subdetectors. For instance, there are classes that convert the ADC signals registered in a calorimeter block into the corresponding amount of energy deposited. There are also classes that handle the computation of a particle's path (or track) through the LHRS (and BigBite) up to its focal plane and its reconstructed vertex position back at the target. The optics for BigBite required special attention, as discussed in [62,64,80].

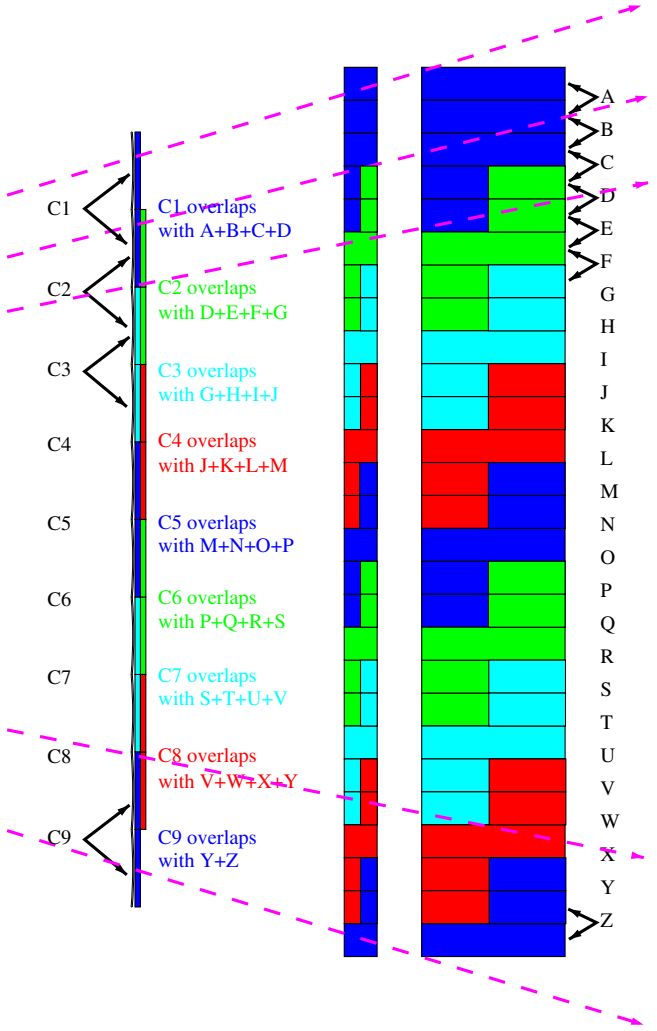

FIG. 11. The geometrical overlap for the main trigger for the BigBite spectrometer. The Čerenkov mirrors are represented by the leftmost column, where the cluster groupings are labeled by Ci, with $i = 1, \ldots, 9$. The preshower blocks are shown as the middle column of colored blocks, while the shower blocks are the long blocks in the rightmost column. The calorimeter cluster groupings are labeled with the letters A–Z. The dashed lines indicate typical electron paths at the extremes of the acceptance of the BigBite spectrometer.

G. Particle identification

The LHRS and the BigBite spectrometers each utilized a gas Čerenkov detector and a double-layered lead-glass shower calorimeter for PID purposes. In this experiment, PID corresponds to distinguishing electrons from pions, which constituted the primary background.

The PID performance of each detector was characterized by the efficiencies of the conditions (or cuts) placed on the corresponding observable. Before PID cut efficiencies were evaluated, the sample distribution of events to be studied was selected using data quality criteria (such as removing beam trips) and conditions to remove events that may have originated in the target's glass end caps [62,86]. The electron cut efficiency ε_e is defined as the ratio of the number of events that pass a given cut to the size of the electron event sample defined by another detector. For the gas Čerenkov, the electron sample was chosen by using the calorimeter, and vice versa. To characterize how well a given detector can reject pions, the rejection factor $f_{\pi,\mathrm{rej}}$ is evaluated. It is defined as the ratio of the size of the selected pion sample to the number of events misidentified as electrons for a given cut. The PID cuts were chosen such that the pion rejection was maximized while the highest electron efficiency was maintained.

In the momentum acceptance range of the experiment, 0.6 GeV $\leq p \leq$ 1.7 GeV, the electron cut efficiency for the LHRS gas Čerenkov was found to be $\varepsilon_e^{\mathrm{cer}} \approx 96\%$ for a cut of greater than two photoelectrons in the ADC. For the LHRS pion rejector, $\varepsilon_e^{\mathrm{pr}} \approx 99\%$ for $E/p > 0.54$. These efficiencies are critical for the LHRS data since they contribute directly in the determination of the unpolarized cross section (Sec. IV B). The pion rejection factor was found to be ∼660 for both the gas Čerenkov and pion

rejector, resulting in a combined rejection of $f_{\pi,\mathrm{rej}} \approx 4 \times 10^5$ [86]. As a result, the pion contamination in the final electron sample was negligible.

PID studies were also conducted for the data recorded by BigBite. Here, the pion rejection factor was determined to be better than 2×10^4 when combining the pion rejection capabilities of the gas Čerenkov [89], preshower and shower calorimeters, and the scintillator plane [62]. Unlike the cross section analysis using the LHRS data, the electron cut efficiencies do not play a role in the asymmetry extraction that is performed using the BigBite data; the efficiencies cancel in the asymmetry definition (Sec. IV C).

III. POLARIZED ^{3}He TARGET

Since the lifetime of the neutron is less than 15 min [90] outside the nucleus, a free-neutron target is not practical. ^{3}He, a spin-1/2 nucleus consisting of two protons and a neutron, is a candidate for a polarized neutron target. Deuterium, a spin-1 nucleus consisting of a proton and a neutron, is another option. Both nucleons in deuterium have their spins aligned with the nuclear spin. However, large corrections due to the proton result in large uncertainties when using a deuterium target. When ^{3}He is polarized, there are three principal states in play: ~90% of the time the nucleus is in the symmetric S state; ~1.5% of the time the nucleus is in the S' state; and ~8% of the time the nucleus is in the D state; see Fig. 12. In the S state, the spins of the protons are antiparallel to one another, resulting in the neutron carrying the majority of the ^{3}He polarization [60]. As a result, a polarized ^{3}He target can be used as an effective polarized neutron target.

In this experiment, polarized ^{3}He ($\vec{^3\mathrm{He}}$) was used to study the electromagnetic structure and the spin structure of the neutron. Two major methods exist to polarize ^{3}He nuclei. The first one uses the metastable-exchange optical pumping technique [91], while the second method utilizes both spin-exchange [92] and optical pumping [93], dubbed *hybrid spin-exchange optical pumping*.

^{85}Rb atoms were optically pumped using 795 nm circularly polarized laser light, inducing the D1 transition in ^{85}Rb: $5^2S_{1/2}$ $(m = -1/2) \rightarrow 5^2P_{1/2}$ $(m = +1/2)$, in accordance with the selection rule of $\Delta L = +1$. The excited ^{85}Rb electrons decay from the p orbital to the s orbital with equal probabilities for the $m = \pm 1/2$ substates, but the excitation occurs only for the $m = -1/2$ initial state of the s orbital; this results in the selective population of the $m = 1/2$ state of the s orbital. Second, the polarization of the ^{85}Rb atoms was transferred to ^{39}K atoms via spin-exchange binary collisions [92]. In the third and final step, the polarization of the ^{85}Rb and ^{39}K atomic electrons was transferred to the ^{3}He nuclei via the hyperfine interaction, where the nuclear spin of ^{3}He takes part in the process [94]. The use of ^{39}K greatly decreases the spin-relaxation rate for collisions involving ^{3}He, resulting in an increase in the spin-exchange efficiency of the polarization process [95].

As the atomic electrons decayed to the ground state, photons were emitted. These photons were typically unpolarized, and therefore reduced the efficiency of the pumping process. To minimize this effect for the alkali atoms, a small amount of N_2 buffer gas was added to the cell. The excitation energy of the alkali atoms was passed to the rotational and vibrational modes of the buffer gas via collisions, reducing the emission of photons [92].

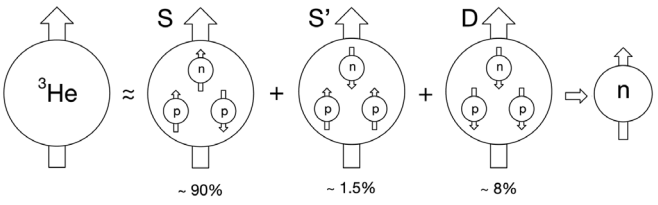

FIG. 12. ^{3}He ground states. The dominant state is the S state, where ~90% of the polarization is carried by the neutron. In this state, the protons pair to $s = 0$.

A. Setup

The target apparatus was composed of a number of different elements: the target cells, target oven, target ladder system, Helmholtz coils for the holding magnetic field, RF coils, and polarizing lasers. The layout of the target system is shown in Fig. 13. The outer circle and large straight lines intersecting at right angles inscribed in the large circle represent Helmholtz coils. The smaller vertical straight lines and circle overlapping with the Helmholtz coils signify the RF coils. Pickup coils mounted near the target cell are also shown.

Two pairs of Helmholtz coils, capable of producing magnetic fields in two orthogonal directions, were utilized in E06-014: longitudinal (along the direction of the beam),

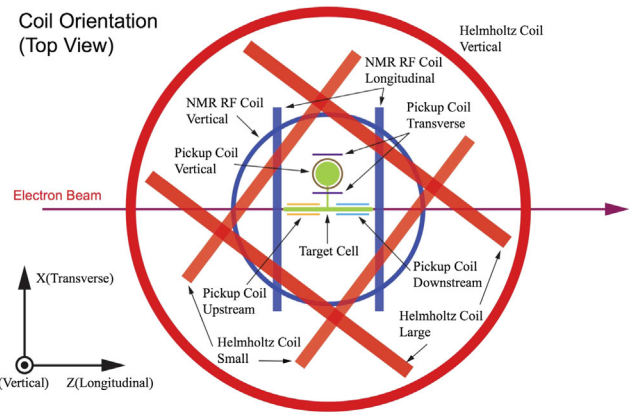

FIG. 13. The target setup. The Helmholtz coils for the holding magnetic field and coils for the RF field are shown. The pickup coils near the target cell are used for nuclear magnetic resonance (NMR) measurements. Figure reproduced from [65].

and transverse in-plane (perpendicular and horizontal to the beam). The field reached a magnitude of 25 G, requiring ∼7 A of current in each coil. The RF coils and pickup coils are important for the measurement of the target polarization, as presented in Secs. III D and III E.

B. Target cells

The production target cell, named Samantha, is shown schematically in Fig. 14. The upper chamber, called the pumping chamber, contained ^{3}He, alkali metals (^{85}Rb and ^{39}K at equal densities), and N_2, with number densities of 10^{20} cm^{-3}, 10^{14} cm^{-3}, and 10^{18} cm^{-3}, respectively [96]. This chamber was heated to ∼265 °C in order to keep the Rb and K in a gaseous state. The polarization process took place in this chamber. The polarized ^{3}He gas (with the N_2 mixture) flowed through a thin transfer tube to the target chamber, thanks to the temperature gradient between the pumping chamber and the target cell that was kept at room temperature. This chamber was 40 cm long and contained ∼8 atm of ^{3}He and ∼0.13 atm of N_2 during the experiment. The temperature of the cell was monitored via resistive temperature devices (RTDs), which were placed equidistant from one another along the length of the target chamber, along with two more placed on the pumping chamber; one at the top and the other at the base. The production cell was made out of aluminoscilicate glass (GE-180), which was filled and characterized at the University of Virgina and the College of William and Mary [66]. This characterization consisted of measuring the polarization, gas density, glass thickness of the cell, and rate of polarization.

An additional reference cell was used [97], which could be filled with H_2, N_2, or ^{3}He. This allowed the determination of the dilution factors that contribute to the cross sections and asymmetries. RTDs were also mounted on the reference cell to monitor its temperature, in a similar configuration as was done for the target cell. A multicarbon foil ("optics") target—as well as the reference cell filled with hydrogen gas—was used for the calibration of the optics for the two spectrometers. All of these targets were mounted on a target ladder, which could be moved vertically up and down to select the target needed. In addition to these targets, a "no target" position was available, corresponding to a hole in the target ladder. It was used during Møller polarimeter measurements, so that the target assembly would not be damaged in the process.

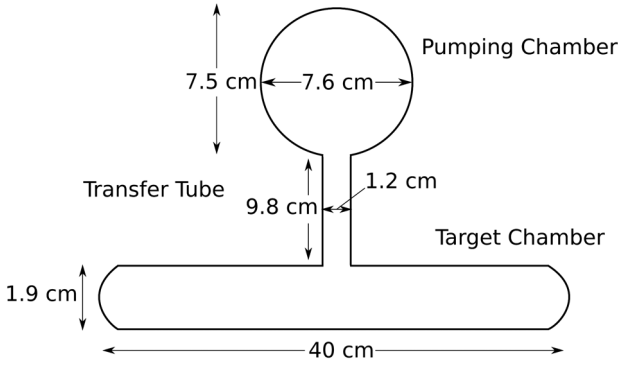

FIG. 14. The production target cell used in our experiment. The top spherical chamber is the pumping chamber where the polarization of ^{3}He takes place. The long cylindrical chamber is the target cell, through which the electron beam passes longitudinally. The thin tube connecting these two chambers is the transfer tube, which allows polarized ^{3}He to drift down into the target chamber. Drawing not to scale.

C. Laser system

Our experiment utilized an upgraded laser system that had been installed for the immediately preceding experiment, E06-010 [76]. These new COMET lasers had a linewidth of 0.2 nm, a factor of 10 less than that of their predecessors (FAP lasers [98–100]). This dramatically improved the optical pumping efficiency, since a narrower linewidth results in proportionately more photons exciting the desired atomic transitions in ^{85}Rb, so that a higher polarization of ^{3}He atoms could be attained in a shorter time frame [96].

The laser setup is shown in Fig. 15. It consisted of three COMET lasers, each with a power of 25 W and a wavelength of 795 nm, used to optically pump the ^{85}Rb in the pumping chamber. The lasers were installed in a separate laser building behind the counting house on the accelerator

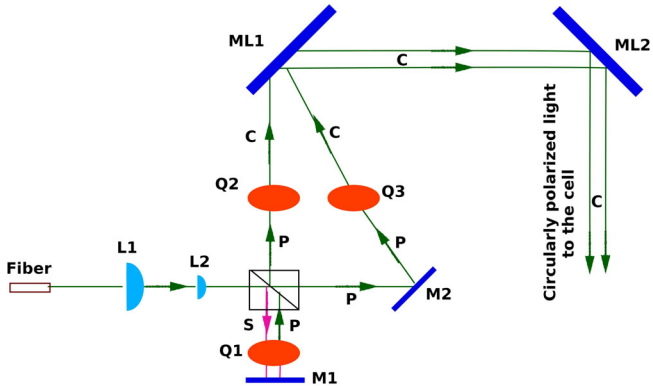

FIG. 15. The laser system used to polarize ^{85}Rb atoms. The symbols labeled L1 and L2 are lenses, while symbols labeled as M and ML are mirrors. Light reflected from ML2 is incident upon another mirror (not shown) which is attached to the oven. Quarter wave plates are indicated by Q1, Q2, and Q3. The beam-splitting polarization cube (BSPC) is represented by the rectangle with a slash through it. The initial unpolarized laser light is split by the BSPC into S- and P-wave components, where the P-wave component has linear polarization and passes through the beam splitter. The S-wave component is converted into a P-wave by Q1. The motorized quarter-wave plates Q2 and Q3 convert P-wave light into circularly polarized light, labeled C. Figure reproduced from [62].

site at JLab. The fiber coming out of each COMET control unit was connected to a 75-m-long fiber that ran from the laser building to the hall. Then the fiber was connected to a 5-to-1 combiner. The output of the combiner was sent to a beam splitter, yielding two linearly polarized components. One component passed twice through a quarter-wave plate, after which both had the same linear polarization. Sending each component through another quarter wave plate converted the linear polarization into circular polarization. The resulting beams were then combined into one, with a spot size of 7.5 cm in diameter, the size of the pumping chamber [96]. There were three optics lines corresponding to the longitudinal, transverse, and vertical polarization directions. The polarizing optics were set up in an antiparallel pumping configuration such that the target spin was always oriented opposite to the magnetic holding field [62].

D. EPR measurements

The target polarization was measured in an absolute sense through an electron paramagnetic resonance (EPR) measurement that utilized Zeeman splitting of the electron energy levels when an atom was placed in an external magnetic field. This phenomenon occurred for the ^{85}Rb and ^{39}K atoms, which were present in the pumping chamber. The ground states of the alkali metals split into $2F+1$ energy levels, where F is the total angular momentum quantum number. Specifically, for ^{85}Rb, the $F=3$ ground state split into seven sublevels corresponding to $m_F = -3,\ldots,3$. For ^{39}K, the $F=2$ ground state split into five energy levels, given by $m_F=-2,\ldots,2$. The splitting corresponded to a frequency that is proportional to the holding field. This frequency was shifted due to the small effective magnetic field created by the spin-exchange mechanism of ^{85}Rb-^{39}K and ^{39}K-^{3}He, in addition to the polarization of the ^{3}He nuclei.

When the EPR transition was excited, an alkali metal (either Rb or K as chosen by the excitation frequency) lost its polarization. When one of the metals was depolarized, so was the other due to the fast spin-exchange mechanism. Upon repolarization of the Rb atoms, there was an increase in the photons emitted corresponding to the $P_{1/2}\rightarrow S_{1/2}$ (D1) transition (795 nm). However, because of thermal mixing between the $P_{1/2}$ and $P_{3/2}$ energy states and occasional collisional mixing with N_2 in the cell, the $P_{3/2}\rightarrow S_{1/2}$ (D2) transition (780 nm) was possible. While the amount of D1 and D2 fluorescence was roughly the same [96], the D1 light was suppressed due to a large background component corresponding to the polarizing laser light. Therefore, a filter was attached to a photodiode to identify the D2 light. During the measurement, the RF was modulated with a 100 Hz sine wave, and the D2 transition was synchronized to this modulating signal and measured by a lock-in amplifier. The signal from the lock-in output was proportional to the derivative of the EPR fluorescence curve as a function of the RF; the EPR resonance occurred when the derivative was equal to zero [96,101]. EPR measurements were performed every few days.

To determine the polarization in the target chamber, a model [102–105] was used to describe the diffusion of the ^{3}He polarization from the pumping chamber to the target chamber. The relative systematic error of the measurement was ∼4%, dominated by the uncertainties on the dimensionless constant κ_0 [106] and the number density of the gas in the pumping chamber [62].

E. NMR measurements

Another method we used for measuring the polarization of the ^{3}He nuclei was measuring the ^{3}He nuclear magnetic resonance signal. The magnetic moments of ^{3}He nuclei aligned along the direction of an external magnetic holding field had their direction reversed by applying an RF field in the perpendicular direction. Sweeping the frequency of the RF field through the resonance of the ^{3}He nucleus flipped the spins of the nuclei. This spin flip changed the field flux through the pick-up coils (Fig. 13), inducing an electromotive force. The signals from the coils were preamplified and combined, and then sent to a lock-in amplifier. The magnitude of the final signal was proportional to the ^{3}He polarization.

The RF is swept according to the adiabatic fast passage technique [107], in which the sweep through the resonant frequency is done faster than the spin-relaxation time, but slowly enough so that the nuclear spins can follow the sweep of the RF field. This minimizes the effect of these NMR measurements on the target polarization.

An NMR measurement is a relative measurement, so it needs to be compared against a known reference. A measurement of NMR on water is typically used, for which the polarization can be calculated exactly from statistical mechanics [108]. However, in E06-014, water-cell measurements were available only for the longitudinal target polarization configuration, as conversion factors needed to account for the different positions of the water and ^{3}He cells could not be measured for the transverse configuration [62]. Because of this, the NMR measurements were calibrated against EPR measurements (Sec. III D) that were done close in time relative to the NMR measurements. The NMR water measurements in the longitudinal configuration were used as a cross-check against the EPR measurements and were found to be consistent to the 1% level. NMR measurements were performed every four hours on the production ^{3}He target. The systematic error on the NMR measurement was ∼3.9% (relative), dominated by the uncertainties on the EPR calibration and on the computed magnetic flux through the pickup coils [62].

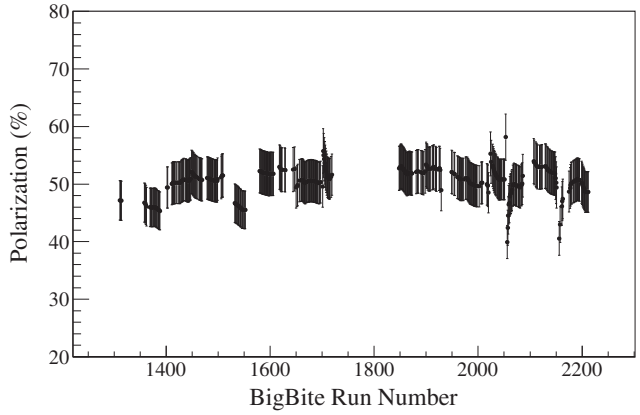

FIG. 16. The ^{3}He target polarization as a function of BigBite run number.

F. Target performance

The target polarization over the course of the experiment, extracted from NMR measurements, is shown in Fig. 16. In the data analysis (Sec. IV C), the target polarization data were utilized on a run-by-run basis. On average, the target polarization achieved was 50.5% with a relative uncertainty of 7.2% (3.6% absolute). The dominant contribution to the uncertainty was from the calibration of the NMR measurements against the EPR measurements (3.9% relative) and the loss of polarization due to the diffusion of polarized ^{3}He from the pumping chamber to the target chamber (6% relative).

IV. DATA ANALYSIS

A. Analysis procedure

The analysis procedure is outlined in Fig. 17, which shows that the raw data were first replayed, followed by the calibration and data quality checks. Data calibrations included gain-matching ADC readings within the gas Čerenkov and shower calorimeters to have the same responses for a given type of signal. Calibrations also involved optimizing the software packages that describe the optics of the two spectrometers. Multifoil carbon targets, a sieve slit collimator, and elastic $^1\mathrm{H}(e,e')p$ data at an incident energy of $E = 1.23$ GeV were used to calibrate the optics software package for the LHRS [76] and for the BigBite spectrometer. The momentum resolution achieved for the BigBite spectrometer was ∼1% [62]. Data quality checks implied checking the calibration results and removing beam trips from the data. Faulty runs (e.g., those having poor beam quality, detector live times $\lesssim$80%, run times less than a few minutes) were also identified and discarded from the analysis.

Following calibration and data quality checks, the electron sample was cleaned up by removing events that did not generate a good trigger or had poor track reconstruction. Cuts were also made to remove pion tracks

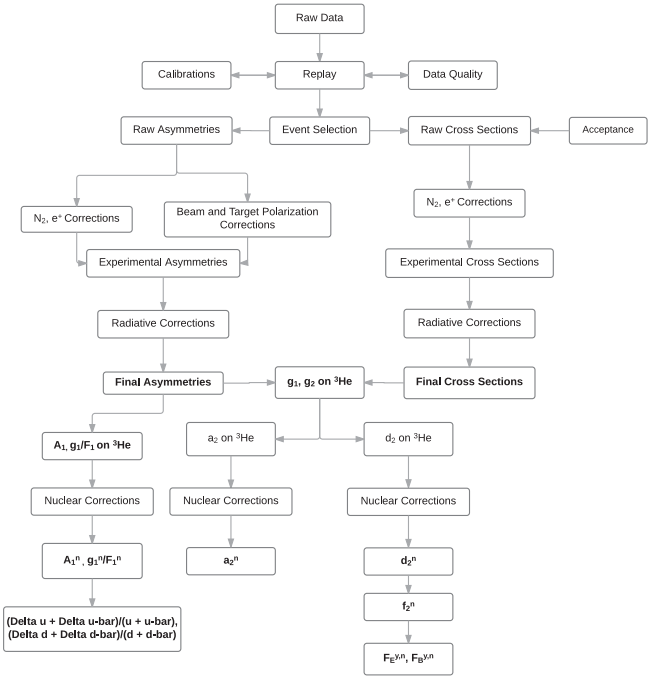

FIG. 17. The data analysis procedure.

and events originating in the target window. In the BigBite data set, geometrical cuts had to be implemented to remove events that rescattered from the BigBite magnet pole pieces. After all cuts had been applied to the data, the raw physics observables consisting of cross sections and asymmetries were then extracted. Corrections were applied to account for the nitrogen target contamination and background due to pair-produced electrons, neither of which could be removed by cuts. After these corrections were applied, we obtained the experimental cross sections (Sec. IV B) and the experimental asymmetries (Sec. IV C). Applying radiative corrections yielded the final quantities for each of those, from which the spin structure functions g_1 and g_2 on ^{3}He were extracted as described in Appendix A 6. The ^{3}He results for the unpolarized cross sections, double-spin asymmetries, and spin structure functions g_1 and g_2 are presented in Sec. V A. The Lorentz color force $d_2^{^3\mathrm{He}}$ was obtained from Eq. (17), after which nuclear corrections (Sec. IV D) were applied to obtain d_2^n (Sec. V B 1). From the $g_1^{^3\mathrm{He}}$ data the a_2 matrix element on ^{3}He (given as the third moment of g_1) was extracted. Nuclear corrections, similar to those used for d_2, were applied to obtain a_2^n (Sec. V B 2). From a twist expansion of world data for Γ_1^n, the twist-4 matrix element f_2^n was obtained using our d_2^n data as input (while the value of a_2^n was taken from an average over the available model calculations; see Sec. V B 3). Additionally, $A_1^{^3\mathrm{He}}$ and $g_1^{^3\mathrm{He}}/F_1^{^3\mathrm{He}}$ were extracted with the aid of Eqs. (18) and (19). Nuclear corrections were then applied to the ^{3}He results to obtain the neutron quantities (Secs. V B 4 and V B 5). Using the

g_1^n/F_1^n data obtained, we then extracted the flavor-separated ratios $(\Delta u+\Delta\bar{u})/(u+\bar{u})$ and $(\Delta d+\Delta\bar{d})/(d+\bar{d})$ (Sec. V C).

B. Cross sections

1. Extraction of raw cross sections from data

The unpolarized differential cross section was calculated from the data for a given run as follows:

$$\frac{d^3\sigma_{\rm raw}}{d\Omega dE'} = \frac{t_{\rm ps}N_{\rm cut}}{(Q/e)nt_{LT}\varepsilon}\frac{1}{\Delta E'\Delta\Omega\Delta Z}, \tag{28}$$

where $t_{\rm ps}$ denotes the prescale value for the T3 trigger [109], $N_{\rm cut}$ the number of electrons that pass all cuts, Q/e the number of beam electrons delivered to the target, n the target number density in amagats [110], t_{LT} the live time [111], and ε the product of all detector (cut) efficiencies. The quantity $\Delta E' = \delta p/p_0 \cdot p_0$, where $\delta p/p_0 = (p-p_0)/p_0$ is the scattered momentum of the electron p relative to the LHRS momentum setting p_0. Electrons were selected according to the criterion $|\delta p/p_0| < 3.5\%$, which was based on the agreement of the Monte Carlo simulation of the spectrometer (see below) with the data [86]. The quantity ΔZ denotes the effective target length seen by the spectrometer, measured in meters. The cut on the effective target length was chosen such that the target windows and edge effects due to scattering from the magnets in the LHRS are removed. The term $\Delta\Omega$ denotes the solid-angle acceptance, measured in steradians; it is defined as the product of the in-plane scattering angle $\Delta\theta$ and out-of-plane scattering angle $\Delta\phi$. The cut chosen for $\Delta\theta$ ($\Delta\phi$) was ± 40 mrad (± 20 mrad), which amounts to a solid angle of 3.2 msr. The cuts on $\delta p/p_0$, ΔZ, $\Delta\theta$, and $\Delta\phi$ were informed by looking at a Monte Carlo simulation of the LHRS.

The effective acceptance was determined with the Single-Arm Monte Carlo (SAMC) simulation [112]. To determine how the geometrical acceptance of the LHRS deviates from the ideal rectangular acceptance, SAMC began by generating events originating from the target that were uniformly distributed over the kinematical phase space. Each event was then transported to the focal plane using an optical model of the LHRS [113]. As the particle encountered each magnet aperture in the LHRS, a check was performed to see if it successfully passed through the known apertures. If the simulated particle successfully made it through all geometrical apertures, it was then reconstructed back to the target using the optics matrix optimized during the experiment. The ratio r of the number of reconstructed events to the number of generated events was used to determine the effective acceptance, written as $r = \Delta E'\Delta\Omega\Delta Z/\Delta E'_{\rm MC}\Delta\Omega_{\rm MC}\Delta Z_{\rm MC}$. The subscript MC refers to the initially generated kinematic phase space in the simulation, chosen to be larger than the apertures of the LHRS, so as to avoid edge effects.

The cross sections extracted for each run of a given momentum bin were then averaged, weighted by their statistical errors,

$$\langle\sigma\rangle = \frac{\sum_{i=0}^{n}\sigma_i\frac{1}{\delta\sigma_i^2}}{\sum_{i=0}^{n}\frac{1}{\delta\sigma_i^2}}, \tag{29}$$

where $\delta\sigma_i$ is the statistical error on the cross section for the ith run.

2. Background corrections

The raw ^{3}He cross section measured in the LHRS, $\sigma_{\rm raw}$, contains contributions from electrons that were not scattered from ^{3}He, but were produced in processes corresponding to electron-positron (pair) production (arising from π^0 mesons decaying predominantly to photons), or scattering from nitrogen nuclei.

To remove the pair-production contributions from $\sigma_{\rm raw}$, several runs were taken with the LHRS in positive polarity mode (i.e., detecting positrons) to measure the positron cross section, σ^{e^+}. The nitrogen electron cross section $\sigma^{e^-}_{\rm N_2}$ was measured by filling the additional reference target cell (Sec. III B) with nitrogen gas and exposing it to the beam. Pair production also occurs when scattering from nitrogen nuclei, so a nitrogen positron cross section, $\sigma^{e^+}_{\rm N_2}$, was also measured with the LHRS in positive polarity mode. The positron cross section on nitrogen $\sigma^{e^+}_{\rm N_2}$ was subtracted from $\sigma^{e^-}_{\rm N_2}$ to avoid double counting the pair-produced events in the measurement that were already accounted for in σ^{e^+}. In principle, one has to consider pion background contributions; however, given the high pion suppression in the LHRS (Sec. II G), this component was found to be negligible. Combining the measurements for $\sigma_{\rm raw}$, σ^{e^+}, $\sigma^{e^-}_{\rm N_2}$, $\sigma^{e^+}_{\rm N_2}$ yielded the experimental ^{3}He cross section, $\sigma_{\rm exp}$,

$$\sigma_{\rm exp} = \sigma_{\rm raw} - \sigma^{e^+} - \sigma^{\rm dil}_{\rm N_2}, \tag{30}$$

$$\sigma^{\rm dil}_{\rm N_2} = \frac{n_{\rm N_2}}{n_{\rm N_2}+n_{^3{\rm He}}}(\sigma^{e^-}_{\rm N_2} - \sigma^{e^+}_{\rm N_2}), \tag{31}$$

where $n_{\rm N_2}$ is the number density of nitrogen in the production cell and $n_{^3{\rm He}}$ is the number density of ^{3}He in the production cell.

When the nitrogen reference cell was in the beam, the number density for the cell was extracted using the measured temperature and pressure of the cell. This number density was used when extracting a nitrogen cross section [Eq. (28)]. A systematic uncertainty of 2.2% was estimated by computing the number densities while varying the temperature and pressure by up to 2° C and 2 psig, respectively [62]. In the ^{3}He production cell, the number density of nitrogen $n_{\rm N_2}$ was taken to be 0.113 amg

[Eq. (31)]. This value was recorded as the target was initially filled, and it is accurate to 3% from a pressure curve analysis.

Because of time constraints and hardware problems encountered during the experiment, there were not enough data to map out the background contributions to the raw cross section for all kinematic bins. To resolve this issue, empirical fits to the positron and nitrogen data (see Appendix C 1) were used to subtract those contributions. Figures 18 and 19 show the raw electron cross section, the positron and nitrogen cross sections (scaled by the ratio of the nitrogen number density to that of ^{3}He in the production target cell), and the background-subtracted electron cross section, $\sigma_{\rm exp}$. The error bars on the data points represent the statistical uncertainties. The largest correction was due to the positrons, at ∼53% in the lowest x bin, and fell to a few percent for $x \gtrsim 0.5$.

3. Radiative corrections

A first correction that must be done *before* carrying out the radiative corrections is to subtract the elastic and quasielastic radiative tails, since they are long and affect all states of higher invariant mass W [114]. For these kinematics, the elastic tail was small and affected the lowest bins in scattered electron energy E' at the $\lesssim$1% level only. The elastic tail was computed following the exact formalism given by Mo and Tsai [114], and using elastic ^{3}He form factors from Amroun [115]. The ^{3}He quasielastic tail, however, was much larger, at ∼25%–30% in the lowest x bin. The quasielastic radiative tail was computed by utilizing an appropriate model of the ^{3}He quasielastic cross section [116] and applying radiative effects [117]. The tail was then subtracted from the data. The model was checked against existing quasielastic ^{3}He data [118–120] covering a broad range of kinematics.

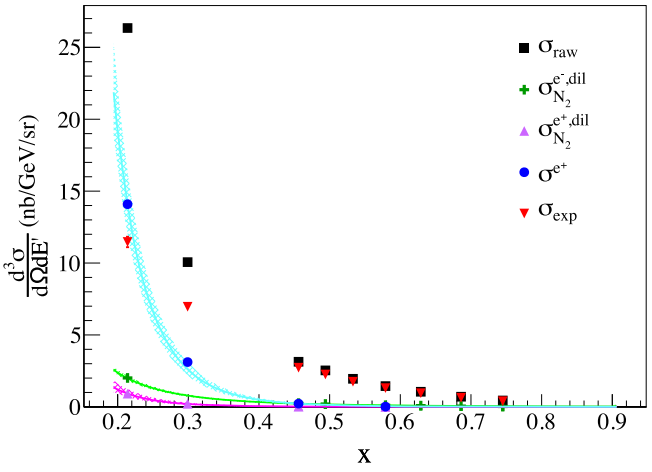

FIG. 18. Cross sections as a function of Bjorken-x at $E = 4.74$ GeV. The squares show the raw electron cross section, and the circles (and fit) show the positron cross section measured on the ^{3}He target. The cross data (and fit) represent the diluted nitrogen cross section measured on the N_2 target, and the up-triangle data (and fit) show the diluted nitrogen cross section measured in positive polarity mode on the N_2 target. The down-triangle data points are the final background-subtracted data, $\sigma_{\rm exp}$. The error bars on the data points represent the statistical uncertainties.

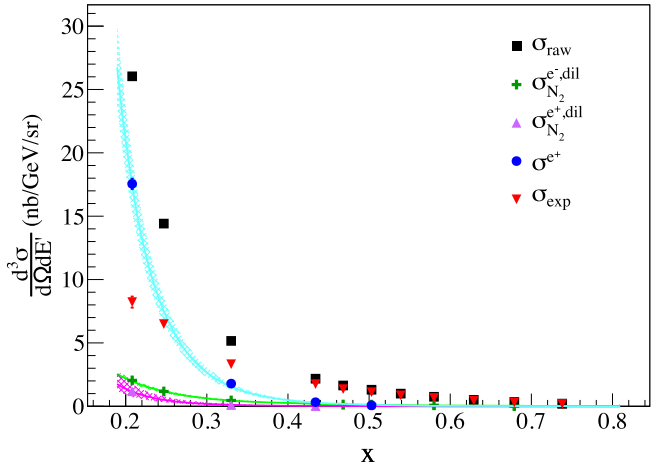

FIG. 19. Cross sections as a function of Bjorken-x at $E = 5.89$ GeV. The description of the various data sets is the same as in Fig. 18.

After the elastic and quasielastic tails had been subtracted from the data, radiative corrections were applied according to Refs. [114,121], where the internal corrections were calculated using the equivalent radiator method and the external corrections were performed using the energy peaking approximation. In the experiment, we took production data for only two beam energies of 4.74 GeV and 5.89 GeV. However, we needed enough data to properly calculate the integrals involved in the radiative correction procedure. Therefore, we used the F1F209 cross section parametrization [122] to fill in the rest of the phase space for each data set. The radiative corrections were as large as ∼50% in the lowest measured x bin, and fell off to a few percent at the large x bins.

The resulting final ^{3}He cross sections for $E = 4.74$ GeV and 5.89 GeV are presented in Fig. 20. The data are tabulated in Tables IV and V. The uncertainty on the final cross section arising from the radiative corrections was determined by varying the contributions to the radiative correction calculations, including the radiation thicknesses in the incident and scattered electron path, and considering different models for the elastic and quasielastic tail calculations. Of these, the quasielastic tail gave the biggest uncertainty, ∼5%–6% for the lowest x bin, falling to ∼1% for all other bins. A full breakdown of the uncertainties on the final results is given in Tables XXIII and XXIV in Appendix E 1.

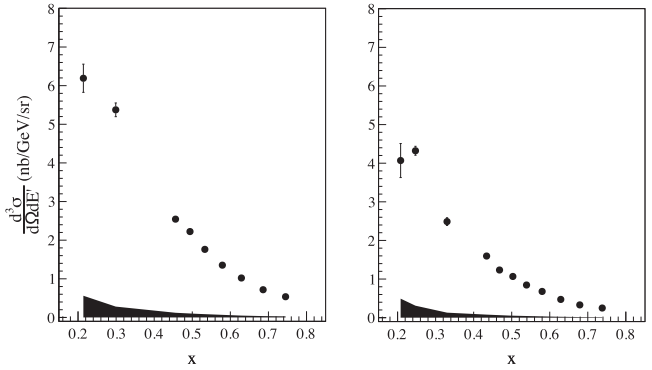

FIG. 20. The final ^{3}He unpolarized cross sections as a function of Bjorken-x. The left (right) panel shows $E = 4.74$ GeV (5.89 GeV) data. The error bars show the statistical uncertainty, while the bands represent the systematic uncertainty.

TABLE V. The final ^{3}He unpolarized cross sections for 5.89 GeV data. The uncertainties listed are statistical and systematic, respectively.

$\langle x \rangle$	$\langle Q^2 \rangle$ [GeV^2]	$\frac{d^3\sigma}{d\Omega dE'}$ [nb/GeV/sr]
0.208	2.064	$4.069 \pm 0.440 \pm 0.492$
0.247	2.409	$4.322 \pm 0.116 \pm 0.310$
0.330	3.095	$2.488 \pm 0.099 \pm 0.130$
0.434	3.882	$1.596 \pm 0.038 \pm 0.079$
0.468	4.124	$1.234 \pm 0.030 \pm 0.063$
0.503	4.360	$1.067 \pm 0.020 \pm 0.052$
0.539	4.603	$0.846 \pm 0.016 \pm 0.042$
0.580	4.873	$0.679 \pm 0.012 \pm 0.033$
0.629	5.173	$0.472 \pm 0.010 \pm 0.022$
0.679	5.478	$0.331 \pm 0.007 \pm 0.016$
0.738	5.811	$0.250 \pm 0.006 \pm 0.013$

C. Asymmetries

1. Extraction of raw asymmetries from data

The raw double-spin asymmetries were extracted from the data recorded in the BigBite detectors according to

$$A_{\parallel}^{\text{raw}} = \frac{N^{\downarrow\Uparrow} - N^{\uparrow\Uparrow}}{N^{\downarrow\Uparrow} + N^{\uparrow\Uparrow}}, \tag{32}$$

$$A_{\perp}^{\text{raw}} = \frac{1}{\langle \cos\phi \rangle} \frac{N^{\downarrow\Rightarrow} - N^{\uparrow\Rightarrow}}{N^{\downarrow\Rightarrow} + N^{\uparrow\Rightarrow}}, \tag{33}$$

where N denotes the number of electron counts after applying data quality and PID cuts for a particular beam and target spin configuration, $\downarrow$ ($\uparrow$) corresponds to the electron's spin polarized antiparallel (parallel) to its momentum, $\Uparrow$ indicates that the target was polarized parallel to the electron momentum, and $\Rightarrow$ indicates that the target was polarized transverse to the electron momentum.

In E06-014, there were three target-spin configurations, either parallel ($\parallel$, referred to here as longitudinal) or transverse ($\perp$, in two orientations: $\Leftarrow$, 90° and $\Rightarrow$, 270°) to the electron beam momentum. The quantity ϕ is the angle between the electron scattering plane (defined by incident and scattered electron momenta $\vec{k}$ and $\vec{k}'$) and the polarization plane (defined by $\vec{k}$ and the target polarization $\vec{S}$). The transverse data were normalized by $\langle \cos\phi \rangle$, since this term is not necessarily equal to unity. This correction was found to be very small. There is no $\langle \phi \rangle$ correction for parallel asymmetry data since the electron spin is aligned along the target spin direction.

TABLE IV. The final ^{3}He unpolarized cross sections for 4.74 GeV data. The uncertainties listed are statistical and systematic, respectively.

$\langle x \rangle$	$\langle Q^2 \rangle$ [GeV^2]	$\frac{d^3\sigma}{d\Omega dE'}$ [nb/GeV/sr]
0.214	1.659	$6.191 \pm 0.365 \pm 0.561$
0.299	2.209	$5.374 \pm 0.178 \pm 0.281$
0.456	3.094	$2.544 \pm 0.048 \pm 0.121$
0.494	3.285	$2.223 \pm 0.034 \pm 0.103$
0.533	3.472	$1.762 \pm 0.026 \pm 0.084$
0.579	3.694	$1.353 \pm 0.027 \pm 0.065$
0.629	3.909	$1.021 \pm 0.018 \pm 0.050$
0.686	4.149	$0.718 \pm 0.012 \pm 0.035$
0.745	4.387	$0.536 \pm 0.012 \pm 0.028$

For the spin asymmetry analysis, one needs to correctly classify the data according to the relation between the digital helicity signal and the physical helicity of the electrons in the beam. Møller polarimetry measurements (Sec. II D 2) were performed after each beam configuration change, to check the consistency of the electron helicity assignment in Hall A [64]. To confirm the relationship between the digital helicity signal and the physical helicity of the electrons in the beam, measurements of the ^{3}He longitudinal quasielastic asymmetry were conducted at $E = 1.23$ GeV and $\theta = 45°$. The sign of the extracted raw quasielastic asymmetry was verified to be consistent with our understanding of the relationship between the digital helicity signal and the physical electron helicity.

Since there were two transverse target spin configurations, care must be taken when combining the results for the 90° and 270° data sets since they will have opposite signs relative to one another. To determine which target configuration should carry which sign, one can consider the dot product of the scattered electron momentum vector $\vec{k}'$ and the target spin vector $\vec{S}$. With the target polarized transverse to the incident electron momentum $\vec{k}$, the target spin only enters the cross section through the dot product of $\vec{k}'$ and $\vec{S}$ [123]. Their dot product is $\vec{k}' \cdot \vec{S} = E' \sin\theta \cos\phi$, where θ is the electron scattering angle. For the transverse spin configurations, ϕ is nearly 0. The positive sense of the

target spin is then the direction that points to the side of the beam line where the scattering electron is detected (consistent with JLab E99-117 [28]). In this experiment, the asymmetry measurement was done using BigBite; therefore, when the target spin was pointing toward BigBite (270°), the asymmetry carried a positive sign. If the target spin was pointing toward the LHRS (90°), it carried a negative sign. Using this convention, the results for 270° and 90° were averaged together using their statistical errors as a weight.

2. Experimental asymmetries

The raw asymmetry definitions shown in Eqs. (32) and (33) do not account for dilution effects due to the presence of nitrogen in the target or the imperfect beam and target polarizations. Therefore, the raw asymmetries must be corrected to yield the experimental asymmetries,

$$A_{\parallel,\perp}^{\mathrm{exp}} = \frac{1}{D_{\mathrm{N}_2} P_b P_t} A_{\parallel,\perp}^{\mathrm{raw}}, \tag{34}$$

where P_b and P_t denote the beam and target polarizations, respectively (Secs. II D 2 and III F) and D_{N_2} the nitrogen dilution factor. Experimental asymmetries for one target-spin configuration were averaged in the same way as shown in Eq. (29), where the ith cross section σ_i is replaced by the ith experimental asymmetry A_i^{exp}.

The nitrogen dilution factor was determined by comparing the rates from the nitrogen reference cell against those from the ^{3}He production cell,

$$D_{\mathrm{N}_2} = 1 - \frac{\Sigma_{\mathrm{N}_2}(\mathrm{N}_2)}{\Sigma_{\mathrm{total}}(^3\mathrm{He})} \frac{t_{\mathrm{ps}}(\mathrm{N}_2)}{t_{\mathrm{ps}}(^3\mathrm{He})} \frac{Q(^3\mathrm{He})}{Q(\mathrm{N}_2)} \frac{t_{LT}(^3\mathrm{He})}{t_{LT}(\mathrm{N}_2)} \frac{n_{\mathrm{N}_2}(^3\mathrm{He})}{n_{\mathrm{N}_2}(\mathrm{N}_2)}, \tag{35}$$

where Σ_{N_2} and Σ_{total} denote the total number of counts that pass data quality and PID cuts detected during the N_2 and ^{3}He production target runs, while $n_{\mathrm{N}_2}(\mathrm{N}_2)$ and $n_{\mathrm{N}_2}(^3\mathrm{He})$ denote the nitrogen number densities present in the two targets. Because the nitrogen and ^{3}He production runs have different characteristics (e.g., scattering rates, running time), the measured electron counts must be normalized by the total charge deposited on the two targets, given by $Q(\mathrm{N}_2)$ and $Q(^3\mathrm{He})$; the trigger prescale factors for the nitrogen and ^{3}He runs, given as $t_{\mathrm{ps}}(\mathrm{N}_2)$ and $t_{\mathrm{ps}}(^3\mathrm{He})$; and finally, the live times for the nitrogen and ^{3}He runs, given as $t_{\mathrm{LT}}(\mathrm{N}_2)$ and $t_{\mathrm{LT}}(^3\mathrm{He})$.

The nitrogen dilution factor was extracted on a run-by-run basis and the results were averaged, weighted by their statistical uncertainties for a given run configuration. The resulting dilution factor was applied bin-by-bin in x and was found to be roughly constant at $D_{\mathrm{N}_2} \approx 0.920 \pm 0.003$ [62].

3. Background corrections

As described in Sec. IV B, the main sources of background contamination were charged pions and pair-produced electrons. To quantify the charged pion contamination in the electron sample, the pion peak in the preshower energy spectrum was fitted with a Gaussian function convoluted with a Landau function, and the electron peak with a Gaussian function, as shown in Fig. 21. The ratio of the pion counts to the electron counts was then evaluated from the integrals of the two fits above a threshold of 200 MeV [62]. This ratio was evaluated for the π^- (N_{π^-}/N_{e^-}) and π^+ (N_{π^+}/N_{e^+}) mesons. The π^+ ratio was evaluated after reversing the polarity of BigBite so that particles with similar trajectories could be compared. The N_{π^-}/N_{e^-} ratio was largest in the lowest x bin of 0.277, at ~2.7%, and dropped quickly to below 1% by $x = 0.425$. The N_{π^+}/N_{e^+} ratio was larger and consistently ~6% across the whole x range. A systematic uncertainty of 2.5% was assigned to the N_π/N_e ratios, the value determined in the immediately preceding experiment, E06-010 [76], in which a similar fitting procedure was used and checked independently through a coincidence trigger between the electrons in BigBite and pions in the LHRS. In E06-010, it was found that these two methods were consistent to around 2%–3% [66].

A spin asymmetry in the charged-pion production will affect the measured electron asymmetries. To study this, asymmetries in the pion sample were determined after applying corrections for the nitrogen dilution and the beam and target polarizations, yielding the π^- and π^+ experimental asymmetries. The results are shown in Figs. 22 and 23 for $E = 5.89$ GeV. After scaling these measured pion asymmetries with the N_π/N_e ratios, it was found that

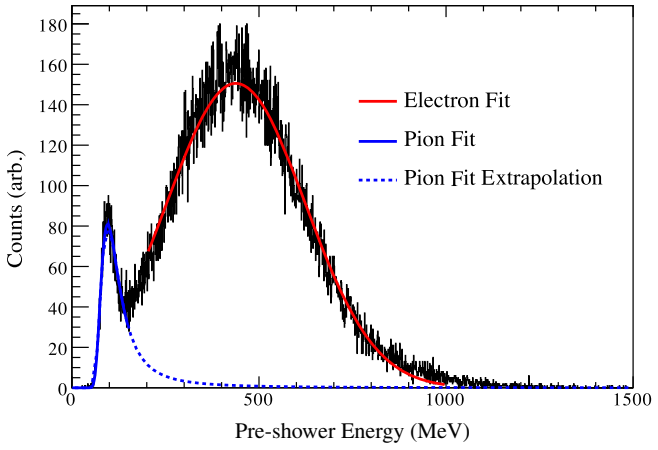

FIG. 21. A signal distribution in the BigBite preshower, where the particle's total deposited energy is plotted for the $\langle x \rangle = 0.425$ bin. Electrons (pions) are shown by the peak on the right (left). The curves fitted to the data are used in the analysis to determine the amount of pion contamination in the electron sample; see the text.

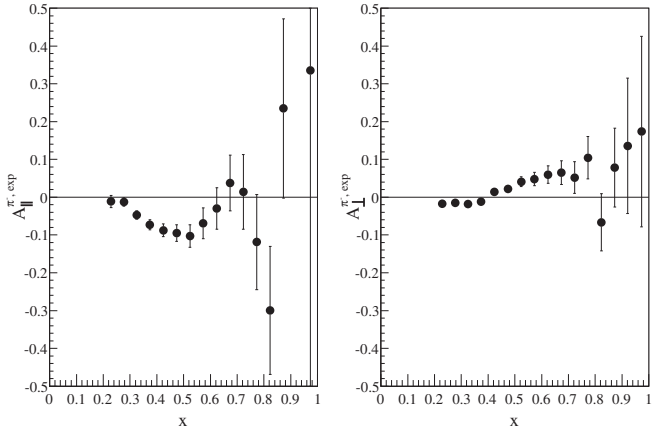

FIG. 22. The π^- experimental asymmetry on ^{3}He for $E = 5.89$ GeV. The left (right) panel shows the data for the target polarized longitudinal (transverse) to the electron beam momentum. The error bars indicate the statistical uncertainty.

the π^- (π^+) asymmetry contribution was less than 5% (3%) of the statistical uncertainty in the asymmetries and therefore could be neglected.

To quantify the contamination due to pair-produced electrons, the ratio of positrons to electrons, N_{e^+}/N_{e^-}, needed to be determined. Because of time constraints this ratio could only be measured directly at 4.74 GeV. To determine this ratio at 5.89 GeV, a parametrization was made of the 4.74 GeV BigBite and LHRS data sets, the 5.89 GeV LHRS data set, and data from JLab CLAS EG1b [124] with $E = 5.7$ GeV and $\theta = 41.1°$. These data, plotted as $(1/E^2)(N_{e^+}/N_{e^-})$, as a function of $k_T = k\sin\theta$, where k_T is the transverse momentum. The data and the fit are shown in Fig. 24. The error on the fit was propagated to be 5%–6% across the x range of the measurements. The lowest x bin, $x = 0.23$, was then excluded from further analysis after the N_{e^+}/N_{e^-} ratio was found to be in excess of 80%.

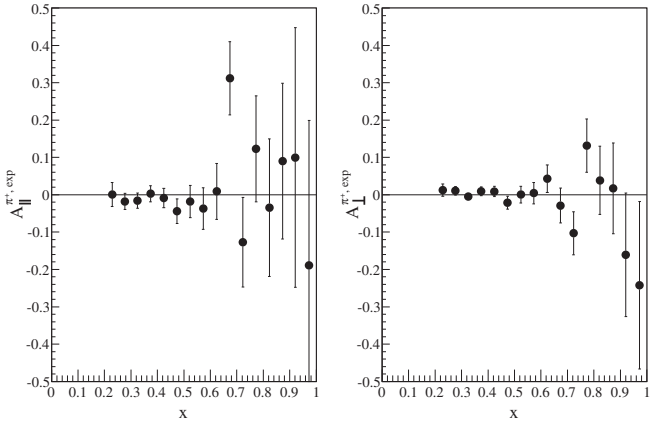

FIG. 23. The π^+ experimental asymmetry on ^{3}He for $E = 5.89$ GeV. The left (right) panel shows the data for the target polarized longitudinal (transverse) to the electron beam momentum. The error bars indicate the statistical uncertainty.

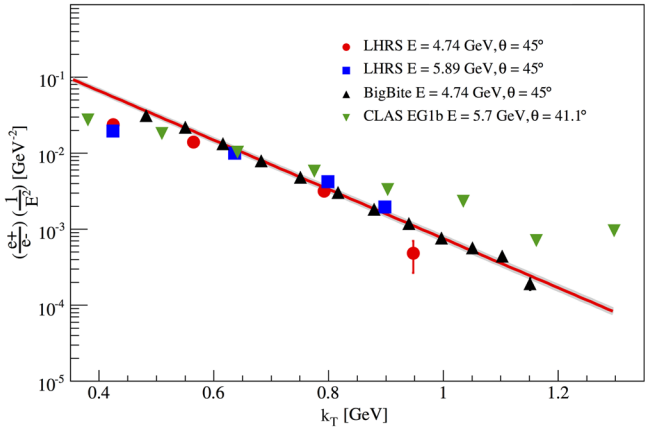

FIG. 24. The N_{e^+}/N_{e^-} data from this experiment measured in the LHRS and BigBite and CLAS EG1b [124] plotted as $(1/E^2)(N_{e^+}/N_{e^-})$ versus the transverse momentum k_T. Our fit function is shown by the solid curve, with its error given by the band surrounding it. See text for additional details.

At the first bin included in the analysis, $x = 0.277$, that ratio was ~50% and fell to less than 10% by $x = 0.473$. Beyond $x = 0.5$ the ratio had dropped to below 3% [62].

Just as with the pion contamination, pair-produced electrons can affect or dilute the measured electron asymmetry. Ideally, the asymmetry should be measured by reversing the polarity of BigBite so that the positrons are detected with the same acceptance as the electrons. However, because of the same time constraints as mentioned previously, this could only be completed for one target-spin orientation (270°) at 4.74 GeV. Because of this, the positron asymmetries were measured bent down in BigBite. The asymmetries measured in this configuration were observed to be in good agreement with those when the positrons were deflected upwards; however, the acceptance, and hence the rate, was ~60% lower. Therefore, for each beam energy and each target-spin configuration a weighted average was computed over all measured asymmetries. The results are shown in Figs. 25 and 26. The measured electron asymmetries for each beam energy and target spin configuration were then corrected by the corresponding weighted average positron asymmetry scaled by the N_{e^+}/N_{e^-} ratio.

The effects of the charged-pion and pair-produced electron asymmetries were corrected for through

$$A_{e^-} = \frac{A_{e^-}^{\mathrm{exp}} - f_1 A_{\pi^-}^{\mathrm{exp}} - f_3 A_{e^+}^{\mathrm{exp}} + f_2 f_3 A_{\pi^+}^{\mathrm{exp}}}{1 - f_1 - f_3 + f_2 f_3}, \quad (36)$$

where $f_1 = N_{\pi^-}/N_{e^-}$; $f_2 = N_{\pi^+}/N_{e^+}$; $f_3 = N_{e^+}/N_{e^-}$; $A_{\pi^\pm}^{\mathrm{exp}}$ are the $\pi^\pm$ experimental asymmetries, and $A_{e^+}^{\mathrm{exp}}$ is the positron experimental asymmetry. Since the corrections for the pion experimental asymmetries were found to be negligible, Eq. (36) can be simplified to

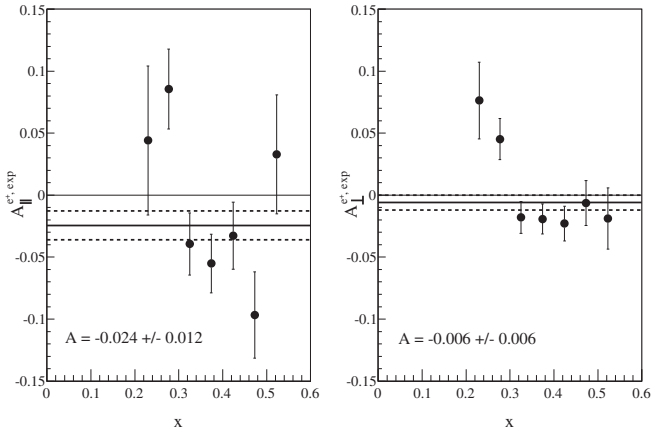

FIG. 25. The positron experimental asymmetry for $E = 4.74$ GeV. The left (right) panel shows the data for the target polarized longitudinal (transverse) to the electron beam momentum. The error bars indicate the statistical uncertainty. The weighted average is indicated by the solid line, and its uncertainty is indicated by the surrounding dashed lines. The numerical value of the weighted average with its uncertainty is also shown.

$$A_{e^-} \approx \frac{A^{\mathrm{exp}}_{e^-} - f_3 A^{\mathrm{exp}}_{e^+}}{1 - f_1 - f_3 + f_2 f_3} \equiv A^{\mathrm{cor}}. \tag{37}$$

At this point, the bins for which $x > 0.90$ were removed from the analysis, so as to exclude the quasielastic and Δ resonance contributions.

4. False asymmetries

When measuring a scattering asymmetry, care must be taken to ensure that the asymmetry was due to electron spin-dependent scattering and not to helicity-correlated changes in the electron beam, known as *false asymmetries*. One potential false asymmetry arises from a difference in the electron beam intensity between the two helicity states, resulting in an asymmetry in the deposited charge on the target. During the experiment, the beam charge asymmetry was limited to ~100 ppm through the use of a feedback loop controlled by a specialized DAQ [125] and was verified by measuring the charge asymmetry using the Compton polarimeter [64]. Compared to the size of the electron asymmetry measurements, A^{cor}, the charge asymmetry was negligible.

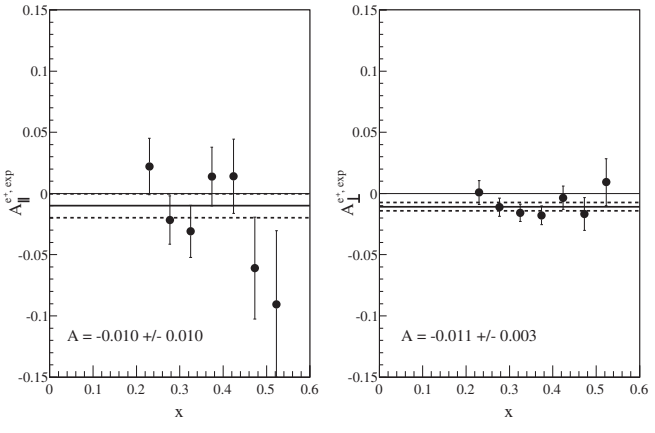

FIG. 26. The positron experimental asymmetry for $E = 5.89$ GeV. The description of the data and fitted line with its uncertainty is the same as Fig. 25.

Helicity-dependent DAQ changes can also generate false asymmetries, which can be observed through the measurement of the detector's live time. A helicity-dependent rate change could lead to one helicity state having a larger live time than the other, resulting in an asymmetry. BigBite detector live times were recorded for each helicity gate for each run of the experiment. The helicity-dependent live-time asymmetry was extracted from the data and was found to be < 100 ppm for the entire data set, which was negligible [62].

In addition to charge- and DAQ-induced false asymmetries, the analysis could also introduce a false asymmetry. For example, if the data rates were high enough, it may be more difficult to reconstruct good tracks related to the higher-rate helicity state as compared to the lower-rate one, resulting in an asymmetry [126]. However, the E06-014 data set was dominated by single-track events (~96%), and thus the rates were not high enough for such an asymmetry to have a significant impact on the measured electron asymmetries.

Potential sources of false asymmetries are limited by the 30 Hz helicity flipping rate of the electron beam. Additionally, any false asymmetry that does not change sign with respect to the IHWP state (Sec. IV C 1), such as those due to electronic cross talk [127], would be canceled when combining data from the two IHWP states. In summary, no significant false asymmetries were observed.

5. Radiative corrections

Radiative corrections on the asymmetries were applied utilizing a similar approach as on the cross sections in Sec. IV B 3. We carried out the corrections on polarized cross section differences, $\Delta\sigma$, related to asymmetries by

$$A^r_{\parallel,\perp} = \frac{\Delta\sigma^r_{\parallel,\perp}}{2\sigma^r_0}, \tag{38}$$

where $A^r_{\parallel}$ ($A^r_{\perp}$) indicates the longitudinal (perpendicular) asymmetry which includes radiative effects. The unpolarized cross section is σ^r_0, where the r indicates that radiative effects have been applied. We used the F1F209 parametrization [122] for the unpolarized cross section. The input used to fill out the integration phase space fell into three different kinematic regions: the DIS region, the quasielastic region, and the Δ resonance region. For the DIS region the de Florian-Sassot-Stratmann-Vogelsang (DSSV) [128] PDF parametrization was used; for the quasielastic region Bosted's nucleon form factors [129], smeared by a quasielastic scaling function [130], was used;

and for the Δ region the MAID model [29] was used. The $\Delta\sigma$ obtained after putting these models together for the three regions described the JLab E94-010 data [131] reasonably well [86].

In the radiative correction procedure, the quasielastic tail was not subtracted first but rather was included in the integration. The elastic tail was found to be negligible and was not subtracted. To minimize statistical fluctuations in the radiative corrections, the corrections were performed on a model of our data set. After obtaining the final $\Delta\sigma$, the corresponding asymmetry was obtained by inverting Eq. (38) (but using the *Born* σ_0 from F1F209) to find A with the size of the radiative correction given by

$$\Delta A = A^b - A^r. \tag{39}$$

The quantity A^b denotes the Born asymmetry and A^r the radiated asymmetry. Here, A^r is the model input to the radiative corrections program. This ΔA was applied to our extracted asymmetries, $A_{\parallel,\perp}^{\mathrm{cor}}$ [see Eq. (37)], as an additive correction. The size of the radiative correction was found to be at most of the order of 45% (10^{-3} absolute) of the uncorrected asymmetry. The radiative corrections in the DIS region were checked against results obtained using the formalism of Akushevich *et al.* [132]. The results of both methods agreed to the 10^{-4} level in the asymmetry.

The asymmetries on ^{3}He before and after radiative corrections for the 4.74 and 5.89 GeV runs are shown in Figs. 27 and 28 and tabulated in Tables VI and VII in Sec. V. The systematic uncertainties for the radiatively-corrected data were obtained by varying all input to reasonable levels. The inputs varied included the electron cuts, the nitrogen dilution factor, beam and target polarizations, pion and pair-production contamination levels, and the radiative corrections. The latter were observed to change less than 5% when using various input models and when the radiation thicknesses before and after scattering were varied by up to ±10%. Tables in Appendix E 2 list the various contributions to the systematic uncertainties.

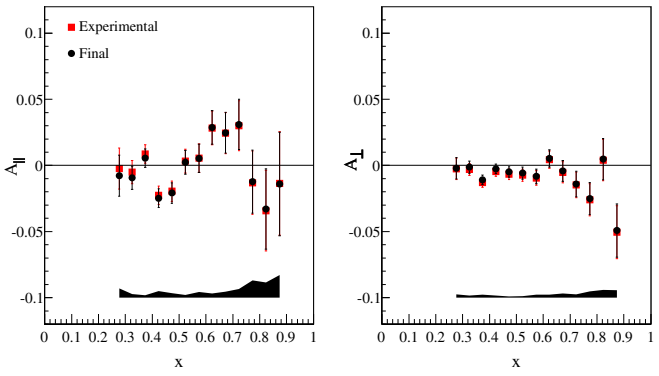

FIG. 27. The parallel and perpendicular asymmetries on ^{3}He for $E = 4.74$ GeV before (square) and after (circle) radiative corrections. The error bands indicate the systematic uncertainty for the final asymmetries.

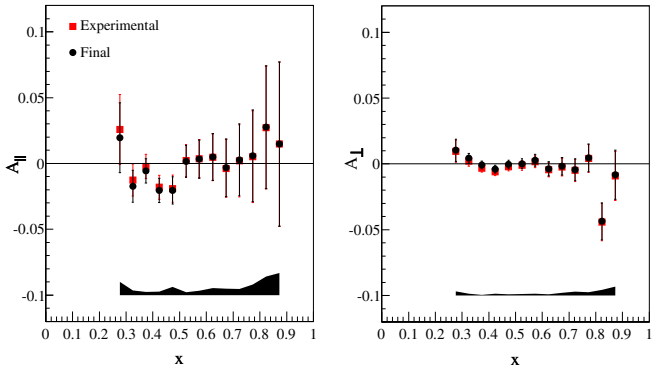

FIG. 28. The parallel and perpendicular asymmetries on ^{3}He for $E = 5.89$ GeV before (square) and after (circle) radiative corrections. The error bands indicate the systematic error for the final asymmetries.

D. From ^{3}He to the neutron

Free nucleons behave differently from those bound in nuclei, primarily due to spin depolarization, Fermi motion, nuclear binding, and nuclear shadowing and antishadowing effects. Additionally, the characteristics of bound nucleons can be altered by the presence of non-nucleonic degrees of freedom and how far off-shell the nucleons are.

We utilized the work of Bissey *et al.* [133], which provides a description of the g_1 spin structure function on ^{3}He over the range $10^{-4} \le x \le 0.8$. It models the ^{3}He wave function incorporating the S, S', and D states, and includes a preexisting Δ (1232) component,

$$g_1^{^3\mathrm{He}}(x) = P_n g_1^n(x) + 2P_p g_1^p(x) - 0.014[g_1^p(x) - 4g_1^n(x)] + a(x)g_1^n(x) + b(x)g_1^p(x), \tag{40}$$

where P_p and P_n are the effective polarizations of the proton and neutron in ^{3}He [60], respectively. The third term arises from the $\Delta(1232)$ component in the ^{3}He wave function [133]. The functions $a(x)$ and $b(x)$ describe nuclear shadowing and antishadowing effects. In the present experiment, the x coverage does not drop below $x \sim 0.2$ so that shadowing and antishadowing effects can be neglected. Therefore, Eq. (40) becomes

$$g_1^{^3\mathrm{He}}(x) \approx P_n g_1^n(x) + 2P_p g_1^p(x) - 0.014[g_1^p(x) - 4g_1^n(x)]. \tag{41}$$

The same formula applies for g_2 data, with g_2 replacing g_1 in Eq. (41).

The nuclear corrections to our data for $d_2^{^3\mathrm{He}}$ were applied to the *integral* (not bin by bin to the d_2 integrand), which

TABLE VI. Asymmetry results for $A_\parallel^{^3\mathrm{He}}$, $A_\perp^{^3\mathrm{He}}$, $A_1^{^3\mathrm{He}}$, and $g_1^{^3\mathrm{He}}/F_1^{^3\mathrm{He}}$ for the 4.74 GeV data. The first uncertainty is statistical, while the second is systematic.

$\langle x\rangle$	$\langle Q^2\rangle$ [GeV^2]	$A_\parallel^{^3\mathrm{He}}$	$A_\perp^{^3\mathrm{He}}$	$A_1^{^3\mathrm{He}}$	$g_1^{^3\mathrm{He}}/F_1^{^3\mathrm{He}}$
0.277	2.038	$-0.008 \pm 0.015 \pm 0.007$	$-0.002 \pm 0.008 \pm 0.003$	$-0.008 \pm 0.017 \pm 0.004$	$-0.009 \pm 0.016 \pm 0.004$
0.325	2.347	$-0.009 \pm 0.009 \pm 0.003$	$-0.001 \pm 0.005 \pm 0.002$	$-0.010 \pm 0.010 \pm 0.001$	$-0.010 \pm 0.009 \pm 0.001$
0.374	2.639	$0.005 \pm 0.007 \pm 0.002$	$-0.011 \pm 0.004 \pm 0.002$	$0.008 \pm 0.008 \pm 0.001$	$0.001 \pm 0.007 \pm 0.001$
0.424	2.915	$-0.025 \pm 0.007 \pm 0.005$	$-0.003 \pm 0.004 \pm 0.002$	$-0.027 \pm 0.008 \pm 0.003$	$-0.026 \pm 0.007 \pm 0.002$
0.473	3.176	$-0.021 \pm 0.008 \pm 0.003$	$-0.005 \pm 0.004 \pm 0.001$	$-0.022 \pm 0.009 \pm 0.002$	$-0.023 \pm 0.008 \pm 0.002$
0.523	3.425	$0.002 \pm 0.009 \pm 0.002$	$-0.006 \pm 0.005 \pm 0.001$	$0.004 \pm 0.010 \pm 0.001$	$0.000 \pm 0.009 \pm 0.001$
0.574	3.662	$0.005 \pm 0.010 \pm 0.004$	$-0.008 \pm 0.005 \pm 0.002$	$0.008 \pm 0.012 \pm 0.002$	$0.002 \pm 0.011 \pm 0.002$
0.623	3.886	$0.029 \pm 0.013 \pm 0.003$	$0.005 \pm 0.007 \pm 0.002$	$0.031 \pm 0.015 \pm 0.002$	$0.031 \pm 0.013 \pm 0.002$
0.673	4.099	$0.025 \pm 0.015 \pm 0.005$	$-0.004 \pm 0.009 \pm 0.003$	$0.030 \pm 0.018 \pm 0.003$	$0.023 \pm 0.016 \pm 0.002$
0.723	4.307	$0.031 \pm 0.019 \pm 0.007$	$-0.014 \pm 0.009 \pm 0.002$	$0.041 \pm 0.022 \pm 0.004$	$0.026 \pm 0.020 \pm 0.003$
0.773	4.504	$-0.012 \pm 0.024 \pm 0.013$	$-0.025 \pm 0.012 \pm 0.005$	$-0.005 \pm 0.028 \pm 0.008$	$-0.023 \pm 0.025 \pm 0.007$
0.823	4.694	$-0.033 \pm 0.030 \pm 0.012$	$0.005 \pm 0.016 \pm 0.006$	$-0.041 \pm 0.037 \pm 0.007$	$-0.032 \pm 0.032 \pm 0.006$
0.874	4.876	$-0.014 \pm 0.039 \pm 0.017$	$-0.049 \pm 0.020 \pm 0.006$	$0.004 \pm 0.048 \pm 0.010$	$-0.035 \pm 0.041 \pm 0.009$

resulted in two average Q^2 bins for each of the beam energies 4.74 and 5.89 GeV. Thus, the correction followed the formalism defined in Eq. (41),

$$d_2^n = \frac{1}{\tilde{P}_n}(d_2^{^3\mathrm{He}} - \tilde{P}_p d_2^p), \tag{42}$$

for a given bin in Q^2, where the quantity $\tilde{P}_p = 2P_p - 0.014$ and $\tilde{P}_n = P_n + 0.056$. For the proton an effective polarization $P_p = -0.028^{+0.009}_{-0.004}$ was used, and for the neutron $P_n = 0.86^{+0.036}_{-0.020}$ [28]. The matrix element d_2^p was evaluated by considering various global analyses [49,128,134–136] to construct g_1^p. The Wandzura-Wilczek relation [14,137,138] was used to obtain g_2^p, which is valid if the higher-twist effects are assumed to be small; this is a reasonable assumption based on the results of SLAC E155 [139]. Using the average of the results for g_1^p and g_2^p, the d_2^p integral was evaluated over the same x range of our experiment at $\langle Q^2\rangle = 3.21$ and 4.32 GeV^2, and the result was inserted into Eq. (42).

To obtain the nuclear corrections needed to extract g_1^n/F_1^n, we first divided Eq. (41) by $F_1^{^3\mathrm{He}}$ and then rewrote $F_1^{^3\mathrm{He}}$ in terms of $F_2^{^3\mathrm{He}}$ following

$$F_1(x,Q^2) = \frac{F_2(x,Q^2)(1+\gamma^2)}{2x[1+R(x,Q^2)]}, \tag{43}$$

where R is taken to be target independent [133], which is a reasonable assumption for $Q^2 > 1.5$ GeV^2 and $x > 0.15$ [140]. Solving for g_1^n/F_1^n yielded

$$\frac{g_1^n}{F_1^n} = \frac{1}{\tilde{P}_n}\frac{F_2^{^3\mathrm{He}}}{F_2^n}\left(\frac{g_1^{^3\mathrm{He}}}{F_1^{^3\mathrm{He}}} - \tilde{P}_p\frac{F_2^p}{F_2^{^3\mathrm{He}}}\frac{g_1^p}{F_1^p}\right). \tag{44}$$

Using Eq. (44), we extracted g_1^n/F_1^n from our ^{3}He data. For the unpolarized $F_2^{^3\mathrm{He}}$ structure function, we utilized the

TABLE VII. Asymmetry results for $A_\parallel^{^3\mathrm{He}}$, $A_\perp^{^3\mathrm{He}}$, $A_1^{^3\mathrm{He}}$, and $g_1^{^3\mathrm{He}}/F_1^{^3\mathrm{He}}$ for the 5.89 GeV data. The first uncertainty is statistical, while the second is systematic.

$\langle x\rangle$	$\langle Q^2\rangle$ [GeV^2]	$A_\parallel^{^3\mathrm{He}}$	$A_\perp^{^3\mathrm{He}}$	$A_1^{^3\mathrm{He}}$	$g_1^{^3\mathrm{He}}/F_1^{^3\mathrm{He}}$
0.277	2.626	$0.019 \pm 0.027 \pm 0.010$	$0.010 \pm 0.008 \pm 0.003$	$0.020 \pm 0.029 \pm 0.006$	$0.024 \pm 0.028 \pm 0.006$
0.325	3.032	$-0.017 \pm 0.012 \pm 0.003$	$0.004 \pm 0.004 \pm 0.001$	$-0.019 \pm 0.013 \pm 0.002$	$-0.016 \pm 0.012 \pm 0.002$
0.374	3.421	$-0.006 \pm 0.009 \pm 0.002$	$-0.001 \pm 0.003 \pm 0.001$	$-0.006 \pm 0.010 \pm 0.001$	$-0.006 \pm 0.009 \pm 0.001$
0.424	3.802	$-0.020 \pm 0.009 \pm 0.003$	$-0.004 \pm 0.003 \pm 0.001$	$-0.021 \pm 0.010 \pm 0.002$	$-0.022 \pm 0.009 \pm 0.002$
0.474	4.169	$-0.021 \pm 0.010 \pm 0.006$	$0.000 \pm 0.003 \pm 0.001$	$-0.022 \pm 0.011 \pm 0.003$	$-0.021 \pm 0.010 \pm 0.003$
0.524	4.514	$0.002 \pm 0.012 \pm 0.002$	$0.000 \pm 0.004 \pm 0.001$	$0.002 \pm 0.013 \pm 0.001$	$0.002 \pm 0.012 \pm 0.001$
0.573	4.848	$0.003 \pm 0.015 \pm 0.003$	$0.003 \pm 0.004 \pm 0.001$	$0.003 \pm 0.016 \pm 0.002$	$0.004 \pm 0.015 \pm 0.002$
0.624	5.176	$0.005 \pm 0.018 \pm 0.005$	$-0.004 \pm 0.005 \pm 0.001$	$0.006 \pm 0.020 \pm 0.003$	$0.003 \pm 0.018 \pm 0.003$
0.674	5.486	$-0.003 \pm 0.022 \pm 0.005$	$-0.002 \pm 0.007 \pm 0.002$	$-0.003 \pm 0.024 \pm 0.003$	$-0.004 \pm 0.022 \pm 0.002$
0.723	5.777	$0.003 \pm 0.027 \pm 0.005$	$-0.004 \pm 0.008 \pm 0.003$	$0.004 \pm 0.031 \pm 0.003$	$0.001 \pm 0.028 \pm 0.003$
0.773	6.059	$0.006 \pm 0.035 \pm 0.008$	$0.005 \pm 0.010 \pm 0.002$	$0.005 \pm 0.039 \pm 0.004$	$0.008 \pm 0.035 \pm 0.004$
0.823	6.325	$0.028 \pm 0.047 \pm 0.014$	$-0.044 \pm 0.014 \pm 0.004$	$0.045 \pm 0.053 \pm 0.008$	$0.009 \pm 0.047 \pm 0.013$
0.873	6.585	$0.015 \pm 0.062 \pm 0.017$	$-0.008 \pm 0.019 \pm 0.007$	$0.020 \pm 0.072 \pm 0.009$	$0.011 \pm 0.064 \pm 0.009$

F1F209 parametrization [122], which incorporates Fermi motion and EMC effects [141,142], and for F_2^p and F_2^n, the unpolarized PDF model CJ12 [143] was used. A fit to world g_1^p/F_1^p data [45,47,56,139,144] was performed and used. The fit used a second-order polynomial in x with three free parameters and assumed Q^2 independence. Any Q^2 dependence would cancel in the ratio of g_1/F_1 to leading order and next-to-leading order [123]. For more details, see Appendix C 2.

For the nuclear corrections to obtain A_1^n, we used the expression for A_1 in terms of the structure functions g_1, g_2, and F_1 (Appendix A 4). Solving for A_1^n gave [cf. Eq. (44)]

$$A_1^n = \frac{1}{\tilde{P}_n}\frac{F_2^{^3\mathrm{He}}}{F_2^n}\left(A_1^{^3\mathrm{He}} - \tilde{P}_p\frac{F_2^p}{F_2^{^3\mathrm{He}}}A_1^p\right). \quad (45)$$

The same models used in the g_1/F_1 analysis for F_2 on ^{3}He, the proton, and the neutron were used in the A_1 analysis. Similar to the g_1/F_1 analysis, a Q^2-independent, second-order polynomial in x was fit to world A_1^p data [47,56,139,145–149] and used in the analysis. For more details, see Appendix C 3.

Other neutron extraction methods have been studied in Ref. [150], where the full convolution formalism was used at finite Q^2, including the nucleon off-shell and Δ contributions. Such calculations are consistent with our extraction of d_2^n and A_1^n following Eqs. (42) and (45), respectively.

V. RESULTS

A. ^{3}He results

Results for the unpolarized e-^{3}He scattering cross section (Sec. IV B) for $E = 4.74$ and 5.89 GeV are given in Tables IV and V. All of the contributions to the systematic uncertainty in the cross section are given in Tables XXIII and XXIV. The biggest contribution to the systematic uncertainty was the background subtraction, at a relative uncertainty of ∼9% in the lowest bin in x. Our extracted cross section values are in good agreement with the F1F209 parametrization [122].

The $\vec{e} - \vec{^3\mathrm{He}}$ electron asymmetries $A_\parallel^{^3\mathrm{He}}$ and $A_\perp^{^3\mathrm{He}}$ (Sec. IV C), the virtual photon asymmetry $A_1^{^3\mathrm{He}}$, and the structure function ratio $g_1^{^3\mathrm{He}}/F_1^{^3\mathrm{He}}$ [Eqs. (18) and (19)] for

TABLE VIII. The g_1 and g_2 spin-structure functions measured on ^{3}He at an incident electron energy of 4.74 GeV. The first uncertainty is statistical, while the second is systematic.

$\langle x\rangle$	$g_1^{^3\mathrm{He}}$	$g_2^{^3\mathrm{He}}$
0.277	$-0.009 \pm 0.016 \pm 0.009$	$-0.006 \pm 0.034 \pm 0.009$
0.325	$-0.009 \pm 0.008 \pm 0.002$	$-0.001 \pm 0.014 \pm 0.006$
0.374	$0.001 \pm 0.005 \pm 0.002$	$-0.026 \pm 0.009 \pm 0.005$
0.424	$-0.014 \pm 0.004 \pm 0.003$	$0.001 \pm 0.006 \pm 0.002$
0.473	$-0.010 \pm 0.003 \pm 0.002$	$-0.002 \pm 0.004 \pm 0.001$
0.523	$0.000 \pm 0.003 \pm 0.000$	$-0.005 \pm 0.004 \pm 0.001$
0.574	$0.000 \pm 0.003 \pm 0.001$	$-0.005 \pm 0.003 \pm 0.001$
0.623	$0.005 \pm 0.002 \pm 0.001$	$0.000 \pm 0.002 \pm 0.001$
0.673	$0.003 \pm 0.002 \pm 0.001$	$-0.002 \pm 0.002 \pm 0.001$
0.723	$0.002 \pm 0.002 \pm 0.001$	$-0.003 \pm 0.002 \pm 0.001$
0.773	$-0.001 \pm 0.002 \pm 0.001$	$-0.002 \pm 0.001 \pm 0.001$
0.823	$-0.001 \pm 0.001 \pm 0.001$	$0.001 \pm 0.001 \pm 0.000$
0.874	$-0.001 \pm 0.001 \pm 0.001$	$-0.002 \pm 0.001 \pm 0.001$

TABLE IX. The g_1 and g_2 spin-structure functions measured on ^{3}He at an incident electron energy of 5.89 GeV. The first uncertainty is statistical, while the second is systematic.

$\langle x\rangle$	$g_1^{^3\mathrm{He}}$	$g_2^{^3\mathrm{He}}$
0.277	$0.026 \pm 0.029 \pm 0.012$	$0.046 \pm 0.047 \pm 0.019$
0.325	$-0.013 \pm 0.010 \pm 0.003$	$0.022 \pm 0.015 \pm 0.006$
0.374	$-0.004 \pm 0.006 \pm 0.002$	$0.000 \pm 0.008 \pm 0.002$
0.424	$-0.011 \pm 0.005 \pm 0.002$	$-0.002 \pm 0.006 \pm 0.002$
0.474	$-0.008 \pm 0.004 \pm 0.002$	$0.003 \pm 0.004 \pm 0.002$
0.524	$0.000 \pm 0.003 \pm 0.001$	$0.000 \pm 0.003 \pm 0.001$
0.573	$0.001 \pm 0.003 \pm 0.001$	$0.001 \pm 0.003 \pm 0.001$
0.624	$0.000 \pm 0.002 \pm 0.001$	$-0.002 \pm 0.002 \pm 0.000$
0.674	$0.000 \pm 0.002 \pm 0.000$	$0.000 \pm 0.002 \pm 0.000$
0.723	$0.000 \pm 0.002 \pm 0.000$	$-0.001 \pm 0.002 \pm 0.000$
0.773	$0.000 \pm 0.002 \pm 0.000$	$0.000 \pm 0.001 \pm 0.000$
0.823	$0.000 \pm 0.002 \pm 0.000$	$-0.003 \pm 0.001 \pm 0.001$
0.873	$0.000 \pm 0.002 \pm 0.000$	$0.000 \pm 0.001 \pm 0.000$

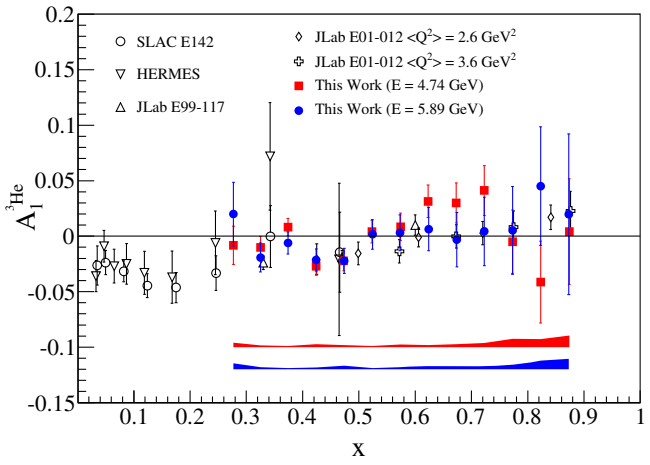

FIG. 29. Our measured result for $A_1^{^3\mathrm{He}}$ for 4.74 GeV (filled squares) and 5.89 GeV (filled circles) data. The error bars on our data points represent the statistical uncertainty. The bands at the bottom of the plot indicate the systematic uncertainty for each data set, where the upper (lower) band corresponds to the 4.74 GeV (5.89 GeV) data set. The DIS data set corresponds to data for which $x < 0.519$ ($x < 0.623$) for $E = 4.74$ GeV (5.89 GeV); the data at larger x values correspond to the resonance region. Also plotted are world DIS data from SLAC E142 [43], HERMES [151], and JLab E99-117 [28,46], and resonance data from JLab E01-012 [152].

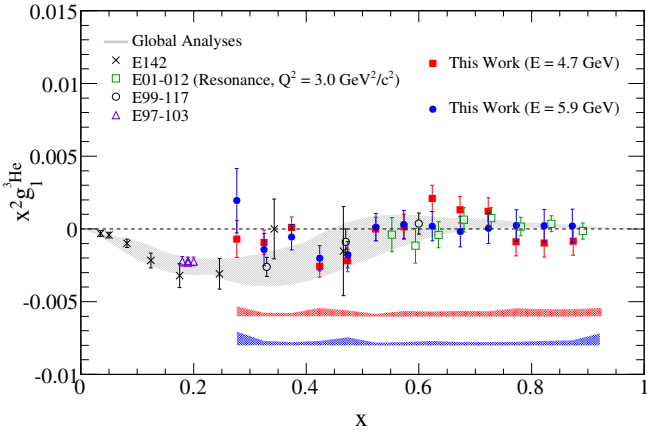

FIG. 30. Our results for g_1 on ^{3}He for 4.74 GeV (filled squares) and 5.89 GeV (filled circles) data. The error bars on our data points represent the statistical uncertainty. The bands at the bottom of the plot indicate the systematic uncertainty for each data set, where the upper (lower) band corresponds to the 4.74 GeV (5.89 GeV) data set. The DIS data set corresponds to data for which $x < 0.519$ ($x < 0.623$) for $E = 4.74$ GeV (5.89 GeV); the data at larger x values correspond to the resonance data. Our data are compared to world DIS data from JLab E99-117 [28,46], SLAC E142 [43], and resonance data from JLab E01-012 [152] and JLab E97-103 [153,154]. The gray band represents an envelope of various global analyses [59,128,134–136] for g_1 at $Q^2 = 4.43$ GeV^2, which was the average Q^2 of our data set.

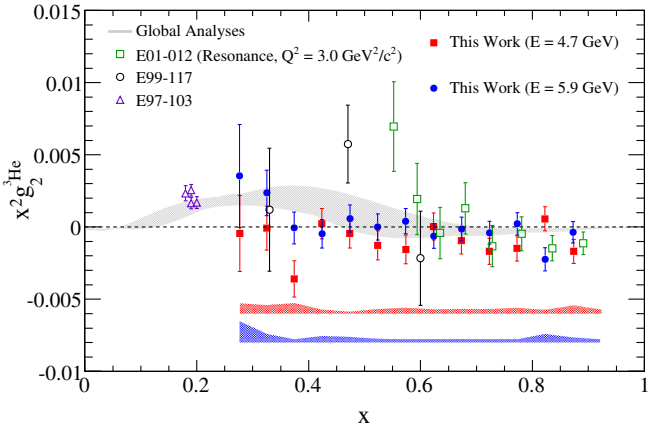

FIG. 31. Our results for g_2 on ^{3}He for the 4.74 GeV (filled squares) and 5.89 GeV (filled circles) data. The error bars on our data points represent the statistical uncertainty. The bands at the bottom of the plot indicate the systematic uncertainty for each data set, where the upper (lower) band corresponds to the 4.74 GeV (5.89 GeV) data set. The DIS data set corresponds to data for which $x < 0.519$ ($x < 0.623$) for $E = 4.74$ GeV (5.89 GeV); the data at larger x values correspond to the resonance data. Our data are compared to world data from JLab E99-117 [28,46], JLab E01-012 [152] (resonance data), and JLab E97-103 [153,154] (resonance data). The gray band represents an envelope of various global analyses [59,128,134–136] used to construct g_2^{WW}.

TABLE X. The d_2^n results with statistical and systematic uncertainties. The last uncertainty represents that due to neglecting the Q^2 evolution of the d_2^n integrand.

$\langle Q^2 \rangle$ [GeV^2]	d_2^n [$\times 10^{-5}$]
3.21	$-421.0 \pm 79.0 \pm 82.0 \pm 8.0$
4.32	$-35.0 \pm 83.0 \pm 69.0 \pm 7.0$

the 4.74 GeV and 5.89 GeV data are given in Tables VI and VII. The polarized structure functions $g_1^{^3\mathrm{He}}$ and $g_2^{^3\mathrm{He}}$ [Eqs. (B3) and (B4)] are given in Tables VIII and IX. All of the contributions to the systematic uncertainties are given in Appendix E, with the dominant one being the selection of the electron sample.

The asymmetry $A_1^{^3\mathrm{He}}$ is plotted in Fig. 29, compared to the world DIS data from SLAC E142 [43], HERMES [151], and JLab E99-117 [28,46]. Also plotted are resonance data from JLab E01-012 [152]. We find that our results reproduce the trend of existing data.

The spin-structure functions $g_1^{^3\mathrm{He}}$ and $g_2^{^3\mathrm{He}}$ are presented in Figs. 30 and 31, in which the world DIS data from JLab E99-117 [28,46] and SLAC E142 [43] are also shown. Resonance data from JLab E01-012 [152] and E97-103 [153,154] are also presented. The gray band represents an envelope encompassing a number of global analyses [59,128,134–136]. Our data reproduce the trend seen in existing $g_1^{^3\mathrm{He}}$ data. For $g_2^{^3\mathrm{He}}$, our data have improved on the uncertainty by about a factor of 2 relative to the JLab E99-117 data set.

B. Neutron results

1. The matrix element d_2^n

Results for the d_2^n matrix element [Eq. (17) and Sec. IV D], first published in Ref. [155], are shown in Fig. 32 and tabulated in Table X. The matrix element was extracted using the Cornwall-Norton (CN) moments [156]. Since our measurement did not cover the full x range, a low-x ($x < 0.25$) and a high-x ($x > 0.90$) contribution needed to be evaluated from other sources. For the low-x region, a third-order polynomial fit to the world data on $x^2 g_1^n$ [43,44,47,154] and $x^2 g_2^n$ [27,139,154] was used to evaluate d_2^n. This contribution is relatively small, considering the x^2 weighting. The large-x contribution comes from the elastic peak, which was modeled using the Riordan [35] and Kelly [36] parametrizations. The contribution from the range $0.90 < x < 0.99$ was considered to be negligible when taking into account the size of our g_1 and g_2 data at $x \sim 0.90$. Nuclear corrections were applied to our ^{3}He data as described in Sec. IV D. Adding the low-x and high-x (elastic) contributions to our measured result gave the full d_2^n integral. Target mass corrections were checked by extracting

d_2^n using the Nachtmann moments [157]; the difference between the CN and Nachtmann approaches was found to be small relative to the statistical uncertainties. An overview of the systematic uncertainties is given in Table XXXIII in Appendix E. The largest contribution to the systematic uncertainty comes from the unmeasured low-x region.

Our unpolarized cross section and double-spin asymmetry data were obtained at various Q^2 values; since the d_2^n integral is typically carried out at constant Q^2, we considered what the effect of evolving $\bar{g}_2^n$ (the twist-3 part of g_2^n) would have on the d_2^n value. To do this, we utilized the $\bar{g}_2^n$ model from Ref. [158] along with the Q^2 evolution description for g_2^n from Ref. [159], which uses flavor-nonsinglet evolution equations and utilizes large-N_c and large-x ($x \gtrsim 0.1$) approximations. The Q^2-evolution calculations were performed using QCDNUM [160] in the variable-flavor number scheme (VFNS) and with $\alpha_s(Q^2 = M_Z^2) = 0.1185$ [161]. For each of our measured x bins at a given beam energy, the model was evolved from its initial value at $Q^2 = 1$ GeV^2 to the measured Q^2 value (Q_m^2) for that particular x bin and also to the $\langle Q^2 \rangle$ value for the given beam energy; see Figs. 33 and 34. We then evaluated

$$\Delta d_2^n = |d_2^n(\langle Q^2 \rangle) - d_2^n(Q_m^2)|, \tag{46}$$

where $\langle Q^2 \rangle = 3.21$ GeV^2 (4.32 GeV^2) for $E = 4.74$ GeV (5.89 GeV). The d_2^n integral was evaluated according to Eq. (4) for our measured $\langle x \rangle$ bins corresponding to $0.277 \leq x \leq 0.874$ ($0.277 \leq x \leq 0.873$) for $E = 4.74$ GeV (5.89 GeV). We found $\Delta d_2^n = 0.00008$ (0.00007) for $E = 4.74$ GeV (5.89 GeV), which is a factor of 6

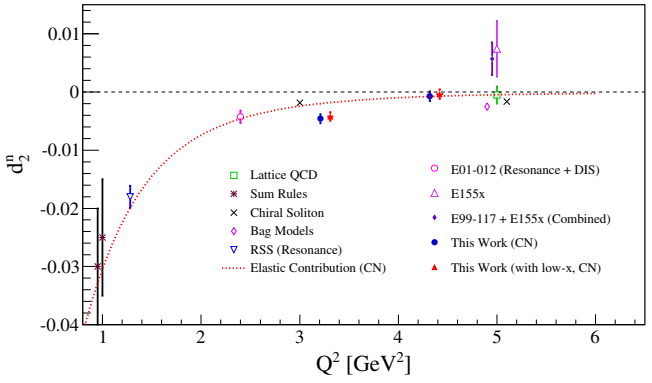

FIG. 32. Our measured d_2^n data as a function of Q^2 compared to the world data from SLAC E155x [27], JLab E99-117, and SLAC E155x [28], JLab RSS [25], and JLab E01-012 [26]. Our results including the low-x contribution are offset in Q^2 for clarity. Also shown are various theoretical calculations, including a QCD sum rule approach [30,31], a chiral soliton model [32], and a bag model [33]. Additionally, a lattice QCD [34] calculation is shown. The elastic contribution to d_2^n is given by the dashed curve, evaluated using the CN moments. Figure reproduced from Ref. [155].

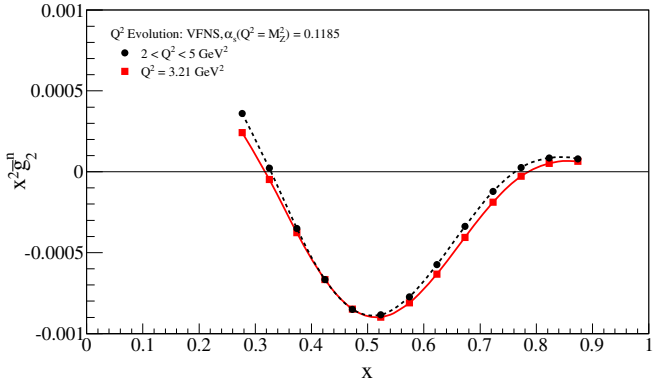

FIG. 33. The d_2^n integrand for 4.74 GeV kinematics. For each measured $\langle x \rangle$ bin, the model [158] was evolved [159,160] to the measured (average) Q^2 value indicated by the circles (squares). For more details, see the text.

(5) smaller than the systematic uncertainty on our measured d_2^n for $E = 4.74$ GeV (5.89 GeV). The difference between the constant Q^2 evaluation of d_2^n compared to the varying Q^2 approach was taken as an estimate of the systematic uncertainty due to not performing the Q^2 evolution on our data.

Our result at $\langle Q^2 \rangle = 3.21$ GeV^2 is small and negative, while the result at $\langle Q^2 \rangle = 4.32$ GeV^2 is consistent with zero (Table X). The trend of our measurements appears to be in agreement with the lattice QCD calculation [34] at $Q^2 = 5$ GeV^2. Our d_2^n extraction is also consistent with bag [33,38,39] and chiral soliton [32] models, as shown in Fig. 32.

The Jefferson Lab Angular Momentum (JAM) Collaboration has published new results from their global QCD analysis [162]. Their work utilizes an iterative Monte Carlo technique that aims to reduce the influence of unphysical fitting parameters and lower the impact of parameter initial values on the results. JAM has included our data in their global analysis by fitting directly our DIS

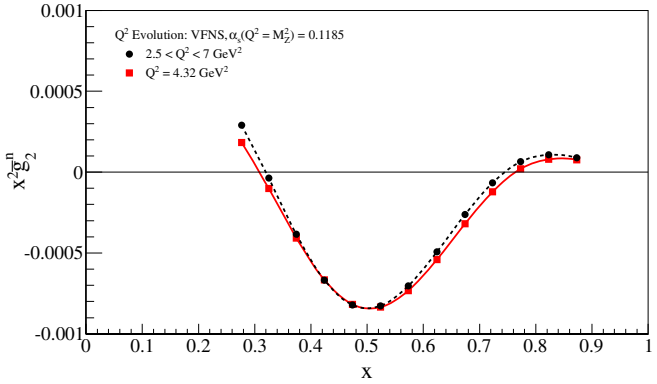

FIG. 34. The d_2^n integrand for 5.89 GeV kinematics. For each measured $\langle x \rangle$ bin, the model [158] was evolved [159,160] to the measured (average) Q^2 value indicated by the circles (squares). For more details, see the text.

data for $A_{\parallel}^{^3\mathrm{He}}$ and $A_{\perp}^{^3\mathrm{He}}$. Extracting a pure twist-3 d_2^n without higher-twist contributions from resonances at the same Q^2 values as our results, they find a sizable effect on their (extrapolated) prediction at $Q^2 = 1$ GeV^2, reducing it from 0.005 ± 0.005 to -0.001 ± 0.001. They also found their d_2^n value to be consistent with lattice calculations [34] when extrapolating to $Q^2 = 5$ GeV^2.

2. The matrix element a_2^n

Following a similar procedure to that discussed for d_2, we can extract the a_2 matrix element from our g_1 data according to the third CN moment of g_1,

$$a_2(Q^2) = \int_0^1 x^2 g_1(x, Q^2) dx. \tag{47}$$

The low-x, high-x, and measured regions were treated in the same way as was done for the d_2 analysis, using the same model inputs. Our g_1 data were not evolved to a constant Q^2, as our investigation into the Q^2 evolution of our g_1 data revealed that the Q^2 dependence was negligible [62]. Our results for a_2^n are shown in Fig. 35, where the inner error bars are the statistical uncertainties and the outer error bars represent the in-quadrature sum of statistical and systematic uncertainties. The circle (square) data points exclude (include) the unmeasured low-x region. Both data points extracted are positive, and the elastic contribution is sizable. The SLAC E143 [47] data are also plotted, where their uncertainty is the in-quadrature sum of the statistical and systematic contributions. The up-triangles represent the average over global analyses [59,128,134–136]. The lattice calculation shown is from Göckeler *et al.* [34], where the error bar is statistical with a 15% systematic uncertainty added in quadrature. The systematic uncertainty arises from their extrapolation of their result to the chiral limit [34]. Our results are tabulated in Table XI, broken down into the low-x, measured, and high-x regions. The last column shows the full extraction. The systematic uncertainties on a_2^n are dominated by that in $a_2^{^3\mathrm{He}}$ and that due to the parametrization of a_2^p. The uncertainties for a_2^n are summarized in Appendix E 5.

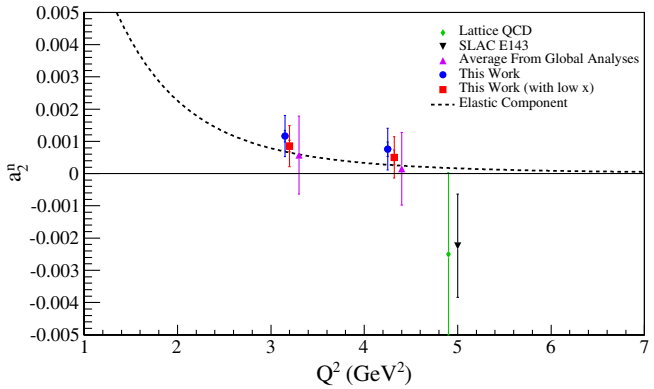

FIG. 35. Our measured a_2^n data compared to SLAC E143 [47] and a lattice QCD calculation [34], both of which are at $Q^2 = 5$ GeV^2. The lattice calculation is offset in Q^2 for clarity. The up-triangles represent the average over global analyses [59,128,134–136], which are offset in Q^2 for clarity. Our measurements shown as the circles (squares) exclude (include) the unmeasured low-x region. The inner error bar on our data is the statistical error, and the outer error bar is the in-quadrature sum of the statistical and systematic uncertainties. The results excluding the low-x contribution are offset in Q^2 for clarity. The elastic contribution is computed by using the Riordan [35] and Kelly [36] parametrizations for G_E^n and G_M^n, respectively.

3. Color force extraction

In order to decompose the Lorentz color force into its electric and magnetic components, one needs to first extract the twist-4 matrix element, f_2^n. This is accomplished by considering our measured d_2^n value along with the a_2^n matrix element.

The a_2^n matrix element was evaluated for various global analyses [59,128,134–136] over the range $0.02 < x < 0.90$, and the average of the results at each $\langle Q^2 \rangle$ bin is taken as the value of a_2^n. These results are consistent with our extracted values (Fig. 35). The elastic contribution was added to the integral in a similar fashion as was done for d_2^n.

With d_2^n and a_2^n in hand, the twist-4 matrix element f_2^n was evaluated following the analysis presented in [22,40]. Results for Γ_1^n [Eq. (13)] from HERMES [163], SMC [149], JLab RSS [25], and E94-010 [131], and the SLAC experiments E142 [43], E143 [47], and E154 [164] were used in the updated extraction analysis. The data sets chosen for this analysis were from those experiments that published g_1^n data at constant Q^2. Since Γ_1^n is an integral over all x ($0 \le x \le 1$), the unmeasured low-x and high-x regions need to be accounted for in a consistent fashion. The method we implemented for all data sets is that shown in Ref. [22], with the exception of the HERMES and JLab data, which had already used such an extrapolation. The extrapolation calls for fitting the g_1^n data to an appropriate function over the appropriate x range. For the low-x region, the fit function was a constant $f(x) = A$, with A being a free parameter. The fit was performed over the range

TABLE XI. The extracted a_2^n over the full x range, decomposed into the low-x, measured, and high-x components. The column labeled "full" is the sum of all three regions. The uncertainties are only listed for the full extraction, where the first quantity is the statistical uncertainty and the second is the systematic uncertainty.

$\langle Q^2 \rangle$ [GeV^2]	Low x [$\times 10^{-4}$]	Measured [$\times 10^{-4}$]	High x [$\times 10^{-4}$]	Full [$\times 10^{-4}$]
3.21	−3.056	5.078	6.530	$8.552 \pm 1.761 \pm 6.125$
4.32	−3.056	5.499	2.601	$5.044 \pm 2.270 \pm 6.042$

$x_{\min} < x < x'$, where x' is the lowest measured x bin for a given experiment. The lower bound $x_{\min}$ is defined by $W = \sqrt{1000}$ GeV. The uncertainty in this low-x extrapolation was estimated by taking the difference between our fit of $f(x) = A$ with that of a simple Regge parametrization where $f(x) = Ax^{-1/2}$ [165,166]. For the high-x region, the fit function was $f(x) = A(1-x)^3$, with A being a free parameter, over the range $x' < x < x_{\max}$. The quantity x' is the highest x bin for which there were data available, and $x_{\max}$ is defined by the pion production threshold, $W = 1.12$ GeV. The fit functions for the low- and high-x regions were chosen based on the trend of the data in the last three or two bins in each case, respectively.

The elastic contribution to Γ_1^n was evaluated using the Riordan [35] and Kelly [36] parametrizations, and it was added to all of the world data. The uncertainty on the elastic contribution was estimated as the difference between using the Riordan (Kelly) parametrization for G_E^n (G_M^n) compared to using Galster [167] (dipole) for G_E^n (G_M^n). The resulting Γ_1^n data from this analysis are presented in Appendix D.

In order to extract the higher-twist contribution, the twist-2 contribution must first be removed. Using the OPE [15], Γ_1^n was expanded as an inverse power series in Q^2, revealing the higher-twist components, that was accessed by subtracting the leading twist (twist-2) contribution. The twist-2 contribution μ_2^n was calculated using Eq. (14), where α_s was parametrized according to [168] and normalized to $\alpha_s(1\ \text{GeV}^2) = 0.45 \pm 0.05$ for $\Lambda_{\text{QCD}} = 315$ MeV. We used $N_f = 3$ and $N_{\text{loop}} = 3$ [40], $g_A = 1.2723 \pm 0.0023$ [161], and $a_8 = 0.587 \pm 0.016$ [161]. Note that the values for g_A and a_8 have been updated relative to those used in Ref. [155]. At large Q^2, the higher-twist contributions should be small due to the Q^{-2} suppression; therefore, $\Gamma_1^n(Q^2) = \mu_2(Q^2)$. Because of this, the axial charge $\Delta\Sigma$ was extracted [Eq. (14)] using the highest Q^2 measurements from SLAC E154 [164] ($Q^2 = 5\ \text{GeV}^2$), SMC [149] ($Q^2 = 10\ \text{GeV}^2$), and HERMES [163] ($Q^2 = 6.5\ \text{GeV}^2$). Statistically averaging the results of these experiments yielded $Q^2 = 5.77\ \text{GeV}^2$ and $\Gamma_1^n = -0.03851 \pm 0.00535$, resulting in $\Delta\Sigma = 0.375 \pm 0.052$. This calculation is in excellent agreement with [169] and is consistent with Ref. [128], but at odds with Ref. [170]. In the latter case, we suspect this disagreement may be due in part to differing approaches in the low-x extrapolation of the world data in the various global analyses; additionally, Ref. [170] is dominated by proton data (and does not include JLab neutron data [26,28,46,131]), which may be biasing the extraction of $\Delta\Sigma$, though it is clear that there is a need for more neutron data in general.

As described in Appendix D, a fit to $\Gamma_1^n - \mu_2$ as a function of Q^2 allows the extraction of f_2^n after inserting the average a_2^n (see the beginning of Sec. V B 3) and d_2^n from the present experiment. The extracted f_2^n values are given in Table XII. This result differs from that in Ref. [155] because we have improved our analysis, where we have updated the values for g_A and a_8 used in the evaluation of the twist-2 term μ_2. We also now include uncertainties on the low-x and elastic terms in the Γ_1^n analysis mentioned above; additionally, our uncertainty on f_2^n has changed as we now consider the full error matrix of our fit function, accounting for correlations between the fit parameters A and B. Our results reported here are larger than those in Ref. [155] by about 23% (25%) for $E = 4.74$ GeV (5.89 GeV), and the systematic uncertainty has been reduced by a factor of 1.5.

TABLE XII. Extracted f_2^n results. The uncertainties given are the statistical and systematic uncertainties, respectively.

$\langle Q^2 \rangle$ (GeV^2)	f_2^n ($\times 10^{-3}$)
3.21	$53.41 \pm 0.79 \pm 25.55$
4.32	$49.66 \pm 0.83 \pm 25.99$

Our result for f_2^n is compared to that from an instanton model [171,172] and QCD sum rule calculations from E. Stein *et al.* [30,173] and Balitsky *et al.* [31], shown in Fig. 36. We find good agreement with the instanton model and reasonable agreement with the QCD sum rule result from Balitsky *et al.* Currently, there are no lattice QCD calculations of f_2^n, and it would be interesting to see what a lattice approach would yield. One can compare our result to that of Meziani *et al.* [22], who found $f_2^n = 0.034 \pm 0.043$ normalized to $Q^2 = 1\ \text{GeV}^2$ using a similar data set in their extraction of Γ_1^n. The main difference between these analyses was that they fit world neutron data to obtain a_2^n and used the results of SLAC E155x [27] for d_2^n, both at $Q^2 = 5\ \text{GeV}^2$. In contrast, this work used the measured d_2^n, and the a_2^n matrix element was obtained at the necessary Q^2 from an average over the global analyses [59,128,134–136]. The statistical uncertainty on our extracted f_2^n arises

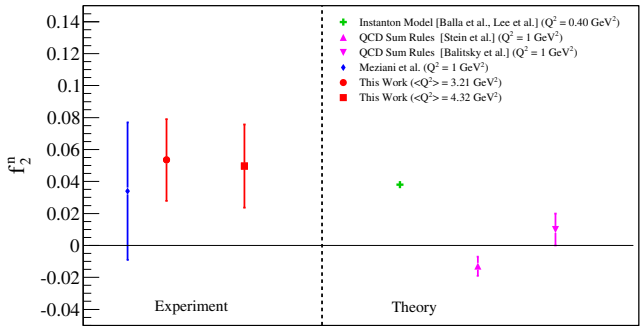

FIG. 36. Our extracted result for f_2^n as compared to that from an instanton model [171,172] and QCD sum rules [30,31,173]. The result from the analysis of Meziani *et al.* [22] is also shown. For the present data, the inner error bars represent the statistical uncertainties (smaller than the markers), while the outer error bars represent the statistical and systematic uncertainties added in quadrature.

from d_2^n, while the systematic uncertainty contains contributions from the fit to extract f_2^n, and from the a_2^n and d_2^n systematic uncertainties, but is dominated by the first.

With the matrix elements d_2^n and f_2^n evaluated, the Lorentz color force was decomposed into its electric and magnetic components via [17]

$$F_E^{y,n} = -\frac{M_n^2}{6}(2d_2^n + f_2^n), \tag{48}$$

$$F_B^{y,n} = -\frac{M_n^2}{6}(4d_2^n - f_2^n). \tag{49}$$

The results for the electric $(F_E^{y,n})$ and magnetic $(F_B^{y,n})$ color forces averaged over the volume of the neutron are shown in Table XIII and in Fig. 37, where we compare to an instanton model [171,172] and QCD sum rules from Stein *et al.* [30,173] and Balitsky *et al.* [31]. In Fig. 37, filled markers represent $F_E^{y,n}$, while open markers indicate $F_B^{y,n}$. We find that the electric and magnetic color forces are approximately equal and opposite. The electric color force component $F_E^{y,n}$ is in agreement with the instanton model, while the magnetic component $F_B^{y,n}$ is consistent with the instanton model and QCD sum rules. However, those calculations were performed at $Q^2 = 0.4$ and 1 GeV^2, respectively. Note that the values for $F_E^{y,n}$ and $F_B^{y,n}$ reported here differ from those presented in Ref. [155] because we have reevaluated the color forces using the updated f_2^n values given in Table XII. The central values for $F_E^{y,n}$ at $E = 4.74$ GeV ($E = 5.89$ GeV) have increased in magnitude by 28% (25%), while for $F_B^{y,n}$ the central values have increased in magnitude by 16% (24%). The systematic uncertainties for both $F_E^{y,n}$ and $F_B^{y,n}$ have been reduced by a factor of 1.5.

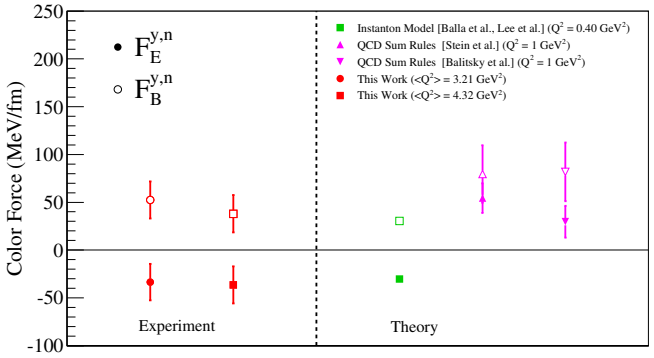

FIG. 37. Our extracted result for $F_E^{y,n}$ (filled markers) and $F_B^{y,n}$ (open markers) as compared to an instanton model [171,172] and QCD sum rules [30,31,173]. For our data points, the inner error bars represent the statistical uncertainties (smaller than the markers), while the outer error bars represent the statistical and systematic uncertainties added in quadrature.

TABLE XIII. Extracted magnetic and electric Lorentz color force components. The uncertainties given are the statistical uncertainty and the systematic uncertainty, respectively.

$\langle Q^2 \rangle$ [GeV^2]	$F_E^{y,n}$ [MeV/fm]	$F_B^{y,n}$ [MeV/fm]
3.21	$-33.53 \pm 1.32 \pm 19.07$	$52.35 \pm 2.43 \pm 19.18$
4.32	$-36.48 \pm 1.38 \pm 19.38$	$38.04 \pm 2.55 \pm 19.46$

4. The virtual photon-nucleon asymmetry A_1^n

The asymmetry A_1^n (Sec. IV D) was extracted for our DIS data at the two beam energies for $\langle Q^2 \rangle = 2.59$ GeV^2 ($E = 4.74$ GeV) and $\langle Q^2 \rangle = 3.67$ GeV^2 ($E = 5.89$ GeV); the results are given in Tables XIV and XV. These results were averaged using the statistical uncertainty as the weight, while the systematic uncertainties were averaged using equal weights. The averaged results, first published in [174], are given in Table XVI and plotted in Fig. 38. The systematic uncertainties are outlined in tables given in Appendix E 6. The biggest contribution to the uncertainty is from the effective proton polarization. Our result is consistent with the trend seen in current DIS data from SLAC E142 [43] and E154 [164], HERMES [45], and JLab E99-117 [28,46]. Although this experiment was optimized for the measurement of d_2^n, we obtained a data set with uncertainties that are competitive with the previous JLab data from E99-117. Our extraction provides a proof-of-principle measurement in an open-geometry detector (BigBite) yielding data with competitive uncertainties compared to the majority of the world data in the mid-x range, and showing a zero crossing at $x \approx 0.5$. Our data tend to follow the trend of the pQCD-based parametrization that includes orbital angular momentum [50], possibly indicating the importance of orbital angular momentum in the spin of the nucleon. Our result also shows good agreement with the NJL-type model from Cloët *et al.* [52]. Dyson-Schwinger equation treatment predictions [53] are presented at $x = 1$ (Fig. 38).

5. The structure function ratio g_1^n/F_1^n

Similar to the A_1^n analysis (Sec. V B 4), the g_1^n/F_1^n ratio was extracted for our DIS data at each beam energy for $\langle Q^2 \rangle = 2.59$ GeV^2 ($E = 4.74$ GeV) and

TABLE XIV. Results for A_1^n and g_1^n/F_1^n for $E = 4.74$ GeV. The uncertainties given are the statistical and systematic uncertainties, respectively.

$\langle x \rangle$	A_1^n	g_1^n/F_1^n
0.277	$0.012 \pm 0.071 \pm 0.008$	$0.007 \pm 0.068 \pm 0.010$
0.325	$0.011 \pm 0.043 \pm 0.009$	$0.008 \pm 0.041 \pm 0.008$
0.374	$0.102 \pm 0.037 \pm 0.014$	$0.065 \pm 0.034 \pm 0.011$
0.424	$-0.064 \pm 0.040 \pm 0.014$	$-0.066 \pm 0.038 \pm 0.013$
0.473	$-0.044 \pm 0.051 \pm 0.015$	$-0.058 \pm 0.047 \pm 0.014$

TABLE XV. Results for A_1^n and g_1^n/F_1^n for $E = 5.89$ GeV. The uncertainties given are the statistical and systematic uncertainties, respectively.

$\langle x \rangle$	A_1^n	g_1^n/F_1^n
0.277	$0.127 \pm 0.116 \pm 0.035$	$0.143 \pm 0.112 \pm 0.014$
0.325	$-0.031 \pm 0.058 \pm 0.009$	$-0.019 \pm 0.056 \pm 0.009$
0.374	$0.035 \pm 0.049 \pm 0.010$	$0.031 \pm 0.046 \pm 0.009$
0.424	$-0.039 \pm 0.053 \pm 0.013$	$-0.049 \pm 0.050 \pm 0.012$
0.474	$-0.044 \pm 0.066 \pm 0.017$	$-0.044 \pm 0.062 \pm 0.015$
0.524	$0.109 \pm 0.088 \pm 0.019$	$0.098 \pm 0.082 \pm 0.017$
0.573	$0.135 \pm 0.126 \pm 0.023$	$0.132 \pm 0.116 \pm 0.021$

$\langle Q^2 \rangle = 3.67$ GeV^2 ($E = 5.89$ GeV). These data are given in Tables XIV and XV. The results were averaged using the statistical uncertainty as the weight, and systematic uncertainties were averaged using equal weights. The averaged results, first published in [174], are given in Table XVI and plotted in Fig. 39. The systematic uncertainties are given in tables presented in Appendix E 6. The biggest contribution to the uncertainty is from the effective proton polarization and from the fit to g_1^p/F_1^p data. Our results are comparable to the JLab E99-117 data [28,46] in reach and precision, and are consistent with the trend seen in the DIS data from SLAC E143 [43] and E155 [175] as shown in Fig. 39.

C. Flavor decomposition via the quark-parton model

Under the quark-parton model [176], if one assumes that the strange quark distributions $s(x)$, $\bar{s}(x)$, $\Delta s(x)$, and $\Delta\bar{s}(x)$ are negligible for $x > 0.3$, and neglecting any Q^2 dependence in the ratio of structure functions, the polarized-to-unpolarized quark ratios can be extracted through Eqs. (27) and (28). We utilized the R^{du} ratio from the CJ12 [143] model. Using our fit to the g_1^p/F_1^p world data sets, we obtained at leading order the quantities $(\Delta u + \Delta\bar{u})/(u + \bar{u})$ and $(\Delta d + \Delta\bar{d})/(d + \bar{d})$ for $E = 4.74$ GeV (5.89 GeV) where $\langle Q^2 \rangle = 2.59$ GeV^2 (3.67 GeV^2). The results are tabulated in Tables XVII and XVIII. Averaging the two data sets, we obtained the values given in Table XIX at $\langle Q^2 \rangle = 3.08$ GeV^2. These averaged results, first published in [174], are compared to various world data

TABLE XVI. Results for A_1^n and g_1^n/F_1^n averaged over our $E = 4.74$ and 5.89 GeV results for $\langle Q^2 \rangle = 3.08$ GeV^2. The uncertainties given are the statistical and systematic uncertainties, respectively.

$\langle x \rangle$	A_1^n	g_1^n/F_1^n
0.277	$0.043 \pm 0.060 \pm 0.022$	$0.044 \pm 0.058 \pm 0.012$
0.325	$-0.004 \pm 0.035 \pm 0.009$	$-0.002 \pm 0.033 \pm 0.009$
0.374	$0.078 \pm 0.029 \pm 0.012$	$0.053 \pm 0.028 \pm 0.010$
0.424	$-0.055 \pm 0.032 \pm 0.014$	$-0.060 \pm 0.030 \pm 0.012$
0.474	$-0.044 \pm 0.040 \pm 0.016$	$-0.053 \pm 0.037 \pm 0.015$
0.548	$0.118 \pm 0.072 \pm 0.021$	$0.110 \pm 0.067 \pm 0.019$

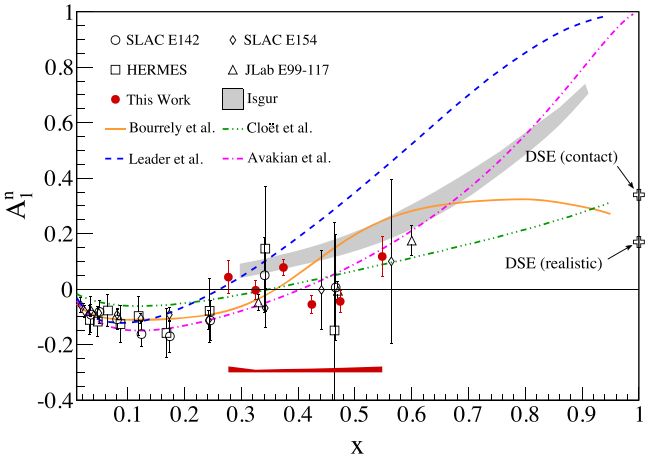

FIG. 38. Our measured A_1^n results compared to world data [28,43–46] and a pQCD-inspired global analysis (dashed curve) [49], a statistical quark model (solid curve) [51], a relativistic CQM model (gray band) [48], and a pQCD-based parametrization including orbital angular momentum (dash-dotted curve) [50]. An NJL-type model (dash–triple-dotted curve) is also shown [52]. Dyson-Schwinger equation treatment predictions [53] are presented at $x = 1$. The band at the bottom of the plot indicates the systematic uncertainty for the present data.

[28,54–56] and theoretical calculations [50,51,53,59] in Fig. 40. The uncertainty due to neglecting the strange contribution was determined by computing Eqs. (27) and (28) with the strange component *included* [86],

$$\frac{\Delta u + \Delta\bar{u}}{u + \bar{u}} = \left(\frac{\Delta u + \Delta\bar{u}}{u + \bar{u}}\right)_{s,\bar{s}=0} + \frac{s + \bar{s}}{u}\left[\frac{4}{15}\frac{g_1^p}{F_1^p} - \frac{1}{15}\frac{g_1^n}{F_1^n} - \frac{1}{5}\frac{\Delta s + \Delta\bar{s}}{s + \bar{s}}\right], \quad (50)$$

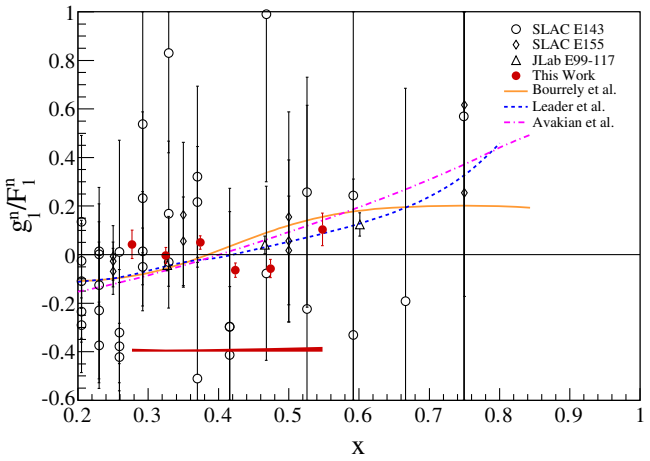

FIG. 39. Our measured g_1^n/F_1^n results, compared to world data [28,43,46,164], and an NLO QCD global analysis [59] (dashed curve) and pQCD-inspired fit [50] (dash-dotted curve), and a statistical quark model [134] (solid curve). The band at the bottom of the plot indicates the systematic uncertainty for our data set.

TABLE XVII. Results for $(\Delta u+\Delta\bar{u})/(u+\bar{u})$ and $(\Delta d+\Delta\bar{d})/(d+\bar{d})$ at $E=4.74$ GeV. The uncertainties given are the statistical and systematic uncertainties, respectively.

$\langle x\rangle$	$(\Delta u+\Delta\bar{u})/(u+\bar{u})$	$(\Delta d+\Delta\bar{d})/(d+\bar{d})$
0.277	$0.437\pm0.013\pm0.031$	$-0.219\pm0.110\pm0.028$
0.325	$0.482\pm0.008\pm0.036$	$-0.267\pm0.069\pm0.032$
0.374	$0.513\pm0.006\pm0.043$	$-0.218\pm0.060\pm0.038$
0.424	$0.570\pm0.006\pm0.050$	$-0.508\pm0.068\pm0.051$
0.473	$0.596\pm0.007\pm0.063$	$-0.566\pm0.088\pm0.069$

TABLE XVIII. Results for $(\Delta u+\Delta\bar{u})/(u+\bar{u})$ and $(\Delta d+\Delta\bar{d})/(d+\bar{d})$ at $E=5.89$ GeV. The uncertainties given are the statistical and systematic uncertainties, respectively.

$\langle x\rangle$	$(\Delta u+\Delta\bar{u})/(u+\bar{u})$	$(\Delta d+\Delta\bar{d})/(d+\bar{d})$
0.277	$0.410\pm0.022\pm0.032$	$0.001\pm0.182\pm0.027$
0.325	$0.487\pm0.010\pm0.037$	$-0.314\pm0.094\pm0.033$
0.374	$0.518\pm0.008\pm0.045$	$-0.281\pm0.081\pm0.040$
0.424	$0.567\pm0.008\pm0.051$	$-0.482\pm0.090\pm0.051$
0.474	$0.593\pm0.009\pm0.063$	$-0.547\pm0.116\pm0.071$
0.524	$0.594\pm0.012\pm0.070$	$-0.352\pm0.165\pm0.083$
0.573	$0.606\pm0.015\pm0.085$	$-0.365\pm0.250\pm0.111$

$$\frac{\Delta d+\Delta\bar{d}}{d+\bar{d}}=\left(\frac{\Delta u+\Delta\bar{u}}{u+\bar{u}}\right)_{s,\bar{s}=0}+\frac{s+\bar{s}}{d}\left[\frac{4}{15}\frac{g_1^n}{F_1^n}-\frac{1}{15}\frac{g_1^n}{F_1^n}-\frac{1}{5}\frac{\Delta s+\Delta\bar{s}}{s+\bar{s}}\right], \quad (51)$$

where the terms $(\cdots)_{s,\bar{s}=0}$ are defined in Eqs. (27) and (28). The second term in Eqs. (50) and (51) is the strange contribution, which was evaluated using various parametrizations [59,128,134,135,143] and taking the maximum difference between calculations using all possible model combinations as the uncertainty. It was found to be sizable in the lowest x bins for the down-quark results, but was small for $x\geq 0.424$. For the up-quark results, the strange uncertainty was small. The uncertainty due to neglecting the strange contribution is included in our reported uncertainties.

TABLE XIX. Results for $(\Delta u+\Delta\bar{u})/(u+\bar{u})$ and $(\Delta d+\Delta\bar{d})/(d+\bar{d})$ averaged over the two beam energies, for $\langle Q^2\rangle=3.08$ GeV^2. The uncertainties given are the statistical and systematic uncertainties, respectively.

$\langle x\rangle$	$(\Delta u+\Delta\bar{u})/(u+\bar{u})$	$(\Delta d+\Delta\bar{d})/(d+\bar{d})$
0.277	$0.430\pm0.011\pm0.031$	$-0.160\pm0.094\pm0.028$
0.325	$0.484\pm0.006\pm0.037$	$-0.283\pm0.055\pm0.032$
0.374	$0.515\pm0.005\pm0.044$	$-0.241\pm0.048\pm0.039$
0.424	$0.569\pm0.005\pm0.051$	$-0.499\pm0.054\pm0.051$
0.474	$0.595\pm0.006\pm0.063$	$-0.559\pm0.070\pm0.070$
0.548	$0.598\pm0.009\pm0.077$	$-0.356\pm0.138\pm0.097$

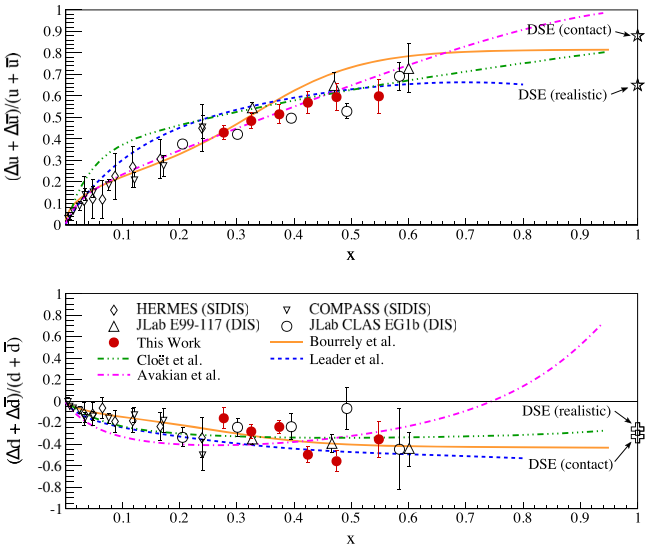

FIG. 40. Our combined $E=4.74$ and 5.89 GeV data for the up- and down-quark ratios. Our results are compared to existing data [28,54–56], where the error bars on all data sets are the in-quadrature sum of the statistical and systematic uncertainties. Also presented is a statistical quark model (solid curve) [51], an NLO QCD global analysis from Leader *et al.* (dashed curve) [59], and a pQCD analysis including orbital angular momentum from Avakian *et al.* (dash-dotted curve) [50]. An NJL-type model from Cloët *et al.* (dash–triple-dotted curve) [52] is also shown. DSE predictions [53] are shown at $x=1$.

The extracted up- and down-quark ratios agree with the general trend of the world data within our uncertainties. Our analysis supports the notion that the down-quark ratio stays negative into the large x region, with no clear indication that it turns positive toward $x\simeq 0.6$, as predicted by the calculation of Avakian *et al.* [50].

The largest contribution to our systematic uncertainties on the up-quark ratio is from our fit to the g_1^p/F_1^p data, while for the down-quark ratio, the largest contributions are due to the g_1^p/F_1^p fit and the d/u ratio. An overview of the systematic uncertainties is given in Appendix E 7.

VI. CONCLUSIONS

Scattering a longitudinally polarized electron beam of energies of $E=4.74$ GeV and 5.89 GeV from a polarized ^{3}He target in two orientations, longitudinal and transverse (with respect to the electron beam momentum), we measured the unpolarized electron-scattering cross section with the LHRS and the electron double-spin asymmetries with the BigBite spectrometer, with both spectrometers set at 45° with respect to the beam line. Combining the unpolarized cross sections and double-spin asymmetries allowed the extraction of the twist-3 matrix element d_2^n. This quantity was extracted at two $\langle Q^2\rangle$ values of 3.21 GeV^2 and 4.32 GeV^2. The result at the lower $\langle Q^2\rangle$ value is small and negative, while that for the higher $\langle Q^2\rangle$ value is consistent with zero. The data indicate a trend toward the lattice QCD [34] calculation at

$Q^2 = 5$ GeV^2. The extracted d_2^n values are also consistent with predictions of chiral soliton [32] and bag [33,38,39] models. The size of the present d_2^n results predicts the twist-3 contribution is small.

Utilizing our measured d_2^n twist-3 matrix element combined with global analyses for a_2^n and world data on Γ_1^n, we have extracted the twist-4 matrix element f_2^n. This matrix element is observed to be larger than d_2^n in magnitude, resulting in approximately equal and opposite Lorentz color magnetic and electric forces in the neutron. The results for f_2^n are consistent with instanton model calculations [171,172] and a QCD sum-rule calculation [30]. The extracted values for $F_E^{y,n}$ and $F_B^{y,n}$ are in agreement with the instanton model calculations of [171,172], while the value for $F_B^{y,n}$ is additionally in accordance with QCD sum-rule calculations from [30,31]. We look forward to lattice QCD calculations of the f_2^n matrix element, not yet available at this time due to their difficulty, before the new wave of planned experiments in the 12 GeV upgrade era of Jefferson Lab to measure d_2 and f_2 with more precision.

Following a similar analysis procedure to the one used for d_2^n, we extracted the a_2^n matrix element using our $g_1^{^3\mathrm{He}}$ data. Our a_2 results are positive for both $\langle Q^2 \rangle = 3.21$ and 4.32 GeV^2, with an improved precision compared to the currently published data and lattice calculations.

The extracted virtual photon asymmetry A_1^n is consistent with the current world data, especially JLab E99-117 [28,46], and shows good agreement with pQCD calculations that incorporate quark orbital angular momentum [50]. This suggests that orbital angular momentum may play an important role in the spin of the nucleon.

The measured structure function ratio of g_1^n/F_1^n shows a similar trend to JLab E99-117 [28,46], adding higher precision data to the world data set.

Fitting the world g_1/F_1 data on the proton allowed the extraction of $(\Delta u + \Delta\bar{u})/(u + \bar{u})$ and $(\Delta d + \Delta\bar{d})/(d + \bar{d})$ when using the CJ12 [143] model for d/u. The extracted up-quark ratio is consistent with existing measurements and models, and its uncertainty is dominated by our fit to the world g_1^p/F_1^p data. The down-quark ratio is observed to remain negative into the large-x region, with no clear indication of a change to positive values in the range of $x \simeq 0.75$ as predicted in Ref. [50]. The down-quark ratio is very sensitive to the d/u ratio, as is evident in the systematic uncertainties. Better precision on d/u from the projected experiment [177] at Jefferson Lab in the 12 GeV upgrade era will help to constrain the $(\Delta d + \Delta\bar{d})/(d + \bar{d})$ ratio.

A future experiment [178] proposed at Jefferson Lab calls for an even higher precision measurement of d_2^n at four central Q^2 bins in a range from 2 GeV^2 to 7 GeV^2. While our data provide a good understanding of d_2^n at $Q^2 = 3.21$ and 4.32 GeV^2, those data will provide a direct comparison to the lattice QCD calculation at $Q^2 = 5$ GeV^2. There are also two dedicated A_1^n experiments approved to run at Jefferson Lab [179,180] that aim to extend DIS A_1^n measurements to larger x ($\sim$0.77) in addition to studying the Q^2 evolution of the asymmetry. These measurements are important for broadening our insight into the large-x spin structure of the nucleon, as suggested by the results[1] presented in this paper.

ACKNOWLEDGMENTS

We would like to thank the Jefferson Lab Accelerator Division and Hall A staff for their efforts, which resulted in the successful completion of the experiment. We would also like to thank M. Burkardt, L. Gamberg, W. Melnitchouk, and J. Soffer for theoretical support and useful discussions. This material is based upon work supported by the U.S. Department of Energy (DOE) Office of Science under Awards No. DE-FG02-94ER40844 and No. DE-FG02-87ER40315. Jefferson Lab is operated by the Jefferson Science Associates, LLC, under DOE Grant No. DE-AC05-060R23177.

APPENDIX A: DEEP INELASTIC ELECTRON SCATTERING FORMALISM

1. Structure functions and cross sections

In electron scattering, the electrons are accelerated to high energies and scatter from a nuclear or nucleon target. In practice, the target is typically fixed. The electron interacts with the target by exchanging a virtual photon with the target object, transferring its energy and momentum to the target. An advantage of lepton scattering is that the interaction at the leptonic vertex is solely described by quantum electrodynamics, which simplifies the mathematics. The electromagnetic nature of the interaction also results in the process being a "clean" probe into the structure of the nucleon, where the QCD physics is contained entirely in the description of the nucleon and is not convoluted with the leptonic probe.

To describe the process more quantitatively, consider Fig. 41. The incident and scattered electrons have the four-momenta $k = (E, \vec{k})$ and $k' = (E', \vec{k}')$, respectively. The target has a four-momentum of $p = (E_T, \vec{p})$. The virtual photon exchanged between the incident electron and the target has the four-momentum $q = (\nu, \vec{q})$. If the incident electron has enough energy, the target can break up into a number of distinct hadrons; otherwise, the target will remain intact. In the latter case, the recoiling target object would have a four-momentum p' in the final hadronic state. Electron scattering data are presented and discussed in terms of a number of Lorentz-invariant variables, namely ν, y, Q^2, W, and x. Since the four-momentum at each vertex is conserved, we begin by defining q in terms of the incoming and outgoing electron four-momenta,

[1]The results presented in this work may downloaded as raw data files from [181].

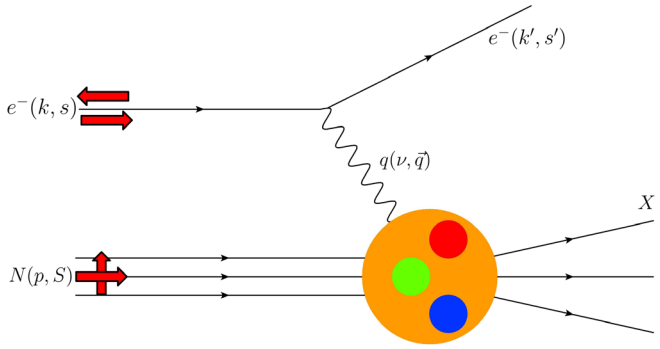

FIG. 41. A cartoon describing inclusive polarized electron-nucleon scattering. The large arrows indicate possible spin orientations of the incident electron and nucleon. The quantities s and S indicate the spin four-vectors of the electron and nucleon, respectively. The other kinematic variables are described in the text.

$$q = k - k' = (E - E', \vec{k} - \vec{k}') = (\nu, \vec{q}), \tag{A1}$$

where ν can be defined in an invariant form,

$$\nu \equiv p \cdot q / M, \tag{A2}$$

with M being the mass of the nucleon. In the target rest frame, $p = (M, \vec{0})$, so Eq. (A2) reduces to $\nu = E - E'$, and is known as the *electron energy loss*. The fractional energy loss, y, can be defined in an invariant form,

$$y \equiv \frac{p \cdot q}{q \cdot k}, \tag{A3}$$

which simplifies to the noninvariant form $y = (E - E')/E$.

The four-momentum transfer squared, q^2, always evaluates to less than or equal to zero. For convenience, we define a positive quantity Q^2,

$$Q^2 \equiv -q^2 = 4EE'\sin^2(\theta/2), \tag{A4}$$

where θ is the scattering angle of the electron in the laboratory frame and we have neglected the electron mass.

Shifting our focus to the hadronic side of Fig. 41, there are two possibilities for the final state: there is one object (i.e., the target remains intact) or several, determined by the energy with which the target is probed. Furthermore, the measured interaction may be described by two general terms: *exclusive* or *inclusive* scattering. In the case of exclusive scattering, the scattered electron *and* all final-state hadrons are detected; there is also the case of detecting an electron and at least one particle in the final state, which is called *semi-inclusive*. For inclusive scattering, only the scattered electron is detected in the final state.

Inclusive scattering can be represented as $eN \to eX$, where e is the electron, N is the target nucleon, and X is the final (unmeasured) hadronic state. In the context of an unmeasured final hadronic state (which could consist of any of the multitude of particle states for a given combination of ν and Q^2 values), we can define the invariant mass of the system, W,

$$W^2 \equiv (q + p)^2 = M^2 + 2M\nu - Q^2. \tag{A5}$$

Finally, we come to the variable x. It is defined in terms of the other invariants ν and Q^2 as

$$x \equiv \frac{Q^2}{2p \cdot q} = \frac{Q^2}{2M\nu}. \tag{A6}$$

The simplest interpretation of x comes in the infinite momentum frame, where the nucleon is traveling with a large momentum along $\vec{q}$. In this frame, the active quark in the interaction (struck by the virtual photon) carries the momentum fraction x of the nucleon momentum in the leading-order DIS process [182].

The DIS region is characterized by $W > 2$ GeV, where ν and Q^2 become large enough so that the quarks can be resolved inside the nucleon. In this case, the electron is scattering from an asymptotically free quark (or antiquark) in the nucleon.

Consider scattering unpolarized electrons from pointlike, unpolarized spin-1/2 particles that are infinitely heavy with a charge of $+1$. In this case, energy conservation dictates $E' = E$, and the cross section is given by

$$\left(\frac{d\sigma}{d\Omega}\right)_{\text{Mott}} = \frac{\alpha^2\cos^2(\theta/2)}{4E^2\sin^4(\theta/2)}, \tag{A7}$$

with θ being the scattering angle of the electron. This quantity is known as the *Mott cross section*. However, since the nucleon is a composite object and is not infinitely massive, the cross section is more complicated than that seen in Eq. (A7), and is given by

$$\frac{d^3\sigma}{d\Omega dE'} = \left(\frac{d\sigma}{d\Omega}\right)_{\text{Mott}} \left[\frac{1}{\nu} F_2(x, Q^2) + \frac{2\tan^2(\theta/2)}{M} F_1(x, Q^2)\right], \tag{A8}$$

where F_1 and F_2 are the unpolarized structure functions, and are related to one another through Eq. (43).

For experiments that use targets that are not nucleons ($A \neq 1$), there are two conventions for expressing the quantities F_1 and F_2. The first is *per nucleon*, written as F_1/A and F_2/A. The second is *per nucleus*, where the structure functions are reported without dividing by A. The latter representation is used in this paper.

When both the incident electron beam and target are polarized, one can access the spin structure functions g_1 and g_2. A full discussion may be found in Ref. [123]. The polarized cross section difference for when the target spin (double arrows) and electron spin (single arrows) are polarized along the direction of the electron momentum is given as

$$\frac{d^2\sigma^{\downarrow,\Uparrow}}{d\Omega dE'} - \frac{d^2\sigma^{\uparrow,\Uparrow}}{d\Omega dE'} = \frac{4\alpha^2}{Q^2}\frac{E'}{\nu E}[(E + E'\cos\theta)g_1(x,Q^2) - 2Mxg_2(x,Q^2)]. \quad \text{(A9)}$$

When the target spin is perpendicular to the electron spin, the cross section difference is written as

$$\frac{d^2\sigma^{\downarrow,\Rightarrow}}{d\Omega dE'} - \frac{d^2\sigma^{\uparrow,\Rightarrow}}{d\Omega dE'} = \frac{4\alpha^2}{Q^2}\frac{E'^2}{\nu E}\sin\theta\left[g_1(x,Q^2) + \frac{2ME}{\nu}g_2(x,Q^2)\right]. \quad \text{(A10)}$$

2. Bjorken scaling, the quark-parton model, and scaling violation

When probing an object of finite size, the measurement will depend upon the spatial resolution of the probe; in the case of electron scattering, this is Q^2, the negative of the momentum transferred to the target squared. If we increase Q^2 so that we can resolve the internal structure of the nucleon, the quarks will become visible. At this point, inelastic electron-nucleon scattering may be seen as elastic scattering from a single quark, while the other quarks remain undisturbed. Considering that quarks are pointlike particles, increasing the resolution Q^2 will no longer affect the interaction.

In the limit where $Q^2 \to \infty$ and $\nu \to \infty$, with $x = Q^2/(2M\nu)$ fixed (the Bjorken limit), the phenomenon where experimental observables lose their Q^2 dependence is known as *Bjorken scaling* [183]. As a result, the structure functions depend upon a single variable x. Furthermore, the F_2 structure function can be related to the F_1 structure function by the *Callan-Gross relation* [184],

$$F_2(x) = 2xF_1(x). \quad \text{(A11)}$$

To connect the quark behavior to the structure functions, we turn to the quark-parton model (QPM). In this model, deep inelastic scattering of electrons from nucleons is described as the incoherent scattering of electrons from free partons (quarks and antiquarks) inside the nucleon [176], via the exchange of a virtual photon. Therefore, the nucleon structure functions F_1 and g_1 can be written in terms of the PDFs [176,182],

$$F_1(x) = \frac{1}{2}\sum_i e_i^2 q_i(x), \quad \text{(A12)}$$

$$g_1(x) = \frac{1}{2}\sum_i e_i^2 \Delta q_i(x), \quad \text{(A13)}$$

with $q = q^{\uparrow}(x) + q^{\downarrow}(x)$ and $\Delta q = q^{\uparrow}(x) - q^{\downarrow}(x)$, where $\uparrow$ ($\downarrow$) indicates quark spin parallel (antiparallel) to the parent nucleon spin.

The scaling behavior of the structure functions is only exact in the limit of infinite Q^2 and ν. At finite values of Q^2 and ν, it is only an approximation. In reality, the quarks participating in the interaction with the electron may radiate gluons before or after scattering. Such processes result in an infinite cross section and can only be treated properly when all other processes of the same order are considered. These gluonic radiative corrections result in the cross section acquiring a logarithmic Q^2 dependence, which can be computed exactly in pQCD under the formalism of the Dokshitzer-Gribov-Lipatov-Altarelli-Parisi (DGLAP) evolution equations [9]. As a result, the Q^2 dependence manifests itself in the structure functions.

As a result of the scaling violation, we recast the PDFs and the structure functions in terms of both x and Q^2. In particular, the definition of the PDF is now $q^{\uparrow(\downarrow)}(x,Q^2)$: this is the probability of finding a quark q with its spin parallel (antiparallel) to its parent nucleon with momentum fraction x *when viewed at an energy scale* $Q = \sqrt{Q^2}$.

The physical interpretation tied to the scaling violation is that structure functions at low Q^2 are dominated by three *valence* quarks "dressed" by sea quarks (manifesting as $q - \bar{q}$ pairs) and gluons. As Q^2 is increased, the resolving power increases, allowing for sensitivity to the "bare" quarks and gluons which make up the nucleon.

3. The resonance region

Because of the kinematics of our experiment, about half of our data set corresponds to the DIS regime, while the other corresponds to the *resonance* region. With this in mind, we give a brief description of the resonance region.

When ν and Q^2 have values such that $1.2 < W < 2$ GeV, we explore the substructure of the nucleon. In this energy range, the quarks that make up the nucleon collectively absorb the energy of the virtual photon, leading to unstable excited states of the nucleon called *nucleon resonances*. The most prominent resonance occurs at $W = 1.232$ GeV, and is known as the Δ resonance. Higher resonances are also possible at $W > 1.4$ GeV, but are difficult to discern from one another, as their peaks and tails tend to overlap.

4. The virtual photon-nucleon asymmetry A_1

Let us consider a scattering interaction in which the nucleon is longitudinally polarized, while the virtual photon is circularly polarized with a helicity of ± 1. As a result, two possible helicity-dependent cross sections for a given nucleon polarization arise, denoted $\sigma_{3/2}$ and $\sigma_{1/2}$. The subscripts denote the projection of the total spin of the virtual photon-nucleon system along the direction of the virtual photon momentum [47,98]. When the virtual photon spin is parallel (antiparallel) to the nucleon spin, they add to 3/2 (1/2). From these two cross sections, the A_1 asymmetry is formed as

$$A_1 \equiv \frac{\sigma_{1/2} - \sigma_{3/2}}{\sigma_{1/2} + \sigma_{3/2}}. \tag{A14}$$

In terms of the structure functions, A_1 may be written as [123]

$$A_1(x, Q^2) = \frac{g_1(x, Q^2) - \gamma^2 g_2(x, Q^2)}{F_1(x, Q^2)}. \tag{A15}$$

At large Q^2, $A_1 \approx g_1/F_1$. This can be seen by observing that $\gamma^2 \to 0$ as Q^2 gets increasingly large. A conceptual argument on the quark level is as follows: if the spin of the virtual photon is antiparallel to that of the quark, then the virtual photon can be absorbed and the quark spin is flipped; however, if the spins are *parallel*, then the absorption of the virtual photon is forbidden, since the total projection of the spins along $\vec{q}$ is $3/2$ and the quark is a spin-$1/2$ particle. The mathematical form of the approximation can be illustrated using this physical interpretation: for the case where the spins of the nucleon and virtual photon are parallel ($\sigma_{3/2}$), then the quark that *can* absorb the virtual photon has its spin antiparallel to the nucleon spin. This translates to $\sigma_{3/2} \sim \sum_i e_i^2 q_i^{\downarrow}(x)$. A similar argument may be made for the $\sigma_{1/2}$ case where only quarks with spins parallel to the parent nucleon can absorb virtual photons. Thus, we have $\sigma_{1/2} \sim \sum_i e_i^2 q_i^{\uparrow}(x)$. Rewriting A_1 in terms of these approximations, we obtain

$$A_1 \sim \frac{\sum_i e_i^2 [q_i^{\uparrow}(x) - q_i^{\downarrow}(x)]}{\sum_i e_i^2 [q_i^{\uparrow}(x) + q_i^{\downarrow}(x)]} = \frac{\sum_i e_i^2 \Delta q_i(x)}{\sum_i e_i^2 q_i(x)} = \frac{g_1(x)}{F_1(x)}, \tag{A16}$$

where the last term arises from the quark-parton model description of the F_1 and g_1 structure functions [Eqs. (A12) and (A13)].

The A_1 asymmetry is a ratio of structure functions ($\approx g_1/F_1$), and as a result there is very little Q^2 dependence. This is because g_1 and F_1 follow the same Q^2 evolution described by the DGLAP equations [9] which tends to cancel in the ratio, leading to A_1 being roughly Q^2 independent.

5. Electron asymmetries

The virtual photon-nucleon asymmetry A_1 is defined in terms of a ratio of the difference in virtual photon cross sections to their sum. Because of the difficulty associated with aligning the virtual photon spin along the direction of the nucleon spin, another approach is utilized to measure A_1 that consists of aligning the *incident electron* spin relative to the direction of the nucleon spin. The extraction of the *electron asymmetries* allows the determination of A_1. After some algebra, the electron asymmetries (Sec. I B) may be written as [156]

$$A_{\parallel} = D(A_1 + \eta A_2), \tag{A17}$$

$$A_{\perp} = d(A_2 - \eta A_1). \tag{A18}$$

The asymmetry A_2 is defined as $A_2 \equiv 2\sigma_{LT}/(\sigma_{1/2} + \sigma_{3/2})$, where σ_{LT} is the cross section describing the interference between virtual photons with longitudinal and transverse polarizations. In the QPM, there is no clear interpretation for σ_{LT}, and in turn A_2, as there is for $\sigma_{1/2}$, $\sigma_{3/2}$, and A_1 [185]. From Eqs. (A17) and (A18), one can write A_1 and A_2 in terms of the double-spin asymmetries $A_{\parallel}$ and $A_{\perp}$. Similar equations may be obtained for g_1/F_1 and g_2/F_1 [156]. The equations for A_1 and g_1/F_1 are shown in Sec. I C.

6. Spin structure functions

The spin structure functions g_1 and g_2 may be obtained from the measured unpolarized cross section σ_0 and the double-spin asymmetries $A_{\parallel}$ and $A_{\perp}$ through

$$g_1 = \frac{MQ^2}{4\alpha^2} \frac{2y}{(1-y)(2-y)} \sigma_0 [A_{\parallel} + \tan(\theta/2) A_{\perp}], \tag{A19}$$

$$g_2 = \frac{MQ^2}{4\alpha^2} \frac{y^2}{(1-y)(2-y)} \sigma_0 \times \left[-A_{\parallel} + \frac{1 + (1-y)\cos\theta}{(1-y)\sin\theta} A_{\perp} \right]. \tag{A20}$$

APPENDIX B: QUARK-GLUON CORRELATIONS

1. The operator product expansion and twist

The OPE allows the separation of the perturbative and nonperturbative components in structure functions at finite Q^2. This concept is illustrated in the product of two *local* quark (or gluon) operators $\mathcal{O}_a(d)\mathcal{O}_b(0)$ separated by a distance d in the limit of $d \to 0$,

$$\lim_{d \to 0} \mathcal{O}_a(d)\mathcal{O}_b(0) = \sum_k c_{abk}(d)\mathcal{O}_k(0), \tag{B1}$$

where the coefficient functions c_{abk} are the Wilson coefficients and contain the perturbative part, which can be computed using perturbation theory since nonperturbative effects occur at distances much larger than d [11]. The nonperturbative components manifest in $\mathcal{O}_k(0)$ and contribute to the cross section on the order of $x^{-n}(Q/M)^{D-2-n}$. The exponents n and D are the spin and (mass) dimension of the operator, respectively. The quantity $Q = \sqrt{Q^2}$. The *twist* τ of the operator is defined by

$$\tau \equiv D - n. \tag{B2}$$

At large Q^2, $\tau = 2$ terms dominate in the OPE; at low Q^2, higher-twist ($\tau > 2$) operators become important.

2. Cornwall-Norton moments and Nachtmann moments

Using the OPE, an infinite set of sum rules may be derived under a twist expansion of the spin structure functions g_1 and g_2 [123]. Such expansions of g_1 and g_2 are known as the CN moments [156],

$$\int_0^1 x^{n-1} g_1(x, Q^2) dx = \frac{1}{2} a_{n-1}, \qquad n = 1, 3, 5, \ldots, \tag{B3}$$

$$\int_0^1 x^{n-1} g_2(x, Q^2) dx = \frac{n-1}{2n}(d_{n-1} - a_{n-1}), \qquad n = 3, 5, 7, \ldots, \tag{B4}$$

where n indicates the nth moment. In Eqs. (B3) and (B4), only twist-2 and twist-3 contributions are considered. The quantities a_{n-1} and d_{n-1} represent the twist-2 and twist-3 matrix elements, respectively [186]. The expansions are only over odd integers, which is a result of the symmetry of the structure functions under charge conjugation [187].

The twist-3 matrix elements d_{n-1} may be accessed by combining Eqs. (B3) and (B4). One obtains [156]

$$\int_0^1 x^{n-1} \left[g_1(x, Q^2) + \frac{n}{n-1} g_2(x, Q^2) \right] dx = \frac{d_{n-1}}{2}, \qquad n \geq 3. \tag{B5}$$

Choosing $n = 3$ yields the equation for d_2 [cf. Eq. (4)].

The study of higher twist in structure functions has traditionally been done through the formalism of the CN moments; however, the exact relation of the CN moments to the dynamical higher-twist contributions has come into question in recent analyses [156,188]. It is argued that the CN moments are valid only when the terms connected to the finite mass of the nucleon are neglected. Such terms are known as *target mass corrections*. These corrections are related to twist-2 operators and are of order $\mathcal{O}(M^2/Q^2)$. Analogous to the CN moments, the Nachtmann moments M_1 and M_2 can be used to separate the higher-twist contribution from the target mass corrections [157,189]. They are defined as [25,156,190]

$$M_1^n(Q^2) \equiv \frac{1}{2} a_{n-1} = \frac{1}{2} \tilde{a}_n E_1^n = \int_0^1 \frac{\xi^{n+1}}{x^2} \left[\frac{x}{\xi} - \frac{n^2}{(n+2)^2} \frac{M^2 x \xi}{Q^2} g_1(x, Q^2) - \frac{4n}{n+2} \frac{M^2 x^2}{Q^2} g_2(x, Q^2) \right] dx, \qquad n = 1, 3, \ldots, \tag{B6}$$

$$M_2^n(Q^2) \equiv \frac{1}{2} d_{n-1} = \frac{1}{2} \tilde{d}_n E_2^n = \int_0^1 \frac{\xi^{n+1}}{x^2} \left[\frac{x}{\xi} g_1(x, Q^2) + \left(\frac{n}{n-1} \frac{x^2}{\xi^2} - \frac{n}{n+1} \frac{M^2 x^2}{Q^2} \right) g_2(x, Q^2) \right] dx, \qquad n = 3, 5, \ldots. \tag{B7}$$

where $\xi = 2x / \left(1 + \sqrt{1 + 4M^2 x^2 / Q^2} \right)$.

We have performed the analysis to extract d_2^n and a_2^n according to the CN moments and checked that result against what was obtained from using the Nachtmann moments. The difference in results between the two approaches was found to be negligible, on the order of 10^{-5} in absolute value.

APPENDIX C: FITS TO DATA

1. Cross section fits

As discussed in Sec. IV B, because of time constraints not all cross section measurements for studying pair production on ^{3}He and N_2 were carried out. To resolve the absence of those data, the data that were collected were fit to a function of the form

$$f(E_p) = \frac{1}{E_p^2} e^{(a_0 + a_1 E_p)}, \tag{C1}$$

where the scattered electron energy E_p is in GeV. This was done for σ^{e^+}, $\sigma^{e^-}_{N_2}$, and $\sigma^{e^+}_{N}$. The fits were performed in ROOT [88], and the extracted parameters and their uncertainties were obtained from the MINUIT minimization package [191]. The fits were done separately for the data sets corresponding to each beam energy. The systematic uncertainties on the fits were obtained by varying the parameters within their errors and observing the change on the fit (see Figs. 18 and 19). The parameters together with their uncertainties are listed in Table XX for the nitrogen cross section when scattered electrons were detected, $\sigma^{e^-}_{N_2}$ (LHRS set to negative polarity mode), and in Table XXI when positrons were detected, $\sigma^{e^+}_{N_2}$ (LHRS in positive polarity mode). Table XXII gives the fit parameters and their uncertainties for the unpolarized ^{3}He cross section where positrons were detected, σ^{e^+} (LHRS in positive polarity mode).

TABLE XX. Fit parameters for the nitrogen cross section (negative polarity), $\sigma^{e^-}_{N_2}$, for $E = 4.74$ GeV and $E = 5.89$ GeV.

Par.	$E = 4.74$ GeV	$E = 5.89$ GeV
a_0	$1.465 \times 10^1 \pm 4.919 \times 10^{-2}$	$1.480 \times 10^1 \pm 5.647 \times 10^{-2}$
a_1	$-1.825 \times 10^{-3} \pm 4.770 \times 10^{-5}$	$-2.123 \times 10^{-3} \pm 5.607 \times 10^{-5}$

TABLE XXI. Fit parameters for the nitrogen cross section (positive polarity), $\sigma^{e^+}_{N_2}$, for $E = 4.74$ GeV and $E = 5.89$ GeV.

Par.	$E = 4.74$ GeV	$E = 5.89$ GeV
a_0	$1.559 \times 10^{1} \pm 1.604 \times 10^{-1}$	$1.614 \times 10^{1} \pm 2.120 \times 10^{-1}$
a_1	$-4.699 \times 10^{-3} \pm 2.255 \times 10^{-4}$	$-5.232 \times 10^{-3} \pm 3.126 \times 10^{-4}$

2. g_1^p/F_1^p fit

To carry out the analysis to obtain g_1^n/F_1^n from our $g_1^{^3\mathrm{He}}/F_1^{^3\mathrm{He}}$ data, a parametrization of the g_1^p/F_1^p data was needed. We fit the world data to a three-parameter, Q^2-independent function given by

$$f(x) = p_0 + p_1 x + p_2 x^2. \tag{C2}$$

The assumption of Q^2 independence is reasonable as the Q^2 evolution in g_1 and F_1 partially cancels in the ratio to leading order and next-to-leading order in Q^2 [123]. Additionally, the world data (which are at differing Q^2) show roughly the same behavior. The world data considered were from HERMES [45], SLAC E143 [47] and E155 [139], along with CLAS EG1b [56] and CLAS EG1-DVCS [144]. First, all of these data were rebinned in x, in new bins formed based on a statistical-error-weighted average; the systematic errors of all data contributing to a new bin were averaged with equal weights to yield its systematic error. The fit result, with $\chi^2/\mathrm{ndf} = 0.91$, is shown in Fig. 42. The fit parameters were found to be

$$\begin{aligned} p_0 &= 0.035 \pm 0.008, \\ p_1 &= 1.478 \pm 0.077, \\ p_2 &= -1.010 \pm 0.138. \end{aligned} \tag{C3}$$

The fit was performed in ROOT [88], and the extracted parameters and their uncertainties were obtained from the MINUIT minimization package [191]. The band indicates the uncertainty on the fit which was taken as the spread in the g_1^p/F_1^p data, serving as a conservative estimate.

3. A_1^p fit

To obtain A_1^n from our $A_1^{^3\mathrm{He}}$ data, we followed a similar procedure to the g_1/F_1 analysis. The data used in the fit include measurements from SMC [149], HERMES [145],

TABLE XXII. Fit parameters for the positron cross section on ^{3}He, σ^{e^+}, for $E = 4.74$ GeV and $E = 5.89$ GeV.

Par.	$E = 4.74$ GeV	$E = 5.89$ GeV
a_0	$1.887 \times 10^{1} \pm 7.998 \times 10^{-2}$	$1.896 \times 10^{1} \pm 6.899 \times 10^{-2}$
a_1	$-5.620 \times 10^{-3} \pm 1.194 \times 10^{-4}$	$-5.421 \times 10^{-3} \pm 9.286 \times 10^{-5}$

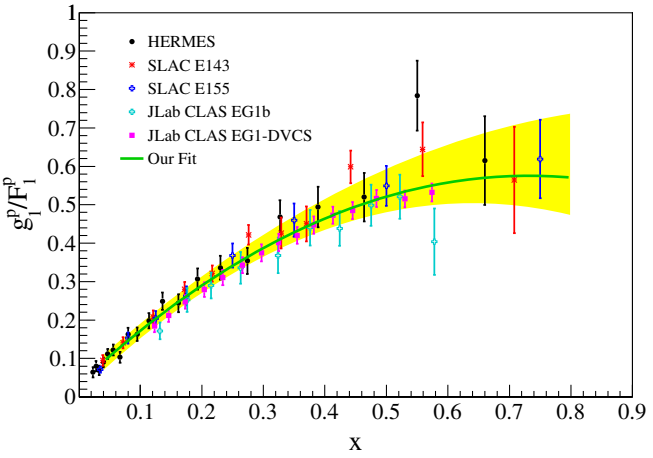

FIG. 42. Our fit to world g_1^p/F_1^p data. The error bars on the data are the in-quadrature sums of their statistical and systematic uncertainties. The band indicates the error on the fit.

EMC [146,147], SLAC E143 [47] and E155 [139], COMPASS [148], and CLAS EG1b [56]. The fit is shown in Fig. 43, where we obtained $\chi^2/\mathrm{ndf} = 1.11$. The fit parameters were found to be

$$\begin{aligned} p_0 &= 0.044 \pm 0.007, \\ p_1 &= 1.423 \pm 0.078, \\ p_2 &= -0.552 \pm 0.158. \end{aligned} \tag{C4}$$

The fit was performed in ROOT [88], and the extracted parameters and their uncertainties were obtained from the MINUIT minimization package [191]. The band in Fig. 43 gives the fit uncertainty, computed in the same fashion as was done for the g_1^p/F_1^p fit.

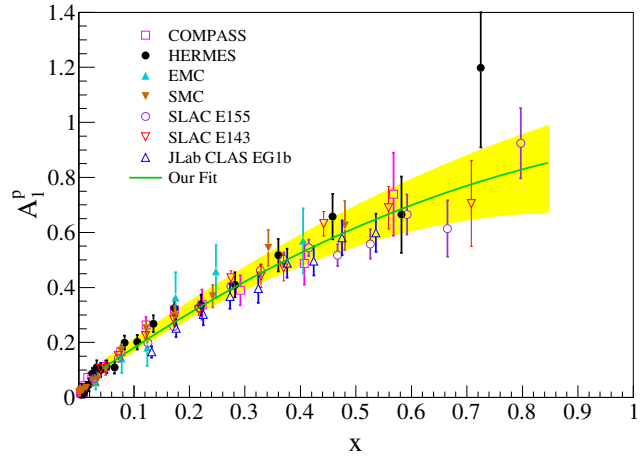

FIG. 43. Our fit to world A_1^p data. The error bars on the data are the in-quadrature sums of their statistical and systematic uncertainties. The band indicates the uncertainty on the fit.

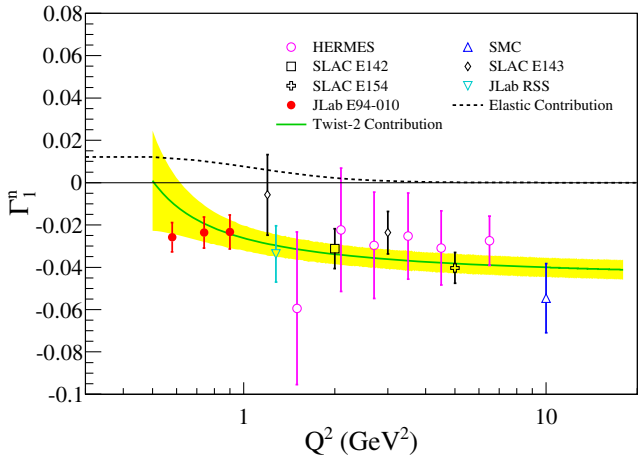

FIG. 44. Γ_1^n for the world data from SLAC E142 [43], E143 [47] and E154 [164], SMC [149], HERMES [163], and JLab RSS [25] and E94-010 [131]. The uncertainties on the world data are the in-quadrature sum of statistical and systematic uncertainties. The elastic contribution is given by the dashed curve and has been added to the data. The twist-2 contribution is indicated by the solid curve, and its uncertainty is given by the band, which is dominated by the uncertainty in α_s.

APPENDIX D: WORLD Γ_1^n DATA

The world Γ_1^n data from SLAC E142 [43], E143 [47] and E154 [164], SMC [149], HERMES [163], and JLab RSS [25] and E94-010 [131] used in our f_2^n analysis are shown in Fig. 44. The twist-2 contribution, μ_2^n, is given by the solid curve; its uncertainty is indicated by the band. The elastic contribution is also shown, given as the dashed curve. For more details, see Sec. V B 3.

Subtracting μ_2^n from Γ_1^n yields the higher-twist contribution, $\Delta\Gamma_1^n \equiv \Gamma_1^n - \mu_2^n$, shown in Fig. 45. Fitting these data to the function

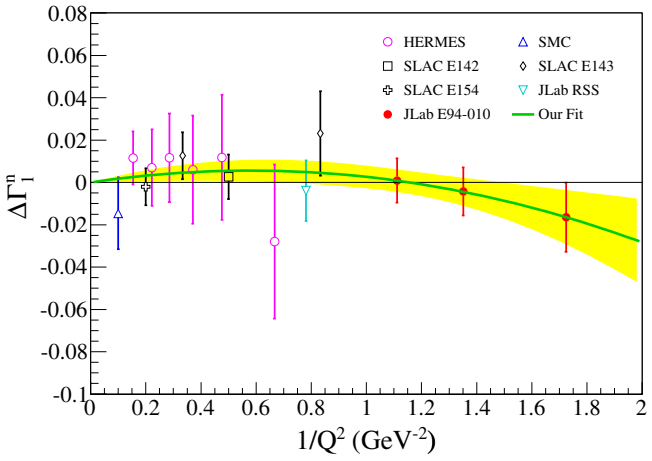

FIG. 45. $\Delta\Gamma_1^n \equiv \Gamma_1^n - \mu_2^n$ for the world data shown in Fig. 44. The uncertainties on the world data are the in-quadrature sum of statistical and systematic uncertainties. Our fit is indicated by the solid curve, and its uncertainty is given by the yellow band.

$$f\left(\frac{1}{Q^2}\right) = \frac{A}{Q^2} + \frac{B}{Q^4}, \tag{D1}$$

where $A = (M_n^2/9)(a_2^n + 4d_2^n + 4f_2^n)$ and $B = \mu_6$, a higher-twist ($\tau > 4$) term, are free parameters. Using the result for the fit parameter A, we extract f_2^n after inserting the average a_2^n from global analyses and our measured d_2^n (see Sec. V B 3) into Eq. (D1). The values of the fit parameters A and B were found to be

$$A = 1.936 \times 10^{-2},$$
$$B = -1.675 \times 10^{-2}, \tag{D2}$$

with the error matrix

$$\varepsilon = \begin{pmatrix} 2.240 \times 10^{-4} & -1.653 \times 10^{-4} \\ -1.653 \times 10^{-4} & 1.351 \times 10^{-4} \end{pmatrix}. \tag{D3}$$

The fit was performed in ROOT [88], and the extracted parameters and their uncertainties were obtained from the MINUIT minimization package [191]. This fit allowed the extraction of f_2^n as described in Sec. V B 3.

APPENDIX E: SYSTEMATIC UNCERTAINTY TABLES

This section contains tables of showing the contributing factors to the systematic uncertainties for the final unpolarized cross sections and double-spin asymmetries, d_2^n, $g_1^{^3\mathrm{He}}$, $g_2^{^3\mathrm{He}}$, $A_1^{^3\mathrm{He}}$, A_1^n, $g_1^{^3\mathrm{He}}/F_1^{^3\mathrm{He}}$, g_1^n/F_1^n and the flavor-separated ratios $(\Delta u + \Delta\bar{u})/(u + \bar{u})$ and $(\Delta d + \Delta\bar{d})/(d + \bar{d})$.

1. Final unpolarized cross section systematic uncertainties

The breakdown of the systematic uncertainty on the unpolarized cross sections is given in Tables XXIII and XXIV. The column "Cuts" indicates uncertainties due to event cuts, which includes the gas Čerenkov, E/p, and target cuts to remove the target windows; "Background" corresponds to uncertainties related to the positron and nitrogen background subtractions; "Misc." refers to the uncertainties incurred from the beam charge calibration, and the density of nitrogen and ^{3}He in the target cell; "RC" is the uncertainty due to the radiative corrections, as explained in Sec. IV B 3. The final column ("Total") gives the in-quadrature sum of all uncertainties in the row.

2. Final asymmetry systematic uncertainties

Tables XXV, XXVI, XXVII, and XXVIII list the systematic uncertainties assigned to the double-spin final asymmetries $A_\parallel$ and $A_\perp$ on ^{3}He. The systematic uncertainty depends on the electron beam polarization P_b, the target polarization P_b, the nitrogen dilution factor D_{N_2}, and contaminations in the BigBite analysis due to π^- (f_1), π^+ (f_2), and e^+ (f_3). Also there are contributions from the electron selection cuts

TABLE XXIII. Systematic uncertainty breakdown for the unpolarized ^{3}He cross section at $E = 4.74$ GeV. All uncertainties are in nb/GeV/sr. See Appendix E 1 for a discussion of the various contributions to the systematic uncertainty.

$\langle x \rangle$	Cuts	Background	Misc.	RC	Total
0.214	1.700×10^{-1}	3.800×10^{-1}	2.440×10^{-1}	2.870×10^{-1}	5.610×10^{-1}
0.299	1.390×10^{-1}	1.170×10^{-1}	2.120×10^{-1}	2.400×10^{-2}	2.810×10^{-1}
0.456	6.400×10^{-2}	1.700×10^{-2}	1.000×10^{-1}	5.000×10^{-3}	1.210×10^{-1}
0.494	5.300×10^{-2}	1.200×10^{-2}	8.800×10^{-2}	1.000×10^{-3}	1.030×10^{-1}
0.533	4.700×10^{-2}	8.000×10^{-3}	7.000×10^{-2}	0.000	8.400×10^{-2}
0.579	3.600×10^{-2}	6.000×10^{-3}	5.300×10^{-2}	2.000×10^{-3}	6.500×10^{-2}
0.629	2.800×10^{-2}	4.000×10^{-3}	4.000×10^{-2}	4.000×10^{-3}	5.000×10^{-2}
0.686	2.000×10^{-2}	3.000×10^{-3}	2.800×10^{-2}	5.000×10^{-3}	3.500×10^{-2}
0.745	1.500×10^{-2}	3.000×10^{-3}	2.100×10^{-2}	9.000×10^{-3}	2.800×10^{-2}

TABLE XXIV. Systematic uncertainty breakdown for the unpolarized ^{3}He cross section at $E = 5.89$ GeV. All uncertainties are in nb/GeV/sr. See Appendix E 1 for a discussion of the various contributions to the systematic uncertainty.

$\langle x \rangle$	Cuts	Background	Misc.	RC	Total
0.208	1.060×10^{-1}	3.710×10^{-1}	1.610×10^{-1}	2.600×10^{-1}	4.920×10^{-1}
0.247	1.120×10^{-1}	2.280×10^{-1}	1.710×10^{-1}	4.700×10^{-2}	3.100×10^{-1}
0.330	5.600×10^{-2}	6.100×10^{-2}	9.800×10^{-2}	1.700×10^{-2}	1.300×10^{-1}
0.434	4.400×10^{-2}	1.700×10^{-2}	6.300×10^{-2}	4.000×10^{-3}	7.900×10^{-2}
0.468	3.800×10^{-2}	1.100×10^{-2}	4.900×10^{-2}	4.000×10^{-3}	6.300×10^{-2}
0.503	2.900×10^{-2}	8.000×10^{-3}	4.200×10^{-2}	1.000×10^{-3}	5.200×10^{-2}
0.539	2.600×10^{-2}	6.000×10^{-3}	3.300×10^{-2}	0.000	4.200×10^{-2}
0.580	1.800×10^{-2}	4.000×10^{-3}	2.700×10^{-2}	1.000×10^{-3}	3.300×10^{-2}
0.629	1.100×10^{-2}	3.000×10^{-3}	1.900×10^{-2}	2.000×10^{-3}	2.200×10^{-2}
0.679	9.000×10^{-3}	2.000×10^{-3}	1.300×10^{-2}	2.000×10^{-3}	1.600×10^{-2}
0.738	7.000×10^{-3}	2.000×10^{-3}	1.000×10^{-2}	4.000×10^{-3}	1.300×10^{-2}

("Cuts") and the radiative corrections ("RC"). The final column ("Total") is the in-quadrature sum of the uncertainties in each row. Columns for all quantities except for the PID cuts have been omitted since they were very small for the lowest x bins and were negligible otherwise.

3. Polarized spin structure function systematic uncertainties

Tables XXIX, XXX, XXXI, and XXXII list the systematic uncertainties assigned to the polarized spin-structure

TABLE XXV. Systematic uncertainties assigned to $A_{\parallel}^{^3\mathrm{He}}$ at an incident beam energy of 4.74 GeV. See Appendix E 2 for a discussion of the various contributions to the systematic uncertainty.

$\langle x \rangle$	Cuts	Total
0.277	7.000×10^{-3}	7.000×10^{-3}
0.325	2.000×10^{-3}	3.000×10^{-3}
0.374	2.000×10^{-3}	2.000×10^{-3}
0.424	4.000×10^{-3}	5.000×10^{-3}
0.473	3.000×10^{-3}	3.000×10^{-3}
0.523	2.000×10^{-3}	2.000×10^{-3}
0.574	4.000×10^{-3}	4.000×10^{-3}
0.623	2.000×10^{-3}	3.000×10^{-3}
0.673	4.000×10^{-3}	5.000×10^{-3}
0.723	6.000×10^{-3}	6.000×10^{-3}
0.773	1.300×10^{-2}	1.300×10^{-2}
0.823	1.100×10^{-2}	1.100×10^{-2}
0.874	1.700×10^{-2}	1.700×10^{-2}

TABLE XXVI. Systematic uncertainties assigned to $A_{\perp}^{^3\mathrm{He}}$ at an incident beam energy of 4.74 GeV. See Appendix E 2 for a discussion of the various contributions to the systematic uncertainty.

$\langle x \rangle$	Cuts	Total
0.277	2.000×10^{-3}	2.000×10^{-3}
0.325	2.000×10^{-3}	2.000×10^{-3}
0.374	2.000×10^{-3}	2.000×10^{-3}
0.424	2.000×10^{-3}	2.000×10^{-3}
0.473	1.000×10^{-3}	1.000×10^{-3}
0.523	1.000×10^{-3}	1.000×10^{-3}
0.574	2.000×10^{-3}	2.000×10^{-3}
0.623	2.000×10^{-3}	2.000×10^{-3}
0.673	3.000×10^{-3}	3.000×10^{-3}
0.723	2.000×10^{-3}	2.000×10^{-3}
0.773	4.000×10^{-3}	5.000×10^{-3}
0.823	6.000×10^{-3}	6.000×10^{-3}
0.874	4.000×10^{-3}	6.000×10^{-3}

TABLE XXVII. Systematic uncertainties assigned to $A_{\parallel}^{^3\mathrm{He}}$ at an incident beam energy of 5.89 GeV See Appendix E 2 for a discussion of the various contributions to the systematic uncertainty.

$\langle x \rangle$	Cuts	Total
0.277	9.000×10^{-3}	1.000×10^{-2}
0.325	3.000×10^{-3}	3.000×10^{-3}
0.374	2.000×10^{-3}	2.000×10^{-3}
0.424	2.000×10^{-3}	3.000×10^{-3}
0.474	6.000×10^{-3}	6.000×10^{-3}
0.524	2.000×10^{-3}	2.000×10^{-3}
0.573	3.000×10^{-3}	3.000×10^{-3}
0.624	5.000×10^{-3}	5.000×10^{-3}
0.674	5.000×10^{-3}	5.000×10^{-3}
0.723	5.000×10^{-3}	5.000×10^{-3}
0.773	8.000×10^{-3}	8.000×10^{-3}
0.823	1.400×10^{-2}	1.400×10^{-2}
0.873	1.700×10^{-2}	1.700×10^{-2}

TABLE XXVIII. Systematic uncertainties assigned to $A_{\perp}^{^3\mathrm{He}}$ at an incident beam energy of 5.89 GeV. See Appendix E 2 for a discussion of the various contributions to the systematic uncertainty.

$\langle x \rangle$	Cuts	Total
0.277	2.000×10^{-3}	3.000×10^{-3}
0.325	1.000×10^{-3}	1.000×10^{-3}
0.374	0.000	0.000
0.424	1.000×10^{-3}	1.000×10^{-3}
0.474	1.000×10^{-3}	1.000×10^{-3}
0.524	1.000×10^{-3}	1.000×10^{-3}
0.573	1.000×10^{-3}	1.000×10^{-3}
0.624	1.000×10^{-3}	1.000×10^{-3}
0.674	2.000×10^{-3}	2.000×10^{-3}
0.723	3.000×10^{-3}	3.000×10^{-3}
0.773	2.000×10^{-3}	2.000×10^{-3}
0.823	3.000×10^{-3}	4.000×10^{-3}
0.873	7.000×10^{-3}	7.000×10^{-3}

TABLE XXIX. Systematic uncertainties assigned to $g_1^{^3\mathrm{He}}$ at an incident beam energy of 4.74 GeV. See Appendix E 3 for a discussion of the various contributions to the systematic uncertainty.

$\langle x \rangle$	Cuts	Total
0.277	8.000×10^{-3}	9.000×10^{-3}
0.325	2.000×10^{-3}	2.000×10^{-3}
0.374	2.000×10^{-3}	2.000×10^{-3}
0.424	3.000×10^{-3}	3.000×10^{-3}
0.473	1.000×10^{-3}	2.000×10^{-3}
0.523	0.000	0.000
0.574	1.000×10^{-3}	1.000×10^{-3}
0.623	0.000	1.000×10^{-3}
0.673	1.000×10^{-3}	1.000×10^{-3}
0.723	0.000	1.000×10^{-3}
0.773	1.000×10^{-3}	1.000×10^{-3}
0.823	1.000×10^{-3}	1.000×10^{-3}
0.874	0.000	1.000×10^{-3}

TABLE XXX. Systematic uncertainties assigned to $g_2^{^3\mathrm{He}}$ at an incident beam energy of 4.74 GeV. See Appendix E 3 for a discussion of the various contributions to the systematic uncertainty.

$\langle x \rangle$	Cuts	Total
0.277	9.000×10^{-3}	9.000×10^{-3}
0.325	6.000×10^{-3}	6.000×10^{-3}
0.374	4.000×10^{-3}	5.000×10^{-3}
0.424	2.000×10^{-3}	2.000×10^{-3}
0.473	0.000	1.000×10^{-3}
0.523	1.000×10^{-3}	1.000×10^{-3}
0.574	1.000×10^{-3}	1.000×10^{-3}
0.623	1.000×10^{-3}	1.000×10^{-3}
0.673	1.000×10^{-3}	1.000×10^{-3}
0.723	0.000	1.000×10^{-3}
0.773	0.000	1.000×10^{-3}
0.823	0.000	0.000
0.874	0.000	1.000×10^{-3}

TABLE XXXI. Systematic uncertainties assigned to $g_1^{^3\mathrm{He}}$ at an incident beam energy of 5.89 GeV. See Appendix E 3 for a discussion of the various contributions to the systematic uncertainty.

$\langle x \rangle$	Cuts	Total
0.277	1.000×10^{-2}	1.200×10^{-2}
0.325	2.000×10^{-3}	3.000×10^{-3}
0.374	2.000×10^{-3}	2.000×10^{-3}
0.424	1.000×10^{-3}	2.000×10^{-3}
0.474	2.000×10^{-3}	2.000×10^{-3}
0.524	1.000×10^{-3}	1.000×10^{-3}
0.573	1.000×10^{-3}	1.000×10^{-3}
0.624	1.000×10^{-3}	1.000×10^{-3}
0.674	0.000	0.000
0.723	0.000	0.000
0.773	0.000	0.000
0.823	0.000	0.000
0.873	0.000	0.000

TABLE XXXII. Systematic uncertainties assigned to $g_2^{^3\mathrm{He}}$ at an incident beam energy of 5.89 GeV. See Appendix E 3 for a discussion of the various contributions to the systematic uncertainty.

$\langle x \rangle$	Cuts	Total
0.277	1.400×10^{-2}	1.900×10^{-2}
0.325	5.000×10^{-3}	6.000×10^{-3}
0.374	1.000×10^{-3}	2.000×10^{-3}
0.424	2.000×10^{-3}	2.000×10^{-3}
0.474	2.000×10^{-3}	2.000×10^{-3}
0.524	1.000×10^{-3}	1.000×10^{-3}
0.573	1.000×10^{-3}	1.000×10^{-3}
0.624	0.000	0.000
0.674	0.000	0.000
0.723	0.000	0.000
0.773	0.000	0.000
0.823	0.000	1.000×10^{-3}
0.873	0.000	0.000

TABLE XXXIII. Systematic uncertainties assigned to different regions of d_2^n. "Res" indicates the contribution from the resonance region, in particular, from data with $W < 2$ GeV. "DIS" represents the contribution due to data for $W > 2$ GeV. See Appendix E 4 for a discussion of the various contributions to the systematic uncertainty.

Region	$\langle Q^2 \rangle$ [GeV^2]	Exp.	RC	d_2^p	$\tilde{P}_p$, $\tilde{P}_n$ (high error)	$\tilde{P}_p$, $\tilde{P}_n$ (low error)	Low x	Total
DIS+Res	3.21	4.700×10^{-4}	2.000×10^{-5}	4.000×10^{-5}	6.000×10^{-5}	1.000×10^{-4}	5.800×10^{-4}	7.500×10^{-4}
DIS+Res	4.32	3.700×10^{-4}	2.000×10^{-5}	4.000×10^{-5}	2.000×10^{-5}	4.000×10^{-5}	5.800×10^{-4}	6.900×10^{-4}
DIS	2.59	3.600×10^{-4}	1.000×10^{-5}	5.000×10^{-5}	3.000×10^{-5}	5.000×10^{-5}	⋯	3.700×10^{-4}
DIS	3.67	2.900×10^{-4}	2.000×10^{-5}	4.000×10^{-5}	2.000×10^{-5}	2.000×10^{-5}	⋯	2.900×10^{-4}
Res	4.71	2.200×10^{-4}	0.000	4.000×10^{-5}	3.000×10^{-5}	5.000×10^{-5}	⋯	2.300×10^{-4}
Res	5.99	1.100×10^{-4}	0.000	2.000×10^{-5}	1.000×10^{-5}	3.000×10^{-5}	⋯	1.200×10^{-4}

functions. A number of factors contribute to the systematic uncertainty, including kinematics ("Kin.") and all of the systematic uncertainties found to contribute to the final asymmetries, namely P_b, P_t, f_1, f_2 f_3, PID cuts ("Cuts"), and radiative corrections ("RC"). Other contributions include the systematic uncertainty on the unpolarized cross section (σ_0), in addition to the uncertainties associated with the interpolation or extrapolation of the data where necessary. The value for each of these uncertainties was determined by varying each of these contributions within reasonable limits and taking the corresponding change in the observable (either $g_1^{^3\mathrm{He}}$ or $g_2^{^3\mathrm{He}}$) as the uncertainty. The last column ("Total") is the in-quadrature sum of the uncertainties in each row. All uncertainties are absolute. Columns for all quantities except for the PID cuts have been omitted since they were very small for the lowest x bins and were negligible otherwise.

4. d_2^n systematic uncertainties

A breakdown of the d_2^n systematic uncertainties is given in Table XXXIII, for each of the measured mean Q^2 points. This table includes the effects of all the uncertainties found in the preceding tables (i.e., P_p, P_t, etc.), referred to as experimental systematics ("Exp."), in addition to radiative corrections, d_2^p, the proton and neutron polarizations ($\tilde{P}_p$ and $\tilde{P}_n$), and the unmeasured low x contributions. The value for each of these uncertainties was determined by varying each of these contributions within reasonable limits and taking the corresponding change in d_2^n as the uncertainty. The two sources of uncertainty that dominate the d_2^n systematic uncertainty are those from the experimental and low-x contributions. However, the final d_2^n measurement's statistical uncertainty is larger than its systematic uncertainty.

TABLE XXXIV. The systematic uncertainties contributing to the $a_2^{^3\mathrm{He}}$ result in the measured x range. See Appendix E 5 for a discussion of the various contributions to the systematic uncertainty.

$\langle Q^2 \rangle$ [GeV^2]	$g_1^{^3\mathrm{He}}$	x	Total
3.21	3.428×10^{-5}	8.803×10^{-6}	3.539×10^{-5}
4.32	3.281×10^{-5}	6.681×10^{-6}	3.348×10^{-5}

5. a_2 systematic uncertainties

The systematic uncertainties for the measured $a_2^{^3\mathrm{He}}$ are given in Table XXXIV, where the column labeled $g_1^{^3\mathrm{He}}$ corresponds to the uncertainty due to our $g_1^{^3\mathrm{He}}$ data, and the column labeled x is the uncertainty due to x in the integration. The value of these uncertainties was determined by varying each of these contributions within reasonable limits and taking the change in $a_2^{^3\mathrm{He}}$ as the uncertainty. The in-quadrature sum of the two contributions is given as the column labeled "Total." The systematic uncertainties for the a_2^n extraction for the full x range are presented in Table XXXV. The columns labeled Low x (High x) correspond to the uncertainties due to the low-x (high-x) regions. The uncertainty due to the effective proton (neutron) polarization is given by the column labeled $\tilde{P}_p$ ($\tilde{P}_n$). The uncertainties due to a_2^p and our measured $a_2^{^3\mathrm{He}}$ are also given.

6. A_1 and g_1/F_1 systematic uncertainties

This section discusses the breakdown of the systematic uncertainties on $A_1^{^3\mathrm{He}}$ and A_1^n. The main factors that contribute to the uncertainties on the ^{3}He data are the final

TABLE XXXV. The systematic uncertainties contributing to the a_2^n result over the full x range. See Appendix E 5 for a discussion of the various contributions to the systematic uncertainty listed below.

$\langle Q^2 \rangle$ [GeV^2]	Low x	High x	$\tilde{P}_p$	$\tilde{P}_n$	a_2^p	$a_2^{^3\mathrm{He}}$	Total
3.21	1.374×10^{-4}	1.373×10^{-4}	2.439×10^{-4}	3.012×10^{-4}	3.068×10^{-4}	3.052×10^{-4}	6.125×10^{-4}
4.32	8.878×10^{-5}	8.880×10^{-5}	2.518×10^{-4}	3.054×10^{-4}	3.118×10^{-4}	3.089×10^{-4}	6.042×10^{-4}

TABLE XXXVI. Systematic uncertainties for $A_1^{^3\mathrm{He}}$ data at $E = 4.74$ GeV. See Appendix E 6 for a discussion of the various contributions to the systematic uncertainty.

$\langle x \rangle$	$A_\parallel$	$A_\perp$	Kin.	Total
0.277	3.850×10^{-3}	1.900×10^{-4}	1.200×10^{-4}	3.860×10^{-3}
0.325	1.480×10^{-3}	1.400×10^{-4}	7.000×10^{-5}	1.480×10^{-3}
0.374	9.900×10^{-4}	2.100×10^{-4}	5.400×10^{-4}	1.150×10^{-3}
0.424	2.650×10^{-3}	1.700×10^{-4}	1.200×10^{-4}	2.660×10^{-3}
0.473	1.840×10^{-3}	1.100×10^{-4}	1.900×10^{-4}	1.850×10^{-3}
0.523	1.100×10^{-3}	1.600×10^{-4}	1.900×10^{-4}	1.130×10^{-3}
0.574	2.430×10^{-3}	3.300×10^{-4}	2.000×10^{-4}	2.460×10^{-3}
0.623	1.840×10^{-3}	3.600×10^{-4}	1.400×10^{-4}	1.880×10^{-3}
0.673	2.620×10^{-3}	5.000×10^{-4}	1.300×10^{-4}	2.670×10^{-3}
0.723	3.770×10^{-3}	4.400×10^{-4}	2.000×10^{-4}	3.800×10^{-3}
0.773	7.510×10^{-3}	8.900×10^{-4}	3.900×10^{-4}	7.570×10^{-3}
0.823	7.000×10^{-3}	1.180×10^{-3}	3.200×10^{-4}	7.100×10^{-3}
0.874	1.019×10^{-2}	1.250×10^{-3}	1.960×10^{-3}	1.045×10^{-2}

TABLE XXXVII. Systematic uncertainties for $A_1^{^3\mathrm{He}}$ data at $E = 5.89$ GeV. See Appendix E 6 for a discussion of the various contributions to the systematic uncertainty.

$\langle x \rangle$	$A_\parallel$	$A_\perp$	Kin.	Total
0.277	5.520×10^{-3}	1.800×10^{-4}	5.900×10^{-4}	5.550×10^{-3}
0.325	1.850×10^{-3}	9.000×10^{-5}	2.400×10^{-4}	1.870×10^{-3}
0.374	1.230×10^{-3}	4.000×10^{-5}	4.000×10^{-5}	1.230×10^{-3}
0.424	1.510×10^{-3}	1.100×10^{-4}	2.200×10^{-4}	1.530×10^{-3}
0.474	3.270×10^{-3}	9.000×10^{-5}	4.000×10^{-5}	3.270×10^{-3}
0.524	1.200×10^{-3}	1.200×10^{-4}	1.000×10^{-5}	1.210×10^{-3}
0.573	1.800×10^{-3}	1.400×10^{-4}	1.300×10^{-4}	1.810×10^{-3}
0.624	3.120×10^{-3}	1.000×10^{-4}	1.600×10^{-4}	3.130×10^{-3}
0.674	2.770×10^{-3}	2.700×10^{-4}	7.000×10^{-5}	2.780×10^{-3}
0.723	2.740×10^{-3}	3.900×10^{-4}	1.300×10^{-4}	2.770×10^{-3}
0.773	4.430×10^{-3}	3.500×10^{-4}	1.100×10^{-4}	4.450×10^{-3}
0.823	7.870×10^{-3}	7.100×10^{-4}	6.600×10^{-4}	7.930×10^{-3}
0.873	9.270×10^{-3}	1.170×10^{-3}	1.400×10^{-4}	9.340×10^{-3}

asymmetries $A_\parallel$ and $A_\perp$, and the kinematic factors D, η, ξ, and d (see Sec. I C). Each final asymmetry was varied within its uncertainty, and the change in $A_1^{^3\mathrm{He}}$ was observed. For the kinematics, the low-level variables of the electron momentum p and scattering angle θ were changed within their relative uncertainties of 1% and 1.4% [86], respectively, and the kinematic factors were reevaluated, and the change in the A_1 asymmetry was observed. The resulting contributions to the systematic uncertainty in $A_1^{^3\mathrm{He}}$ are listed in Tables XXXVI and XXXVII for the 4.74 GeV and 5.89 GeV runs, respectively.

The systematic uncertainties for A_1^n are listed in Tables XXXVIII and XXXIX. The inputs in the A_1^n extraction that were varied consisted of F_2^n and F_2^p, $F_2^{^3\mathrm{He}}$, A_1^p, and our $A_1^{^3\mathrm{He}}$ data. For the neutron and proton F_2, various models [134,143,192] were compared, and the largest difference in A_1^n was taken as the uncertainty, listed in the $F_2^{n,p}$ column. The same procedure was used for $F_2^{^3\mathrm{He}}$,

TABLE XXXVIII. Systematic uncertainties for A_1^n at $E = 4.74$ GeV. See Appendix E 6 for a discussion of the various contributions to the systematic uncertainty.

$\langle x \rangle$	$F_2^{n,p}$	$F_2^{^3\mathrm{He}}$	$\tilde{P}_p$	$\tilde{P}_n$	A_1^p	$A_1^{^3\mathrm{He}}$	Total
0.277	2.730×10^{-3}	7.000×10^{-4}	5.160×10^{-3}	1.500×10^{-4}	5.080×10^{-3}	2.680×10^{-3}	8.220×10^{-3}
0.325	2.690×10^{-3}	1.010×10^{-3}	6.160×10^{-3}	1.200×10^{-4}	6.050×10^{-3}	1.850×10^{-3}	9.280×10^{-3}
0.374	6.900×10^{-3}	6.500×10^{-4}	7.200×10^{-3}	1.690×10^{-3}	6.690×10^{-3}	6.370×10^{-3}	1.371×10^{-2}
0.424	5.980×10^{-3}	1.810×10^{-3}	8.310×10^{-3}	1.190×10^{-3}	7.710×10^{-3}	6.390×10^{-3}	1.449×10^{-2}
0.473	5.740×10^{-3}	1.710×10^{-3}	9.570×10^{-3}	8.500×10^{-4}	8.960×10^{-3}	5.280×10^{-3}	1.537×10^{-2}

TABLE XXXIX. Systematic uncertainties for A_1^n at $E = 5.89$ GeV. See Appendix E 6 for a discussion of the various contributions to the systematic uncertainty.

$\langle x \rangle$	$F_2^{n,p}$	$F_2^{^3\mathrm{He}}$	$\tilde{P}_p$	$\tilde{P}_n$	A_1^p	$A_1^{^3\mathrm{He}}$	Total
0.277	4.500×10^{-3}	4.000×10^{-4}	5.140×10^{-3}	2.070×10^{-3}	5.130×10^{-3}	3.370×10^{-2}	3.483×10^{-2}
0.325	2.440×10^{-3}	1.310×10^{-3}	6.140×10^{-3}	5.900×10^{-4}	5.810×10^{-3}	3.060×10^{-3}	9.430×10^{-3}
0.374	2.650×10^{-3}	6.400×10^{-4}	7.190×10^{-3}	5.200×10^{-4}	6.700×10^{-3}	1.470×10^{-3}	1.032×10^{-2}
0.424	2.900×10^{-3}	2.120×10^{-3}	8.300×10^{-3}	7.400×10^{-4}	7.940×10^{-3}	3.740×10^{-3}	1.263×10^{-2}
0.474	3.940×10^{-3}	1.350×10^{-3}	9.560×10^{-3}	8.400×10^{-4}	9.240×10^{-3}	9.750×10^{-3}	1.702×10^{-2}
0.524	9.950×10^{-3}	0.000	1.096×10^{-2}	1.720×10^{-3}	1.060×10^{-2}	5.050×10^{-3}	1.897×10^{-2}
0.573	1.300×10^{-2}	1.500×10^{-4}	1.247×10^{-2}	2.140×10^{-3}	1.207×10^{-2}	8.000×10^{-3}	2.321×10^{-2}

TABLE XL. Systematic uncertainties for $g_1^{^3\mathrm{He}}/F_1^{^3\mathrm{He}}$ data at $E = 4.74$ GeV. See Appendix E 6 for a discussion of the various contributions to the systematic uncertainty.

$\langle x \rangle$	$A_\parallel$	$A_\perp$	Kin.	Total
0.277	3.680×10^{-3}	5.300×10^{-4}	4.000×10^{-5}	3.720×10^{-3}
0.325	1.340×10^{-3}	3.500×10^{-4}	4.000×10^{-5}	1.380×10^{-3}
0.374	9.200×10^{-4}	4.900×10^{-4}	4.000×10^{-5}	1.040×10^{-3}
0.424	2.560×10^{-3}	3.300×10^{-4}	1.300×10^{-4}	2.580×10^{-3}
0.473	1.710×10^{-3}	2.000×10^{-4}	1.100×10^{-4}	1.720×10^{-3}
0.523	1.030×10^{-3}	2.600×10^{-4}	2.000×10^{-5}	1.060×10^{-3}
0.574	2.200×10^{-3}	4.700×10^{-4}	3.000×10^{-5}	2.260×10^{-3}
0.623	1.610×10^{-3}	5.000×10^{-4}	1.700×10^{-4}	1.690×10^{-3}
0.673	2.430×10^{-3}	6.700×10^{-4}	1.400×10^{-4}	2.530×10^{-3}
0.723	3.350×10^{-3}	5.100×10^{-4}	2.000×10^{-4}	3.390×10^{-3}
0.773	6.410×10^{-3}	9.700×10^{-4}	1.600×10^{-4}	6.490×10^{-3}
0.823	5.760×10^{-3}	1.260×10^{-3}	2.800×10^{-4}	5.900×10^{-3}
0.874	8.590×10^{-3}	1.230×10^{-3}	3.200×10^{-4}	8.680×10^{-3}

where the models considered were F1F209 [122] and NMC95 [193]. This uncertainty is given in the $F_2^{^3\mathrm{He}}$ column. Our fit of the world A_1^p data was varied within its uncertainty, and the change in A_1^n was taken as the uncertainty, listed in the A_1^p column. The values for the effective neutron (proton) polarization $\tilde{P}_n$ ($\tilde{P}_p$) were varied within their uncertainties, and the change in A_1^n was taken as the uncertainty. These contributions are listed as $\tilde{P}_n$ and $\tilde{P}_p$ for the neutron and proton, respectively. We varied our $A_1^{^3\mathrm{He}}$ data within their systematic uncertainties and observed the changes in the A_1^n results, which were taken as the uncertainties, listed in the $A_1^{^3\mathrm{He}}$ column. The in-quadrature sum of all contributions is given in the column labeled "Total."

TABLE XLI. Systematic uncertainties for $g_1^{^3\mathrm{He}}/F_1^{^3\mathrm{He}}$ data at $E = 5.89$ GeV. See Appendix E 6 for a discussion of the various contributions to the systematic uncertainty.

$\langle x \rangle$	$A_\parallel$	$A_\perp$	Kin.	Total
0.277	5.320×10^{-3}	2.570×10^{-3}	5.000×10^{-5}	5.910×10^{-3}
0.325	1.720×10^{-3}	1.070×10^{-3}	4.000×10^{-5}	2.030×10^{-3}
0.374	1.170×10^{-3}	1.900×10^{-4}	1.000×10^{-5}	1.190×10^{-3}
0.424	1.350×10^{-3}	9.500×10^{-4}	4.000×10^{-5}	1.650×10^{-3}
0.474	3.160×10^{-3}	1.100×10^{-4}	5.000×10^{-5}	3.160×10^{-3}
0.524	1.200×10^{-3}	1.100×10^{-4}	0.000	1.200×10^{-3}
0.573	1.640×10^{-3}	6.800×10^{-4}	1.000×10^{-5}	1.780×10^{-3}
0.624	2.720×10^{-3}	9.100×10^{-4}	2.000×10^{-5}	2.870×10^{-3}
0.674	2.420×10^{-3}	4.400×10^{-4}	1.000×10^{-5}	2.460×10^{-3}
0.723	2.370×10^{-3}	1.070×10^{-3}	2.000×10^{-5}	2.600×10^{-3}
0.773	3.900×10^{-3}	1.120×10^{-3}	4.000×10^{-5}	4.060×10^{-3}
0.823	7.090×10^{-3}	1.068×10^{-2}	1.800×10^{-4}	1.282×10^{-2}
0.873	8.480×10^{-3}	2.030×10^{-3}	1.000×10^{-4}	8.720×10^{-3}

TABLE XLII. Systematic uncertainties for g_1^n/F_1^n at $E = 4.74$ GeV. See Appendix E 6 for a discussion of the various contributions to the systematic uncertainty.

$\langle x \rangle$	$F_2^{n,p}$	$F_2^{^3\mathrm{He}}$	$\tilde{P}_p$	$\tilde{P}_n$	g_1^p/F_1^p	$g_1^{^3\mathrm{He}}/F_1^{^3\mathrm{He}}$	Total
0.277	2.530×10^{-3}	7.100×10^{-4}	5.320×10^{-3}	1.200×10^{-4}	2.950×10^{-3}	7.630×10^{-3}	1.011×10^{-2}
0.325	2.480×10^{-3}	9.800×10^{-4}	6.270×10^{-3}	1.300×10^{-4}	3.650×10^{-3}	3.060×10^{-3}	8.310×10^{-3}
0.374	5.640×10^{-3}	2.900×10^{-4}	7.230×10^{-3}	1.080×10^{-3}	4.680×10^{-3}	2.470×10^{-3}	1.064×10^{-2}
0.424	5.770×10^{-3}	1.730×10^{-3}	8.190×10^{-3}	1.100×10^{-3}	6.020×10^{-3}	6.360×10^{-3}	1.346×10^{-2}
0.473	6.020×10^{-3}	1.700×10^{-3}	9.240×10^{-3}	9.700×10^{-4}	7.600×10^{-3}	5.050×10^{-3}	1.445×10^{-2}

TABLE XLIII. Systematic uncertainties for g_1^n/F_1^n at $E = 5.89$ GeV. See Appendix E 6 for a discussion of the various contributions to the systematic uncertainty.

$\langle x \rangle$	$F_2^{n,p}$	$F_2^{^3\mathrm{He}}$	$\tilde{P}_p$	$\tilde{P}_n$	g_1^p/F_1^p	$g_1^{^3\mathrm{He}}/F_1^{^3\mathrm{He}}$	Total
0.277	4.500×10^{-3}	4.500×10^{-4}	5.100×10^{-3}	2.450×10^{-3}	2.970×10^{-3}	1.193×10^{-2}	1.427×10^{-2}
0.325	2.180×10^{-3}	1.160×10^{-3}	6.030×10^{-3}	3.300×10^{-4}	3.760×10^{-3}	4.510×10^{-3}	8.780×10^{-3}
0.374	2.420×10^{-3}	6.200×10^{-4}	6.950×10^{-3}	5.300×10^{-4}	4.790×10^{-3}	2.920×10^{-3}	9.290×10^{-3}
0.424	3.110×10^{-3}	2.110×10^{-3}	7.890×10^{-3}	8.400×10^{-4}	6.020×10^{-3}	4.410×10^{-3}	1.152×10^{-2}
0.474	3.770×10^{-3}	1.260×10^{-3}	8.900×10^{-3}	7.600×10^{-4}	7.280×10^{-3}	9.170×10^{-3}	1.525×10^{-2}
0.524	9.150×10^{-3}	0.000	9.980×10^{-3}	1.680×10^{-3}	9.620×10^{-3}	3.940×10^{-3}	1.716×10^{-2}
0.573	1.240×10^{-2}	1.500×10^{-4}	1.111×10^{-2}	2.280×10^{-3}	1.183×10^{-2}	7.140×10^{-3}	2.176×10^{-2}

TABLE XLIV. Systematic uncertainties for $(\Delta u + \Delta\bar{u})/(u + \bar{u})$ at $E = 4.74$ GeV. See Appendix E 7 for a discussion of the various contributions to the systematic uncertainty.

$\langle x \rangle$	g_1^n/F_1^n	g_1^p/F_1^p	$(d + \bar{d})/(u + \bar{u})$	s	Total
0.277	9.900×10^{-4}	2.918×10^{-2}	3.260×10^{-3}	8.700×10^{-3}	3.064×10^{-2}
0.325	7.800×10^{-4}	3.556×10^{-2}	3.590×10^{-3}	6.450×10^{-3}	3.633×10^{-2}
0.374	9.300×10^{-4}	4.243×10^{-2}	3.610×10^{-3}	4.580×10^{-3}	4.284×10^{-2}
0.424	1.090×10^{-3}	4.967×10^{-2}	4.620×10^{-3}	3.280×10^{-3}	5.000×10^{-2}
0.473	1.100×10^{-3}	6.300×10^{-2}	5.070×10^{-3}	2.350×10^{-3}	6.326×10^{-2}

To evaluate the systematic uncertainties on g_1/F_1 data, shown in Tables XL, XLI, XLII, and XLIII, the same procedure used for the A_1 data was applied. The same models for F_2 on the neutron, proton, and ^{3}He were used, in addition to the effective polarizations of the neutron and proton, $\tilde{P}_n$ and $\tilde{P}_p$.

7. Flavor decomposition systematic uncertainties

Tables XLIV and XLV give a breakdown of the systematic uncertainties at $E = 4.74$ GeV for the up- and down-quark ratios, respectively. Tables XLVI and XLVII list the uncertainties for $E = 5.89$ GeV. The columns of the table represent the contribution due to our g_1^n/F_1^n data, our fit to world g_1^p/F_1^p data, the $(d + \bar{d})/(u + \bar{u})$ parametrization, and the strange uncertainty, respectively. The value of these uncertainties, except for the strange uncertainty (see Sec. V C), was determined by varying each of these contributions within reasonable limits and taking the change in the quark ratio as the uncertainty. This was done for both the up- and down-quark ratios. The in-quadrature sum of all contributions is displayed in the last column, labeled "Total."

TABLE XLV. Systematic uncertainties for $(\Delta d + \Delta\bar{d})/(d + \bar{d})$ at $E = 4.74$ GeV. See Appendix E 7 for a discussion of the various contributions to the systematic uncertainty.

$\langle x \rangle$	g_1^n/F_1^n	g_1^p/F_1^p	$(d + \bar{d})/(u + \bar{u})$	s	Total
0.277	8.240×10^{-3}	1.518×10^{-2}	1.455×10^{-2}	1.673×10^{-2}	2.811×10^{-2}
0.325	7.140×10^{-3}	2.027×10^{-2}	1.886×10^{-2}	1.363×10^{-2}	3.167×10^{-2}
0.374	9.290×10^{-3}	2.647×10^{-2}	2.280×10^{-2}	1.071×10^{-2}	3.770×10^{-2}
0.424	1.193×10^{-2}	3.399×10^{-2}	3.467×10^{-2}	8.140×10^{-3}	5.066×10^{-2}
0.473	1.343×10^{-2}	4.814×10^{-2}	4.754×10^{-2}	5.940×10^{-3}	6.923×10^{-2}

TABLE XLVI. Systematic uncertainties for $(\Delta u + \Delta\bar{u})/(u + \bar{u})$ at $E = 5.89$ GeV. See Appendix E 7 for a discussion of the various contributions to the systematic uncertainty.

$\langle x \rangle$	g_1^n/F_1^n	g_1^p/F_1^p	$(d + \bar{d})/(u + \bar{u})$	s	Total
0.277	1.380×10^{-3}	3.088×10^{-2}	1.980×10^{-3}	8.300×10^{-3}	3.207×10^{-2}
0.325	8.100×10^{-4}	3.675×10^{-2}	3.750×10^{-3}	6.190×10^{-3}	3.746×10^{-2}
0.374	7.800×10^{-4}	4.430×10^{-2}	3.800×10^{-3}	4.390×10^{-3}	4.469×10^{-2}
0.424	9.400×10^{-4}	5.109×10^{-2}	4.460×10^{-3}	3.110×10^{-3}	5.139×10^{-2}
0.474	1.160×10^{-3}	6.267×10^{-2}	4.810×10^{-3}	2.220×10^{-3}	6.290×10^{-2}
0.524	1.220×10^{-3}	6.976×10^{-2}	4.130×10^{-3}	1.600×10^{-3}	6.991×10^{-2}
0.573	1.430×10^{-3}	8.454×10^{-2}	3.860×10^{-3}	1.240×10^{-3}	8.465×10^{-2}

TABLE XLVII. Systematic uncertainties for $(\Delta d + \Delta\bar{d})/(d + \bar{d})$ at $E = 5.89$ GeV. See Appendix E 7 for a discussion of the various contributions to the systematic uncertainty.

$\langle x \rangle$	g_1^n/F_1^n	g_1^p/F_1^p	$(d + \bar{d})/(u + \bar{u})$	s	Total
0.277	1.158×10^{-2}	1.622×10^{-2}	8.640×10^{-3}	1.631×10^{-2}	2.716×10^{-2}
0.325	7.470×10^{-3}	2.116×10^{-2}	1.973×10^{-2}	1.339×10^{-2}	3.274×10^{-2}
0.374	7.850×10^{-3}	2.792×10^{-2}	2.503×10^{-2}	1.036×10^{-2}	3.969×10^{-2}
0.424	1.039×10^{-2}	3.539×10^{-2}	3.438×10^{-2}	7.810×10^{-3}	5.102×10^{-2}
0.474	1.436×10^{-2}	4.863×10^{-2}	4.929×10^{-2}	5.660×10^{-3}	7.094×10^{-2}
0.524	1.731×10^{-2}	6.181×10^{-2}	5.298×10^{-2}	3.580×10^{-3}	8.331×10^{-2}
0.573	2.341×10^{-2}	8.633×10^{-2}	6.641×10^{-2}	2.130×10^{-3}	1.114×10^{-1}

[1] R. W. Mcallister and R. Hofstadter, Phys. Rev. **102**, 851 (1956).

[2] E. D. Bloom, D. H. Coward, H. DeStaebler, J. Drees, G. Miller, L. W. Mo, R. E. Taylor, M. Breidenbach, J. I. Friedman, G. C. Hartmann, and H. W. Kendall, Phys. Rev. Lett. **23**, 930 (1969); M. Breidenbach, J. I. Friedman, H. W. Kendall, E. D. Bloom, D. H. Coward, H. DeStaebler, J. Drees, L. W. Mo, and R. E. Taylor, Phys. Rev. Lett. **23**, 935 (1969).

[3] D. J. Gross and F. Wilczek, Phys. Rev. Lett. **30**, 1343 (1973); D. Gross and F. Wilczek, Phys. Rev. D **8**, 3633 (1973); **9**, 980 (1974).

[4] S. Kuhn, J.-P. Chen, and E. Leader, Prog. Part. Nucl. Phys. **63**, 1 (2009).

[5] C. A. Aidala, S. D. Bass, D. Hasch, and G. K. Mallot, Rev. Mod. Phys. **85**, 655 (2013).

[6] A. Adare *et al.* (PHENIX Collaboration), Phys. Rev. D **90**, 012007 (2014).

[7] L. Adamczyk *et al.* (STAR Collaboration), Phys. Rev. Lett. **115**, 092002 (2015).

[8] E. V. Shuryak and A. I. Vainshtein, Nucl. Phys. **B201**, 141 (1982); R. Jaffe, Comments Nucl. Part. Phys. **19**, 239 (1990); R. L. Jaffe and X.-D. Ji, Phys. Rev. D **43**, 724 (1991).

[9] Y. L. Dokshitzer, Sov. Phys. JETP **46**, 641 (1977); V. Gribov and L. Lipatov, Sov. J. Nucl. Phys. **15**, 438 (1972); G. Altarelli and G. Parisi, Nucl. Phys. **B126**, 298 (1977).

[10] J. D. Bjorken, Phys. Rev. **148**, 1467 (1966); Phys. Rev. D **1**, 1376 (1970).

[11] A. V. Manohar, in *Symmetry and Spin in the Standard Model: Proceedings of the Seventh Lake Louise Winter Institute: Chateau Lake Louise, 1992* (World Scientific, Singapore, 1992).

[12] J. L. Cortes, B. Pire, and J. Ralston, Z. Phys. C **55**, 409 (1992).

[13] B. W. Filippone and X.-D. Ji, Adv. Nucl. Phys. **26**, 1 (2001).

[14] S. Wandzura and F. Wilczek, Phys. Lett. B **72B**, 195 (1977).

[15] K. G. Wilson, Phys. Rev. **179**, 1499 (1969).

[16] B. Ehrnsperger, A. Schäfer, and L. Mankiewicz, Phys. Lett. B **323**, 439 (1994).

[17] M. Burkardt, Phys. Rev. D **88**, 114502 (2013).

[18] E. V. Shuryak and A. I. Vainshtein, Nucl. Phys. **B199**, 451 (1982).

[19] J. Edelmann, G. Piller, N. Kaiser, and W. Weise, Nucl. Phys. **A665**, 125 (2000).

[20] M. Osipenko, W. Melnitchouk, S. Simula, P. E. Bosted, V. Burkert, M. E. Christy, K. Griffioen, C. Keppel, and S. E. Kuhn, Phys. Lett. B **609**, 259 (2005).

[21] S. Larin, T. van Ritbergen, and J. Vermaseren, Phys. Lett. B **404**, 153 (1997).

[22] Z.-E. Meziani *et al.*, Phys. Lett. B **613**, 148 (2005).

[23] In this paper, natural units are used.

[24] M. Amarian *et al.* (Jefferson Lab E94-010 Collaboration), Phys. Rev. Lett. **92**, 022301 (2004).

[25] K. Slifer *et al.* (Resonance Spin Structure Collaboration), Phys. Rev. Lett. **105**, 101601 (2010).
[26] P. Solvignon *et al.* (E01-012 Collaboration), Phys. Rev. C **92**, 015208 (2015).
[27] P. Anthony *et al.* (E155 Collaboration), Phys. Lett. B **553**, 18 (2003).
[28] X. Zheng *et al.* (Jefferson Lab Hall A Collaboration), Phys. Rev. C **70**, 065207 (2004).
[29] D. Drechsel, S. Kamalov, and L. Tiator, Eur. Phys. J. A **34**, 69 (2007).
[30] E. Stein, P Górnicki, L Mankiewicz, A Schäfer, and W Greiner, Phys. Lett. B **343**, 369 (1995).
[31] I. Balitsky, V. M. Braun, and A. Kolesnichenko, Phys. Lett. B **242**, 245 (1990).
[32] H. Weigel, L. Gamberg, and H. Reinhardt, Phys. Rev. D **55**, 6910 (1997); H. Weigel and L. P. Gamberg, Nucl. Phys. **A680**, 48 (2000).
[33] X. Song, Phys. Rev. D **54**, 1955 (1996).
[34] M. Göckeler, R. Horsley, D. Pleiter, P. E. L. Rakow, A. Schäfer, G. Schierholz, H. Stüben, and J. M. Zanotti, Phys. Rev. D **72**, 054507 (2005).
[35] S. Riordan *et al.*, Phys. Rev. Lett. **105**, 262302 (2010).
[36] J. Kelly, Phys. Rev. C **70**, 068202 (2004).
[37] X. Song and J. S. McCarthy, Phys. Rev. D **49**, 3169 (1994); **50**, 4718(E) (1994).
[38] M. Stratmann, Z. Phys. C **60**, 763 (1993).
[39] X.-D. Ji and P. Unrau, Phys. Lett. B **333**, 228 (1994).
[40] X.-D. Ji and W. Melnitchouk, Phys. Rev. D **56**, R1 (1997).
[41] Jefferson Lab E07-003, https://userweb.jlab.org/~rondon/sane/.
[42] We use the parametrization for this ratio in our analysis from Ref. [194].
[43] P. Anthony *et al.* (E142 Collaboration), Phys. Rev. D **54**, 6620 (1996).
[44] K. Abe *et al.* (E154 Collaboration), Phys. Lett. B **404**, 377 (1997).
[45] K. Ackerstaff *et al.* (HERMES Collaboration), Phys. Lett. B **404**, 383 (1997).
[46] X. Zheng *et al.* (Jefferson Lab Hall A Collaboration), Phys. Rev. Lett. **92**, 012004 (2004).
[47] K. Abe *et al.* (E143 Collaboration), Phys. Rev. D **58**, 112003 (1998).
[48] N. Isgur, Phys. Rev. D **59**, 034013 (1999).
[49] E. Leader, A. V. Sidorov, and D. B. Stamenov, Int. J. Mod. Phys. A **13**, 5573 (1998).
[50] H. Avakian, S. J. Brodsky, A. Deur, and F. Yuan, Phys. Rev. Lett. **99**, 082001 (2007).
[51] C. Bourrely and J. Soffer, Nucl. Phys. **A941**, 307 (2015).
[52] I. C. Cloët, W. Bentz, and A. W. Thomas, Phys. Lett. B **621**, 246 (2005).
[53] C. D. Roberts, R. J. Holt, and S. M. Schmidt, Phys. Lett. B **727**, 249 (2013).
[54] A. Airapetian *et al.* (HERMES Collaboration), Phys. Rev. D **71**, 012003 (2005).
[55] M. Alekseev *et al.* (COMPASS Collaboration), Phys. Lett. B **693**, 227 (2010).
[56] K. Dharmawardane *et al.* (CLAS Collaboration), Phys. Lett. B **641**, 11 (2006).
[57] H. L. Lai, J. Huston, S. Kuhlmann, J. Morfin, F. Olness, J. F. Owens, J. Pumplin, and W. K. Tung(CTEQ Collaboration), Eur. Phys. J. C **12**, 375 (2000).
[58] A. Martin, W. Stirling, and R. Thorne, Phys. Lett. B **636**, 259 (2006).
[59] E. Leader, A. V. Sidorov, and D. B. Stamenov, Phys. Rev. D **75**, 074027 (2007).
[60] J. L. Friar, B. Gibson, G. Payne, A. Bernstein, and T. Chupp, Phys. Rev. C **42**, 2310 (1990).
[61] C. W. Leemann, D. R. Douglas, and G. A. Krafft, Annu. Rev. Nucl. Part. Sci. **51**, 413 (2001).
[62] M. Posik, Ph.D. thesis, Temple University, 2013.
[63] K. Aniol *et al.* (HAPPEX Collaboration), Phys. Rev. C **69**, 065501 (2004).
[64] D. Parno, Ph.D. thesis, Carnegie Mellon University, 2011.
[65] J. Alcorn *et al.*, Nucl. Instrum. Methods Phys. Res., Sect. A **522**, 294 (2004).
[66] K. Allada, Ph.D. thesis, University of Kentucky, 2010.
[67] A. A. Kresnin and L. N. Rozentsveig, Sov. Phys. JETP **5**, 288 (1957).
[68] A. V. Glamazdin *et al.*, Fiz. **B8**, 91 (1999).
[69] F. W. Lipps and H. A. Tolhoek, Physica (Amsterdam) **20**, 85 (1954).
[70] F. W. Lipps and H. A. Tolhoek, Physica (Amsterdam) **20**, 395 (1954).
[71] J. P. Jorda *et al.*, Nucl. Instrum. Meth. **A412**, 1 (1998).
[72] M. Friend *et al.*, Nucl. Instrum. Methods Phys. Res., Sect. A **676**, 96 (2012).
[73] D. S. Parno, M. Friend, V. Mamyan, F. Benmokhtar, A. Camsonne, G. B. Franklin, K. Paschke, and B. Quinn, Nucl. Instrum. Methods Phys. Res., Sect. A **728**, 92 (2013).
[74] M. G. Tiefenback and D. Douglas, Jefferson Lab Technical Report No. JLab-TN92-061, 1992.
[75] D. Marchand, Ph.D. thesis, Université Blaise Pascal, 1998.
[76] X. Qian *et al.* (Jefferson Lab Hall A Collaboration), Phys. Rev. Lett. **107**, 072003 (2011).
[77] C. Grupen and B. Shwartz, *Particle Detectors*, 2nd ed. (Cambridge University Press, Cambridge, UK, 2008).
[78] H. Bach and N. Neuroth, *The Properties of Optical Glass*, 2nd ed. (Springer, New York, 1995).
[79] D. Green, *The Physics of Particle Detectors* (Cambridge University Press, Cambridge, UK, 2000).
[80] X. Qian, Ph.D. thesis, Duke University, 2010.
[81] D. J. J. de Lange, J. J. M. Steijger, H. de Vries, M. Anghinolfi, M. Taiuti, D. W. Higinbotham, B. E. Norum, and E. Konstantinov, Nucl. Instrum. Methods Phys. Res., Sect. A **406**, 182 (1998).
[82] M. Posik *et al.* (to be published).
[83] R. Winston, J. Opt. Soc. Am. **60**, 245 (1970).
[84] The lead-glass blocks used had a Molière radius that contained $\gtrsim$90% of the total deposited energy of an incident particle; therefore, the blocks were grouped into a clustering scheme to capture more of the deposited energy [62]. See Sec. II F.
[85] W. A. Watson, J. Chen, G. Heyes, E. Jastrzembski, and D. Quarrie, IEEE Trans. Nucl. Sci. **41**, 61 (1994).
[86] D. Flay, Ph.D. thesis, Temple University, 2014.
[87] ROOT/C++ Analyzer for Hall A, http://hallaweb.jlab.org/podd/.

[88] ROOT: C++ Data Analysis Framework, http://root.cern.ch/drupal/.
[89] The details of the performance of the gas Čerenkov will be discussed in an upcoming publication [82].
[90] F. E. Wietfeldt, arXiv:1411.3687.
[91] F. D. Colegrove, L. D. Shearer, and G. K. Walters, Phys. Rev. **132**, 2561 (1963).
[92] W. Happer, Rev. Mod. Phys. **44**, 169 (1972); S. Appelt, A. Ben-Amar Baranga, C. J. Erickson, M. V. Romalis, A. R. Young, and W. Happer, Phys. Rev. A **58**, 1412 (1998).
[93] T. Chupp, M. Wagshul, K. Coulter, A. B. Mcdonald, and W. Happer, Phys. Rev. C **36**, 2244 (1987).
[94] T. G. Walker and W. Happer, Rev. Mod. Phys. **69**, 629 (1997); N. R. Newbury, A. S. Barton, P. Bogorad, G. D. Cates, M. Gatzke, H. Mabuchi, and B. Saam, Phys. Rev. A **48**, 558 (1993).
[95] T. G. Walker, J. H. Thywissen, and W. Happer, Phys. Rev. A **56**, 2090 (1997).
[96] C. Dutta, Ph.D. thesis, University of Kentucky, 2010.
[97] This cell does not have a pumping chamber.
[98] X. Zheng, Ph.D. thesis, Massachusetts Institute of Technology, 2002.
[99] A. Kolarkar, Ph.D. thesis, University of Kentucky, 2008.
[100] A. Kelleher, Ph. D. thesis, College of William and Mary, 2010.
[101] J. Huang, Ph.D. thesis, Massachusetts Institute of Technology, 2012.
[102] M. V. Romalis, Ph.D. thesis, Princeton University, 1997.
[103] J. Singh, A. M. Kelleher, and P. H. Solvignon, University of Virginia, Polarization Gradients in a Two Chambered Cell, Technical Report.
[104] Q. Ye, G. Laskaris, W. Chen, H. Gao, W. Zheng, X. Zong, T. Averett, G. D. Cates, and W. A. Tobias, Eur. Phys. J. A **44**, 55 (2010).
[105] P. A. M. Dolph, J. Singh, T. Averett, A. Kelleher, K. E. Mooney, V. Nelyubin, W. A. Tobias, B. Wojtsekhowski, and G. D. Cates, Phys. Rev. C **84**, 065201 (2011).
[106] S. Kadlecek, E. Babcock, I. A. Nelson, and T. G. Walker, Phys. Rev. A **71**, 013414 (2005).
[107] A. Abragam, *Principles of Nuclear Magnetism* (Oxford University Press, New York, 1961).
[108] W. Lorenzon, T. R. Gentile, and R. D. McKeown, Phys. Rev. A **47**, 468 (1993).
[109] A prescale factor restricts the number of events accepted for a given trigger. For example, a prescale of 100 means that one event per every 100 will be accepted. It was used either to remove certain types of events entirely or to restrict events due to high rates.
[110] 1 amagat $= 2.6867805 \times 10^{25}$ m^{-3}.
[111] The live-time is defined as the ratio of the number of triggers accepted by the DAQ to the total number of triggers generated for a given run [86]. This factor corrects for the high trigger rates during the experiment, which prevent the detectors from recording every event.
[112] Monte-Carlo Used in Hall A: SAMC, hallaweb.jlab.org/data_reduc/mc/mc.htm.
[113] J. J. LeRose, SNAKE transfer functions, http://hallaweb.jlab.org/news/minutes/tranferfuncs.html.
[114] L. W. Mo and Y.-S. Tsai, Rev. Mod. Phys. **41**, 205 (1969).
[115] A. Amroun *et al.*, Nucl. Phys. **A579**, 596 (1994).
[116] J. W. Lightbody and J. S. O'Connell, Comput. Phys. **2**, 57 (1988).
[117] S. Stein, W. B. Atwood, E. D. Bloom, R. L. A. Cottrell, H. DeStaebler, C. L. Jordan, H. G. Piel, C. Y. Prescott, R. Siemann, and R. E. Taylor, Phys. Rev. D **12**, 1884 (1975).
[118] D. Day, J. S. McCarthy, I. Sick, R. G. Arnold, B. T. Chertok, S. Rock, Z. M. Szalata, F. Martin, B. A. Mecking, and G. Tamas, Phys. Rev. Lett. **43**, 1143 (1979).
[119] C. Marchand *et al.*, Phys. Lett. **153B**, 29 (1985).
[120] Z.-E. Meziani *et al.*, Phys. Rev. Lett. **69**, 41 (1992).
[121] Y. S. Tsai, Report No. SLAC-PUB-0848, 1971.
[122] P. E. Bosted and V. Mamyan, arXiv:1203.2262.
[123] M. Anselmino, A. Efremov, and E. Leader, Phys. Rep. **261**, 1 (1995).
[124] P. Bosted, University of Massachusetts Technical Report No. CLASNOTE 2004-005, 2004.
[125] R. Michaels and B. Moffit, Parity DAQ for Charge Asymmetry Feedback, http://hallaweb.jlab.org/experiment/HAPPEX/HAPPEXII/paritydaq/parity_daq.html.
[126] S. Riordan, Ph.D. thesis, Carnegie Mellon University, 2008.
[127] G. W. Miller, Ph.D. thesis, Princeton University, 2001.
[128] D. de Florian, R. Sassot, M. Stratmann, and W. Vogelsang, Phys. Rev. Lett. **101**, 072001 (2008).
[129] P. E. Bosted, Phys. Rev. C **51**, 409 (1995).
[130] J. E. Amaro, M. B. Barbaro, J. A. Caballero, T. W. Donnelly, A. Molinari, and I. Sick, Phys. Rev. C **71**, 015501 (2005).
[131] M. Amarian *et al.*, Phys. Rev. Lett. **89**, 242301 (2002); K. Slifer *et al.* (E94010 Collaboration), Phys. Rev. Lett. **101**, 022303 (2008).
[132] I. Akushevich, A. Ilyichev, N. Shumeiko, A. Soroko, and A. Tolkachev, Comput. Phys. Commun. **104**, 201 (1997).
[133] F. R. P. Bissey, V. A. Guzey, M. Strikman, and A. W. Thomas, Phys. Rev. C **65**, 064317 (2002).
[134] C. Bourrely, J. Soffer, and F. Buccella, Eur. Phys. J. C **23**, 487 (2002); Phys. Lett. B **648**, 39 (2007).
[135] D. de Florian, G. Navarro, and R. Sassot, Phys. Rev. D **71**, 094018 (2005).
[136] T. Gehrmann and W. J. Stirling, Phys. Rev. D **53**, 6100 (1996).
[137] A. Accardi, A. Bacchetta, W. Melnitchouk, and M. Schlegel, J. High Energy Phys. 11 (2009) 093.
[138] A. Accardi, A. Bacchetta, and M. Schlegel, AIP Conf. Proc. **1155**, 35 (2009).
[139] P. Anthony *et al.* (E155 Collaboration), Phys. Lett. B **458**, 529 (1999).
[140] K. Ackerstaff *et al.* (HERMES Collaboration), Phys. Lett. B **475**, 386 (2000); **567**, 339 (2003).
[141] J. J. Aubert *et al.*, Phys. Lett. B **123**, 275 (1983).
[142] J. Arrington, J. Phys. Conf. Ser. **69**, 012024 (2007).
[143] J. Owens, A. Accardi, and W. Melnitchouk, Phys. Rev. D **87**, 094012 (2013).
[144] Y. Prok *et al.* (CLAS Collaboration), Phys. Rev. C **90**, 025212 (2014).
[145] A. Airapetian *et al.* (HERMES Collaboration), Phys. Rev. D **75**, 012007 (2007).
[146] J. Ashman *et al.* (European Muon Collaboration), Phys. Lett. B **206**, 364 (1988).
[147] J. Ashman *et al.* (European Muon Collaboration), Nucl. Phys. **B328**, 1 (1989).

[148] M. Alekseev *et al.* (COMPASS Collaboration), Phys. Lett. B **690**, 466 (2010).
[149] B. Adeva *et al.* (Spin Muon Collaboration), Phys. Rev. D **58**, 112001 (1998).
[150] J. J. Ethier and W. Melnitchouk, Phys. Rev. C **88**, 054001 (2013).
[151] K. Ackerstaff *et al.* (HERMES Collaboration), Phys. Lett. B **464**, 123 (1999).
[152] P. Solvignon *et al.* (Jefferson Lab E01-012 Collaboration), Phys. Rev. Lett. **101**, 182502 (2008).
[153] K. Kramer, Ph.D. thesis, College of William and Mary, 2003.
[154] K. Kramer *et al.*, Phys. Rev. Lett. **95**, 142002 (2005).
[155] M. Posik *et al.* (Jefferson Lab Hall A Collaboration), Phys. Rev. Lett. **113**, 022002 (2014).
[156] W. Melnitchouk, R. Ent, and C. Keppel, Phys. Rep. **406**, 127 (2005).
[157] O. Nachtmann, Nucl. Phys. **B63**, 237 (1973); A. Accardi and W. Melnitchouk, Phys. Lett. B **670**, 114 (2008); A. V. Sidorov and D. B. Stamenov, Mod. Phys. Lett. A **21**, 1991 (2006); S. Matsuda and T. Uematsu, Nucl. Phys. **B168**, 181 (1980); S. Wandzura, Nucl. Phys. **B122**, 412 (1977).
[158] V. M. Braun, T. Lautenschlager, A. N. Manashov, and B. Pirnay, Phys. Rev. D **83**, 094023 (2011).
[159] V. M. Braun, G. P. Korchemsky, and A. N. Manashov, Nucl. Phys. **B603**, 69 (2001).
[160] M. Botje, Comput. Phys. Commun. **182**, 490 (2011).
[161] K. A. Olive *et al.* (Particle Data Group Collaboration), Chin. Phys. C **38**, 090001 (2014).
[162] N. Sato, W. Melnitchouk, S. E. Kuhn, J. J. Ethier, and A. Accardi, Phys. Rev. D **93**, 074005 (2016).
[163] A. Airapetian *et al.* (HERMES Collaboration), Eur. Phys. J. C **26**, 527 (2003).
[164] K. Abe *et al.* (E154 Collaboration), Phys. Rev. Lett. **79**, 26 (1997).
[165] R. L. Heimann, Nucl. Phys. **B64**, 429 (1973).
[166] J. R. Ellis and M. Karliner, Phys. Lett. B **213**, 73 (1988).
[167] S. Galster, H. Klein, J. Moritz, K. H. Schmidt, D. Wegener, and J. Bleckwenn, Nucl. Phys. **B32**, 221 (1971).
[168] S. Bethke, Eur. Phys. J. C **64**, 689 (2009).
[169] A. Accardi *et al.*, arXiv:1212.1701.
[170] E. R. Nocera, R. D. Ball, S. Forte, G. Ridolfi, and J. Rojo (NNPDF Collaboration), Nucl. Phys. **B887**, 276 (2014).
[171] N.-Y. Lee, K. Goeke, and C. Weiss, Phys. Rev. D **65**, 054008 (2002).
[172] J. Balla, M. V. Polyakov, and C. Weiss, Nucl. Phys. **B510**, 327 (1998).
[173] E. Stein, P. Gornicki, L. Mankiewicz, and A. Schafer, Phys. Lett. B **353**, 107 (1995).
[174] D. S. Parno *et al.* (Jefferson Lab Hall A Collaboration), Phys. Lett. B **744**, 309 (2015).
[175] P. Anthony *et al.* (E155 Collaboration), Phys. Lett. B **493**, 19 (2000).
[176] R. P. Feynman, Phys. Rev. Lett. **23**, 1415 (1969).
[177] G. Petratos *et al.*, Measurement of the f_2^n/f_2^p Ratios and $a = 3$ EMC Effect in Deep Inelastic Scattering off the Tritium and Helium Mirror Nuclei, proposal for Jefferson Lab PAC 37, 2010.
[178] A. Camsonne *et al.*, Probing Quark-Gluon Correlations in the Neutron: A Precision Measurement of the Neutron g_2 and d_2 at High q^2 in Hall A, proposal for Jefferson Lab PAC 30, 2006.
[179] T. Averett *et al.*, Measurement of Neutron Spin Asymmetry a_1^n in the Valence Quark Region Using 8.8 GeV and 6.6 GeV Beam Energies and BigBite Spectrometer in Hall A, proposal for Jefferson Lab PAC 30, 2006.
[180] G. Cates *et al.*, Measurement of Neutron Spin Asymmetry a_1^n in the Valence Quark Region Using an 11 GeV Beam and a Polarized ^{3}He Target in Hall C, proposal for Jefferson Lab PAC 36, 2010.
[181] See Supplemental Material at http://link.aps.org/supplemental/10.1103/PhysRevD.94.052003 for raw data files containing tables of all results (and their uncertainties) reported.
[182] F. Halzen and A. D. Martin, *Quarks and Leptons* (John Wiley and Sons, Inc., New York, 1984).
[183] J. Bjorken and E. A. Paschos, Phys. Rev. **185**, 1975 (1969).
[184] J. Callan, G. Curtis, and D. J. Gross, Phys. Rev. Lett. **22**, 156 (1969).
[185] D. Drechsel, S. Kamalov, and L. Tiator, Phys. Rev. D **63**, 114010 (2001).
[186] The convention used by [156] is such that the matrix elements are labeled according to n as opposed to $n-1$, as defined in this paper.
[187] K. Slifer, Ph.D. thesis, Temple University, 2004.
[188] Y. Dong, Phys. Rev. C **77**, 015201 (2008).
[189] H. Georgi and H. D. Politzer, Phys. Rev. D **14**, 1829 (1976).
[190] A. Piccione and G. Ridolfi, Nucl. Phys. **B513**, 301 (1998).
[191] F. James and M. Roos, Comput. Phys. Commun. **10**, 343 (1975).
[192] J. Pumplin, D. R. Stump, J. Huston, H.-L. Lai, P. Nadolsky, and W.-K. Tung, J. High Energy Phys. 07 (2002) 012.
[193] M. Arneodo *et al.* (New Muon Collaboration), Phys. Lett. B **364**, 107 (1995).
[194] K. Abe *et al.* (E143 Collaboration), Phys. Lett. B **452**, 194 (1999).